Controlling surface plasmon polaritons with dielectric nanostructures

Dissertation

zur

Erlangung des Doktorgrades (Dr. rer. nat.)

der

Mathematisch-Naturwissenschaftlichen Fakultät

der

Rheinischen Friedrich-Wilhelms-Universität Bonn

vorgelegt von

Felix Bleckmann

aus

Bonn

Bonn, 2016

Dieser Forschungsbericht wurde als Dissertation von der
Mathematisch-Naturwissenschaftlichen Fakultät der Universität Bonn angenommen und ist auf
dem Hochschulschriftenserver der ULB Bonn
`http://hss.ulb.uni-bonn.de/diss_online` elektronisch publiziert.

1. Gutachter: Prof. Dr. Stefan Linden
2. Gutachterin: Priv.-Doz. Dr. Elisabeth Soergel

Tag der Promotion: 17.06.2016
Erscheinungsjahr: 2016

Abstract

This thesis focuses on the investigation of methods to control surface plasmon polaritons (SPPs), i.e., coupled oscillations of electromagnetic waves with the conduction band electrons at the surface of metals.

In the first part, the evolution of so-called Airy SPP beams propagating under influence of a non-vanishing gradient of the effective refractive index is investigated. These beams represent the plasmonic analog to a class of non-diffracting wave packets, named Airy beams. We experimentally demonstrate that by fabricating dielectric wedges on top of a gold layer with negative-tone gray-scale electron beam lithography, Airy SPP beams can be bent in a controlled manner. The evolution of bent Airy SPP beams is observed by making use of leakage radiation microscopy. The results exhibit an excellent agreement to our numerical calculations.

In the second part of this thesis we use dielectric loaded SPP waveguide arrays as quantum simulators. In this context, a Su-Schrieffer-Heeger topological insulator is implemented in the plasmonic system. Such material can provide both, a band structure with a band gap in its bulk material as well as in-gap states, localized at the surface/edge of the system. The waveguide arrays are fabricated on top of a gold layer by negative-tone gray-scale electron beam lithography. The intensity distribution of propagating SPPs in these arrays is then investigated in both, real and Fourier space by making use of leakage radiation microscopy. As a result, a topologically protected edge state is observed as localized state in the real space and as an in-gap state in the Fourier space. All results are in excellent agreement to numerical calculations.

The last part of the thesis is dedicated to the switching of plasmonic systems. For this purpose we make use of photochromic materials, i.e., materials that provide isomers with different complex refractive indices which can be converted into each other by light induced chemical reactions. In this context, we investigate Fano resonances in photochromic metallic photonic crystal slabs on their behavior by switching the state of a photochromic layer. The Fano resonances are induced by the interaction of localized plasmonic modes in gold wires with extended waveguide modes in the dielectric layer. The corresponding structures are fabricated with positive tone electron beam lithography. By careful adjustment of all parameters we observe a strong blurring of the Fano resonance upon switching the photochromic material. All results are in good agreement to numerical calculations.

Finally, we investigate the influence of a changing real part of the effective refractive index on SPPs propagating along a photochromic-material-gold interface, as induced by photochromic switching. By making use of Fourier space imaging we demonstrate a change of the effective refractive index of the SPPs of approximately 5%. Additionally, first experiments on the manipulation of propagating SPPs by a locally switched photochromic layer are discussed.

Contents

Introduction

Humans are fascinated by light. Already in the 3rd century before Christ, Archimedes dedicated parts of his work to optics. In the following centuries, the endeavor of many scientists built the basis of a strong evolution of this research area. As a result, devices with functions based on optics play an important role in our daily life, e.g., lenses, telescopes, and microscopes are used to improve the visual capacity and allow for a deep insight both, in microcosm and space. In addition to these directly related applications, the evolution of optics led also to the development of new sub-disciplines, which became distinct fields of research with own applications.

One of these fields is named plasmonics. It originates from the work of Ritchie [1] in the mid of the last century and focuses on the investigation of surface plasmon polaritons (SPPs), i.e., coupled oscillations of electromagnetic waves with the conduction band electrons at the interfaces of metals. In the subsequent years it has evolved fast. Based on experiments, performed by Otto [2], as well as Kretschmann and Reaether [3] on the excitation of SPPs, the field now incorporates many branches of research, spreading from biosensing [4] to photovoltaic devices [5].

One of the intensively developing research topics in the field is the study of propagating SPPs, excited at a metal dielectric interface [6]. Their propagating nature in combination with a strong confinement to the metal's surface and a reduced wavelength promises further applications, e.g., in the plasmonic circuitry [7, 8]. Since the ability to precisely control the propagation of SPPs is the first step towards such applications, this topic is currently in the focus of many research groups. It turned out that a number of concepts developed in the frames of conventional optics can be utilized for the manipulation of SPPs. So it is feasible to create simple optical elements, e.g., lenses [9, 10] and waveguides [11–13], as well as the more complicated gradient index (GRIN) elements [14, 15] for propagating SPPs.

Based on such optical elements, the transfer of further concepts from conventional optics to plasmonics can give a deeper insight into new and interesting physics, even exceeding the frames of conventional optics. I would like to emphasize this with the following examples.

One concept that can be transferred to plasmonics is the generation of non-diffracting beams. This designates a class of beams, which preserve their shape during the propagation and thus become less affected by diffraction effects. A prominent member are the so-called Airy beams, which were suggested in the pioneering work of Berry et al. [16]. Besides their non-diffracting

nature they also exhibit a number of other remarkable features, such as a self-accelerating behavior and self-healing after passing through obstacles [17].

Their plasmonic analog are the so-called Airy SPP beams [18] that offer the same intriguing properties as their free space counterpart [19, 20]. Their high confinement to the interface and efficient energy transfer, however, make them additionally attractive for the application in plasmonic circuitry [19–21] and hot-spot creation [22]. Even more and more flexible applications could be achieved if a manipulation by preserving their unique properties is possible. As it tuned out, this can be achieved by making use of GRIN elements [23].

In this thesis we will therefore implement GRIN elements in a plasmonic system in order to manipulate Airy SPP beams by preserving their unique properties.

A second example is the coupled mode theory. In the context of conventional optics, it is used to approximate the field evolution in arrays of evanescently coupled single mode waveguides [24, 25]. This description exhibits a remarkable mathematical similarity to the temporal evolution of an electron in a crystal lattice, according to the condensed matter tight binding model [26]. An electromagnetic wave in a waveguide array can therefore be used to simulate the temporal evolution of electrons in a crystal lattice. Since a temporal effect is mapped onto a spatial evolution, this approach allows for the simpler tailoring of the system's properties. As a result, a number of interesting effects has already been demonstrated in this context [27–30].

Transferring this idea to plasmonic systems provides additional advantages. Beside the possibility to image the field evolution inside the waveguides [31–33], the imaging of its Fourier transform becomes possible [34]. This is of high interest, since it allows also for the investigation of the band structure of the waveguide array. In this context, a plasmonic realization of the Su-Schrieffer-Heeger model is of particular interest. It originally describes the behavior of solitons in polyacetylene [35, 36] and furthermore the behavior of a 1D topological insulator. A system described by this model provides a complex band structure. On the one hand, its bulk material offers an empty band gap, while on the other hand, there can be states located in the gap. These so-called topologically protected edge states can exist at the surface or edge of the system [37, 38]. In this context, recent investigations on plasmonic waveguide arrays concentrated only on the field distribution at the end facets of the waveguides [39]. Thus, it is of high interest to extend the present investigations to the field distributions inside the waveguides and the corresponding band structure.

One part of this thesis is therefore dedicated to the investigation of propagating SPPs in waveguide arrays, mimicking a Su-Schrieffer-Heeger topological insulator, by making use of both, real and Fourier space imaging.

A third concept well known in conventional optics is the switching of optical properties, as it is used for example in liquid crystal retarders or beam shutters. Also this concept can be transferred to plasmonic systems, leading to interesting new features exceeding the possibilities of conventional optics. In order to implement this, a growing field of research concentrates on plasmonic systems that can be switched between different states [40–42]. One particularly interesting approach in this context makes use of photochromic molecules, i.e., molecules that can, under illumination with light, be reversibly converted between two different isomers with different complex refractive indices. Such molecules can offer a large change in the optical properties, thus are promising candidates for switching applications.

In the context of propagating SPPs, present investigations mainly concentrated on the photochromic manipulation by increasing the absorption in the system [43]. Based on the working principle of conventional lenses it would, however, be interesting to manipulate propagating SPPs via a changing real part of the refractive index in such material. Being able to alter it, even locally, would facilitate the generation of refracting boundaries of tailored shape with switchable properties.

In order to fill this gap, a part of this thesis will focus the manipulation of propagating SPPs with photochromic materials that exhibit a large change in the real part of the refractive index.

In addition to the systems discussed above, which were based on the concepts transferred from conventional optics to plasmonics, there are also plasmonic systems that can be directly used for free space applications, e.g., as filter. Basis are the so-called localized SPPs, which can directly interact with the light field [6]. Also in this field of research the attractive properties of photochromic materials have been used already [44–47], however, with a rather low influence on the systems.

An improvement can be achieved by investigating hybrid systems, simultaneously obtaining two effects. For example, if a broad plasmonic resonance overlaps with a sharp resonance of another type. This can lead to a hybridization of both resonances, as described by a Fano resonance [48]. In terms of plasmonics, such Fano resonances have already been observed in many different nano-structures, as for example in oligomers [49–51]. These resonances obtain highly dispersive properties, making them attractive for switching applications [52]. A particular promising system in this context are metallic photonic crystal slabs, in which the Fano resonance stems from the interaction of localized plasmonic and extended waveguide modes [53, 54]. This special combination makes the Fano resonance highly dependent on the waveguide's damping and hence let us anticipate an effective switching procedure.

For this reason, one part of this thesis will investigate the influence of a changing absorption on the properties of photochromic metallic photonic crystal slabs.

Outline

Chapter 2 gives a brief introduction into all basic concepts utilized in this thesis. For this purpose, starting from the Maxwell equations and the Drude Lorentz model, propagating and localized surface plasmon polaritons (SPPs) are introduced.

Based on a short discussion of freely propagating Airy SPP beams (a class of non-diffracting SPP beams), **Chapter 3** introduces dielectric ramps on top of the gold layer as manipulation method for Airy SPP beams. The utilized samples are fabricated by making use of gray-scale electron beam lithography (gEBL) and are experimentally investigated with leakage radiation microscopy (LRM). This leads to the experimental demonstration of bent Airy SPP beams.

Chapter 4 starts with the introduction of the coupled mode theory (CMT) for plasmonic waveguide arrays. Additionally, a more rigorous calculation method is developed. With both methods as a basis, plasmonic waveguide arrays are introduced as simulator of the Su-Schrieffer-Heeger (SSH) model. Subsequently, appropriate samples are fabricated by making use of gEBL and investigated with the help of LRM. As a result, the plasmonic SSH model is experimentally demonstrated.

Chapter 5 is dedicated to the photochromic switching of plasmonic systems. In a first part, the photochromic switching of Fano resonances in photochromic metallic photonic crystals is theoretically discussed on basis of a simple oscillator model and more rigorous scattering matrix based calculations. The samples are fabricated by making use of positive tone electron beam lithography (pEBL) with a subsequent spin-coating of the photochromic layer. With this as a basis, the switching of Fano resonances is experimentally demonstrated.

The second part of this chapter focuses on the photochromic switching of propagating SPPs. Based on theoretical calculations, both, the influence of a local as well as a global switching of the photochromic material on propagating SPPs is discussed. The samples are fabricated by making use of pEBL and subsequently investigated in an optical setup utilizing LRM. This results in the experimental demonstration of manipulated propagating SPPs.

Theoretical basics

This thesis presents a number of possibilities to control surface plasmon polaritons (SPPs), i.e., coupled oscillations of electromagnetic waves with the metal's conduction band electrons at metal dielectric interfaces. The aim of this chapter is to introduce the theoretical basics, needed to understand the plasmonic systems discussed in this thesis. For this purpose, it starts with the description of the basic principles of electromagnetic waves in matter and the optical properties of gold, the metal utilized in the presented experiments. With this as basis, interfaces of infinite extensions between gold and dielectric half-spaces are discussed. They are one of the simplest types of systems where propagating SPPs can exist. Finally, the last part of this chapter concentrates on one type of interface with finite dimensions: a single gold wire. In this particular case, the strong influence of the structure's boundaries facilitates the excitation of another type of SPPs, the so-called localized SPPs.

2.1 Electromagnetic waves

The natural starting point for the investigation of electromagnetic waves interacting with matter are the macroscopic Maxwell equations. They can be written as [55]:

$$\nabla \cdot \boldsymbol{D} = \rho, \qquad\qquad \nabla \cdot \boldsymbol{B} = 0, \qquad\qquad (2.1)$$

$$\nabla \times \boldsymbol{E} = -\frac{\partial \boldsymbol{B}}{\partial t}, \qquad\qquad \nabla \times \boldsymbol{H} = \boldsymbol{j} + \frac{\partial \boldsymbol{D}}{\partial t}, \qquad\qquad (2.2)$$

with the magnetic field $\boldsymbol{H}$, the electric field $\boldsymbol{E}$, the charge density ρ, and the current density $\boldsymbol{j}$. In case of homogeneous and linear media having a permeability of $\mu_\mathrm{r} = 1$, as they are used in this thesis, the dielectric displacement $\boldsymbol{D}$ and the magnetic induction $\boldsymbol{B}$ depend linearly on $\boldsymbol{H}$ and $\boldsymbol{E}$. In a material with the permittivity ε_r, this dependency is given by [55]:

$$\boldsymbol{D} = \varepsilon_0 \varepsilon_\mathrm{r} \boldsymbol{E}, \qquad\qquad \boldsymbol{B} = \mu_0 \boldsymbol{H}. \qquad\qquad (2.3)$$

For the systems discussed in this thesis, the system of equations can be simplified. Here, it is sufficient to consider an electromagnetic wave with the free space wavelength λ_0, frequency ω, and a harmonic time dependence ($\boldsymbol{E}(\boldsymbol{r},t) = \boldsymbol{E}(\boldsymbol{r})e^{-\mathrm{i}\omega t}$), propagating in absence of external

charges and current. In this special case a combination of the two curl equations (2.2), by making use of the vector identity:

$$\nabla \times (\nabla \times E) = \nabla (\nabla \cdot E) - \nabla^2 E, \tag{2.4}$$

leads to the so-called Helmholtz equation [56]:

$$\left(\nabla^2 + n^2 k_0^2\right) \cdot E = 0. \tag{2.5}$$

This equation describes the evolution of an electromagnetic wave, with the wave number in vacuum given by $k_0 = \frac{2\pi}{\lambda_0}$, in a medium characterized by the refractive index $n = \sqrt{\varepsilon_r}$. A corresponding wave equation for the magnetic field, the magnetic Helmholtz equation can be calculated analogously [56].

A simple solution of the electrical Helmholtz equation and the basis of the discussions in the subsequent sections, is a plane wave propagating in an isotropic medium. Without loss of generality it is traveling along the z-direction with a wave vector k parallel to the z-axis and a propagation constant described by $|k| = k_z$. Such plane wave is described by:

$$E(r) = E_0(\mathrm{x}, \mathrm{y})e^{ikr} = E_0(\mathrm{x}, \mathrm{y})e^{ik_z z}. \tag{2.6}$$

Its, typically complex, amplitude $E_0(\mathrm{x}, \mathrm{y})$ defines the polarization of the wave. With this, the Helmholtz equation for the present system further reduces to:

$$\left(\frac{\partial^2}{\partial x^2} + \frac{\partial^2}{\partial y^2} + n^2 k_0^2\right) E_0(\mathrm{x}, \mathrm{y}) = k_z^2 E_0(\mathrm{x}, \mathrm{y}). \tag{2.7}$$

2.2 Drude Lorentz model

All metal structures utilized in this thesis consist out of gold. This material has the advantage, that it is not only chemically stable but at the same time provides low ohmic losses in the infrared and a large part of the visible spectral range [57].

In order to understand the behavior of the structures utilized in the remaining parts of this thesis, the optical properties of gold have to be discussed. As it turns out they can be described piecewise by models based on publications of Paul Drude [58] and Hendrik A. Lorentz [59]. A good approximation for the properties of gold in the infrared regime is the Drude model, which models the interaction of electromagnetic waves with the metal by an externally driven oscillation of the free electron gas, relatively to the positive background of the nuclei [56]. The dielectric behavior of gold in the vicinity of the intra-band transitions taking place in the visible part of the spectrum can however be described by the Lorentz model [56]. It describes the interaction of the electromagnetic wave with gold as an externally driven and damped oscillation of the single electrons relatively to their atomic nuclei, possessing a resonance frequency.

In order to cover a large spectral range, in this thesis, a fit of a combined model to the experimental data given by Johnson et al. [57] is used. With this we obtain the following equation for the

permittivity of gold [60]:

$$\varepsilon(\omega) = \varepsilon_\infty - \frac{\omega_D^2}{\omega(\omega + i\gamma_D)} - \frac{\Delta\varepsilon\omega_L^2}{\omega^2 - \omega_L^2 + i\gamma_L\omega}. \tag{2.8}$$

The first two addends result from the Drude model, while the third accounts for a single Lorentzian oscillator. The included parameters are the plasma frequency $\omega_D = 8.794\,\text{eV}$, the eigenfrequency of the Lorentz oscillator $\omega_L = 2.646\,\text{eV}$, the corresponding dampings $\gamma_D = 0.066\,\text{eV}$ and $\gamma_L = 0.382\,\text{eV}$ as well as the remaining two parameters $\varepsilon_\infty = 6.21$ and $\Delta\varepsilon = 1$.

2.3 Propagating surface plasmon polaritons

Based on the general discussion of electromagnetic waves interacting with matter and the optical properties of gold, we can now discuss the simplest environment in which SPPs can exist. It is formed by a metal dielectric interface with infinite dimensions [6], e.g., between a dielectric and a gold half-space, as it is sketched in Fig. 2.1.

Figure 2.1: Two layer system with an interface along the zy-plane between a dielectric and a gold half-space.

In order to find the allowed solutions of the Maxwell equations for the given system, it is sufficient to consider only the so-called transverse electrical (TE) and transverse magnetic (TM) polarizations. This stems from the fact that they form a complete system of polarization states [56], with $\boldsymbol{H}$ and $\boldsymbol{E}$ given by:

$$
\begin{array}{cc}
\text{TE} & \text{TM} \\[4pt]
\begin{pmatrix} H_x \\ 0 \\ H_z \end{pmatrix}, \begin{pmatrix} 0 \\ E_y \\ 0 \end{pmatrix} &
\begin{pmatrix} 0 \\ H_y \\ 0 \end{pmatrix}, \begin{pmatrix} E_x \\ 0 \\ E_z \end{pmatrix}
\end{array}
$$

By regarding the continuity conditions at an interface between the dielectric and the gold half-space, shown in Fig. 2.1, it turns out that in this two layer system the Maxwell equations provide only TM polarized solutions, which correspond to propagating waves along the interface [56]. These waves are the so-called propagating SPPs (without loss of generality propagating in positive z-direction) [6]. Based on the Maxwell equations, in a metal with permittivity ε_g and a dielectric with permittivity ε_d, their non-zero field components ($H_y\ E_x,\ E_z$) are given by the

following set of equations [56]:

$$x > 0 \qquad\qquad\qquad x < 0$$

$$H_y(x, z) = A_d e^{i\beta z} e^{-k_d x}, \qquad\qquad H_y(x, z) = A_g e^{i\beta z} e^{k_g x}, \qquad (2.9)$$

$$E_x(x, z) = -A_d \frac{\beta}{\omega \varepsilon_0 \varepsilon_d} e^{i\beta z} e^{-k_d x}, \qquad E_x(x, z) = -A_g \frac{\beta}{\omega \varepsilon_0 \varepsilon_g} e^{i\beta z} e^{k_g x}, \qquad (2.10)$$

$$E_z(x, z) = i A_d \frac{1}{\omega \varepsilon_0 \varepsilon_d} k_d e^{i\beta z} e^{-k_d x}, \qquad E_z(x, z) = -i A_g \frac{1}{\omega \varepsilon_0 \varepsilon_g} k_g e^{i\beta z} e^{k_g x}, \qquad (2.11)$$

with the condition

$$k_i^2 = \beta^2 - k_0^2 \varepsilon_i, \qquad\qquad i \in \{d, g\}, \qquad (2.12)$$

and, resulting from the continuity at the interface:

$$\frac{k_g}{k_d} = -\frac{\varepsilon_g}{\varepsilon_d}. \qquad (2.13)$$

From these equations we can deduce the main characteristics of SPPs, propagating along the dielectric gold interface:

Penetration depth

The field of the propagating SPPs is, perpendicular to the propagation direction, exponentially decaying in both media away from the interface. A measure of this is the penetration depth that for each side of the interface is given by [56]:

$$s_j = \frac{1}{|k_j|}, \qquad\qquad j \in \{d, g\}. \qquad (2.14)$$

It describes the length after which the amplitude of the field dropped to $1/e$ of its initial value. In the case of a vacuum gold interface, a free space wavelength of $\lambda_0 = 980\,\text{nm}$, and a vacuum permittivity of $\varepsilon_d = 1$ the penetration depths for both sides of the interface are:

$$s_d \approx 984\,\text{nm}, \qquad\qquad s_g \approx 24\,\text{nm}. \qquad (2.15)$$

Due to this strong decay perpendicular to the interface, propagating SPPs can be seen as bound to the interface and hence as effective two-dimensional waves.

Dispersion relation

The field evolution in propagation (z-) direction included in (2.9)–(2.11) is mainly described by the propagation constant β. By using (2.12)–(2.13), it can be derived to [56]:

$$\beta = k_0 \sqrt{\frac{\varepsilon_d \varepsilon_g}{\varepsilon_d + \varepsilon_g}}. \qquad (2.16)$$

The resulting dispersion relation for SPPs, propagating at a vacuum gold interface, is plotted in Fig. 2.2 together with the light cone in vacuum and glass, given by $k_{vac}(\omega) = \omega/c_0$ and $k_{glass}(\omega) = n_{glass}\,\omega/c_0 = 1.5\,\omega/c_0$, respectively.
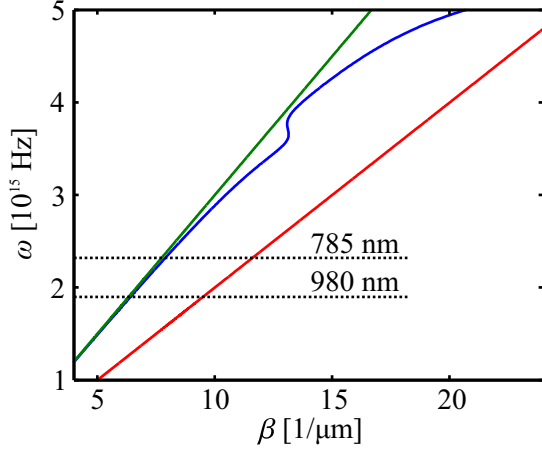

Figure 2.2: Dispersion relation of propagating SPPs at a vacuum gold interface (blue), based on $\varepsilon_d = 1$ and the material properties of gold given by (2.8). Additionally plotted are the light cone in vacuum (green), described by $k_{vac}(\omega)$, as well as the light cone in glass (red), described by $k_{glass}(\omega)$. The wavelengths, mostly used in this thesis, are marked as examples.

Since the SPP dispersion relation lies to the right side of the vacuum light line, the SPPs cannot couple to propagating modes in vacuum. This ensures the binding of the propagating SPPs to the interface and simultaneously makes it challenging to excite them with free space radiation in vacuum.

For the further discussions it is useful to introduce an effective refractive index as a measure for the change in the propagation constant, being defined by:

$$n_{eff} = \frac{\beta}{k_0} \xrightarrow[980\,nm]{vac-au} 1.0125 + 0.0008i. \qquad (2.17)$$

Here, n_{eff} is calculated for propagating SPPs at a vacuum gold interface with a free space wavelength of $\lambda_0 = 980\,nm$.

Wavelength

Similar to free space optics, from the real part of the effective refractive index, the shortened wavelength of propagating SPPs can be calculated as [56]:

$$\lambda_{SPP} = \frac{\lambda_0}{\Re(n_{eff})} \xrightarrow[980\,nm]{vac-au} \approx 968\,nm. \qquad (2.18)$$

Propagation length

From (2.9)–(2.11) results that the imaginary part of the effective refractive index describes the absorption in the system. It induces an exponential decay of the SPP's intensity in propagation direction, described by the so-called propagation length [56]:

$$L_{SPP} = \frac{1}{2k_0\Im(n_{eff})} \xrightarrow[980\,nm]{vac-au} \approx 95\,\mu m. \qquad (2.19)$$

Note, that the propagation length strongly depends on the used free space wavelength. The larger ohmic losses in gold, for example at 785 nm wavelength, lead to a drastically reduced propagation length of approximately 40 μm.

2.3.1 Surface plasmon polariton excitation

Since the SPP propagation constant is bigger than the wave vector in vacuum, due to conservation of momentum, the excitation of propagating SPPs at a perfectly flat interface is not possible. However, there are several possibilities to overcome this momentum mismatch in experimental environments as for example by making use of end-fire coupling [61], prism coupling in the so-called Kretschmann configuration [3] and the Otto configuration [2], or just the roughness of the surface [6]. In this thesis we utilize a more flexible approach: a grating coupler made of dielectric ridges. The working principle is sketched in Fig. 2.3 for an ideal grating coupler, consisting of dielectric ridges of infinite length on top of the gold layer.

Figure 2.3: An electromagnetic wave with the wave vector $\boldsymbol{k}_0$ polarized along the z-direction, illuminates a dielectric grating with period p and excites propagating SPPs with the wave vector $\boldsymbol{\beta}$.
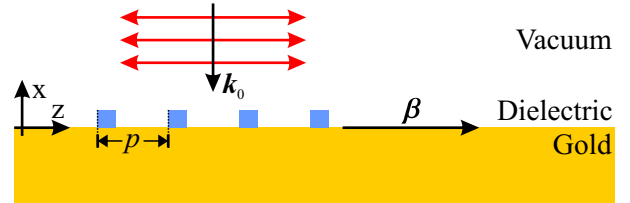
In order to excite propagating SPPs ($\boldsymbol{\beta}$) with such a dielectric grating of period p by a horizontally polarized electromagnetic wave with the wave vector $\boldsymbol{k}_0$, impinging from positive x-direction, Bragg's condition has to be fulfilled. With the unit vector in z-direction ($\hat{\mathbf{z}}$), this condition can be written as [56]:

$$\boldsymbol{\beta} = (k_{0,z} + m \cdot \frac{2\pi}{p}) \cdot \hat{\mathbf{z}}, \qquad m \, \epsilon \, \mathbb{N}. \tag{2.20}$$

In the simple case of $\boldsymbol{k}_0$ being perpendicular to the interface, the necessary period has therefore to be an integral multiple of the SPP wavelength.

The intensity distribution of the propagating SPPs in y-direction, resulting from the excitation at such grating coupler, is determined by the intensity distribution of the laser spot on the grating. As the laser beam is Gaussian shaped in most cases, the intensity of propagating SPPs is also of Gaussian shape.

2.3.2 Surface plasmon polariton detection

As it was introduced in the last sections, propagating SPPs are bound to the interface. This feature makes it challenging to image their intensity distribution on top of the gold film. Nevertheless, there have been many ideas to overcome this issue. On the one hand scanning near-field optical microscopes (SNOM) are used to make the evanescent field in vacuum visible [62, 63] taking an image, rather time consuming, by raster scanning a near-field probe over the interface. On the other hand fluorescent layers were added on top of the gold film [64] or inside the investigated structures [15], and the fluorescence, excited by the propagating SPPs, is collected and imaged.
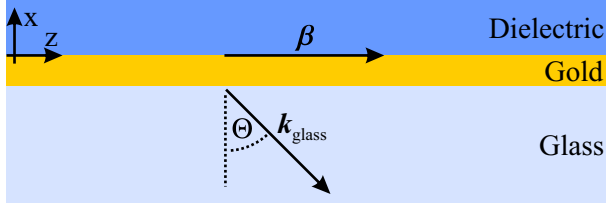
Figure 2.4: Detection principle of propagating SPPs with a wave vector $\boldsymbol{\beta}$ at a metal dielectric interface. In case of a thin gold layer, the SPPs can leak through the layer and couple to propagating modes in glass, obtaining the emission angle Θ and the wave vector $\boldsymbol{k}_{\text{glass}}$.

In this thesis we make use of another approach that allows not only to image the intensity distribution of propagating SPPs on top of a gold layer [65], but also to detect the absolute value of the propagation constant [66]. For this purpose, the thickness of the gold layer is chosen to be 60 nm and is placed on top of a glass substrate, as sketched in Fig. 2.4. In this case the SPP field can leak through the gold layer [67]. Then, this leaked fraction of the field can couple to radiating modes in the glass substrate, since the light cone in glass lies on the right side of the SPP's dispersion relation, as plotted in Fig. 2.2. Due to the conservation of momentum, the resulting radiation, the so-called leakage radiation [67, 68], leaves the gold layer under an angle Θ (see Fig. 2.4). With the absolute value of the SPP wave vector $\beta = |\boldsymbol{\beta}|$, this angle is calculated to be [56]:

$$\Theta = \arcsin\left(\frac{\beta}{n_{\text{glass}} k_0}\right) = \arcsin\left(\frac{n_{\text{eff}}}{n_{\text{glass}}}\right). \tag{2.21}$$

In the case of a vacuum gold interface and a free space wavelength of $\lambda_0 = 980$ nm, the angle is given by:

$$\Theta_{\text{vac}-\text{gold}} \approx 42.5^\circ. \tag{2.22}$$

This rather big angle obtained by freely propagating SPPs makes it necessary to use an objective with a high numerical aperture (NA) to collect this radiation in an experimental environment. Based on the definition of the NA [69], the maximal detectable effective refractive index then equals the value of the NA.

It should be pointed out that this detection method induces an additional loss channel to the system and hence decreases the propagation length below the value calculated in (2.19). Therefore, the chosen thickness of the gold layer has to be a good trade off between a strongly reduced propagation length and the loss of too much intensity in the experimental setup [67].

2.4 Localized surface plasmon polaritons

If the dimensions of the gold interface are drastically reduced, even below the size of one wavelength of the used light source, the previously described propagating SPPs are not an allowed solution of the Maxwell equations any more. In this regime the strong influence of the structure's boundaries leads to the occurrence of the so-called localized SPPs [6, 56]. While this type of SPPs was experimentally investigated in various types of gold structures [70, 71], we restrict ourselves to the type of structure, used in this thesis: gold wires. Here, we will start with the discussion of a single gold wire, which forms a good starting point for the introduction of localized SPPs. Gold wire arrays will be addressed in a later part of this thesis.

If such a gold wire of infinite length in y-direction, a width of w, and a height given by h,

as sketched in the inset of Fig. 2.5, is illuminated by a plane wave propagating in negative x-direction two possible polarization directions have to be treated independently:

Polarization along the y-direction

Similar to an extended gold film, the gold wire supports SPP modes that propagate along the wire. Analog to (2.11), these modes exhibit a strong electric field component along the y-direction. As their counterpart on a flat interface, the wire SPP modes cannot be directly excited from the far-field due to the conservation of momentum. For that reason, these modes play no relevant role within this thesis.

Figure 2.5: The inset shows a single gold wire of width w and height h with an infinite length along the y-direction, placed on top of a glass substrate. The graph describes the modeled absorption spectrum of a typical gold wire, resulting from an illumination with z-polarized light. The displayed spectrum exhibits a resonance at a wavelength of $\lambda_{res} = 610\,\mathrm{nm}$.
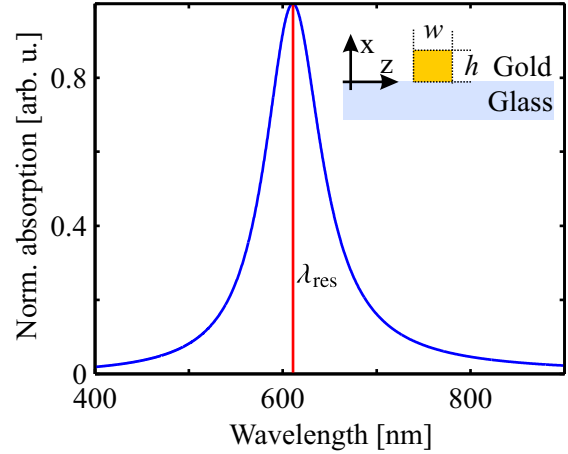
Polarization along the z-direction

If the polarization is rotated to the z-direction, the behavior changes. Due to the small extensions of the wires in this direction, the translational invariance of the system is broken. This facilitates a direct interaction of the incoming electromagnetic wave with the gold's free electrons, leading to the excitation of localized oscillations, the mentioned localized SPPs [6, 56]. Their interaction with the exciting light field can be modeled with a simple oscillator model [72].
In this model, the impinging electromagnetic wave $E(t)$ drives an oscillation of the electron cloud, exhibiting a charge of q_{pl} and mass of m_{pl}. This induces a displacement $\xi_{pl}(t)$ of the electron cloud in the gold wire relatively to the positive background of the nuclei. A counteracting restoring force is then built up by the Coulomb attraction of the positive background. It is proportional to the displacement [73] and furthermore determines the resonance frequency Ω_{pl} of the system. Simultaneously, ohmic and radiation losses induce a damping γ_{pl}. Based on this, the equation of motion of the system corresponds to a single Lorentzian oscillator [72]:

$$\ddot{\xi}_{pl} + 2\gamma_{pl}\dot{\xi}_{pl} + \Omega_{pl}^2 \xi_{pl} = \frac{q_{pl}}{m_{pl}} E(t). \tag{2.23}$$

For a monochromatic excitation ($E(t) = E_0 e^{-\mathrm{i}\omega t}$), the following ansatz can be taken:

$$\xi_{pl}(t) = \tilde{\xi}_{pl}(\omega) e^{-\mathrm{i}\omega t}. \tag{2.24}$$

The resulting frequency dependent displacement can be derived with this ansatz in combination with (2.23). This leads to:

$$\tilde{\xi}_{\text{pl}}(\omega) = \frac{q_{\text{pl}}E_0}{m_{\text{pl}}(\Omega_{\text{pl}}^2 - \omega^2 - 2\mathrm{i}\gamma_{\text{pl}}\omega)}. \tag{2.25}$$

This equation describes an oscillating charge, which naturally induces a dipole moment, given by:

$$p(t) = q_{\text{pl}}\tilde{\xi}_{\text{pl}}(\omega)e^{-\mathrm{i}\omega t}. \tag{2.26}$$

Based on this, the absorption related to the excitation of such an oscillating dipole is proportional to the frequency and the imaginary part of the displacement [72]:

$$\alpha(\omega) \propto \omega \, \Im(\tilde{\xi}_{\text{pl}}(\omega)). \tag{2.27}$$

For some geometries, e.g., cylinders of finite size [73], the resonance frequency and damping can be approximated analytically. In most cases, as in the present one, however, more rigorous simulation methods have to be used to predict the exact resonance frequency and damping of the single structure. Nevertheless, we can deduce a set of parameters from the experimental results discussed in a subsequent chapter of this thesis. A typical absorption spectrum can be described by a resonance at $2\pi c/\Omega_{\text{pl}} = 610\,\text{nm}$ wavelength, a frequency dependent damping of $\gamma_{\text{pl}} = 0.06 \cdot \Omega_{\text{pl}}$, $q_{\text{pl}} = 0.5$, and $m_{\text{pl}} = 1$. The resulting modeled absorption spectrum, is plotted in Fig. 2.5. While the peak position is clearly determined by the spectral position of the resonance, the large width of the peak is induced by the damping of the oscillation.

Gradient index plasmonics: manipulation of Airy SPP beams

Airy SPP beams are the plasmonic analog to Airy beams in free space, as initially proposed by Berry et al. [16]. Similar to their free space counterpart, Airy SPP beams form a class of wave packets that provide interesting features, such as a diffraction-free propagation, self-healing after passing through obstacles, and self-acceleration [19, 20]. This chapter concentrates on the investigation of the destructive-free manipulation of such beams by preserving their unique properties.

For this purpose, the chapter starts with an introduction of freely propagating Airy SPP beams and presents a method to excite them on extended gold films. Subsequently, gradients of the effective refractive index generated by dielectric ramps on the gold film are used to manipulate propagating Airy SPP beams, based on an approach proposed by Liu et al. [23].

After the theoretical discussion of the excitation and manipulation concepts, gray-scale electron beam lithography (gEBL) is introduced as the fabrication method for all dielectric structures. In the final part of this chapter the used experimental setup is introduced. This is followed by the experimental demonstration of bent Airy SPP beams. Herein, this chapter mainly follows Ref. [74].

3.1 Freely propagating Airy SPP beams

To transfer the concept of Airy beams to a plasmonic system, was firstly suggested in the theoretical work of Salandrino et al. [18]. Their argumentation originated from the possibility to describe the evolution of propagating SPPs at a metal dielectric interface by their main field component E_x. Based on (2.9)–(2.11), all other field components of the propagating SPPs can be derived from this component. Thus, in the dielectric half-space, E_x can be written as [18]:

$$E_x = A(y, z)e^{i\beta_0 z}e^{-k_d x}, \tag{3.1}$$

with the transverse beam profile assembled to $A(y, z)$ and the propagation constant β_0, as well as k_d taken from (2.12). With the Helmholtz equation (2.5), the condition (2.12), and

the assumption of a slowly varying transverse beam profile $\left(\frac{\partial^2 A}{\partial z^2} = 0\right)$, an analog to the free 1D-Schrödinger equation can be derived for the transverse beam profile [18]:

$$\frac{\partial^2 A}{\partial y^2} + 2i\beta_0 \frac{\partial A}{\partial z} = 0. \tag{3.2}$$

As it turns out, one possible solution of (3.2) is given by a paraxial Airy SPP beam, being described by [18]:

$$A(y, z) = \text{Ai} \left[Y - \frac{Z^2}{4} + iaZ \right] \cdot \exp \left[a \left(Y - \frac{1}{2}Z^2 \right) \right] \cdot \exp \left[i \left(\frac{1}{2}(a^2 + Y)Z - \frac{1}{12}Z^3 \right) \right], \tag{3.3}$$

with the Airy function Ai [75], the newly defined coordinates $Z = z/(\beta_0 y_0^2)$ and $Y = y/y_0$, the parameter y_0 (determined by the main lobe width $w = 2y_0$), as well as the apodization factor a. While Z and Y simply renormalize the coordinate system, a ensures the paraxiality of the beam by inducing a limited Gaussian shaped field distribution in the k-space [18].

Intensity evolution in a typical system

With (3.3) the intensity distribution of a paraxial Airy SPP beam propagating along an extended vacuum gold interface can be calculated for a typical set of parameters. In case of a free space wavelength of $\lambda_0 = 785$ nm, the propagation constant for this system can be derived to $\beta_0 = n_{\text{eff0}} k_0 = (1.02 + i0.0015)k_0$. Together with an apodization factor of $a = 0.08$ and a main lobe width of $w = 3\,\mu\text{m}$, a paraxial Airy SPP beam exhibits the intensity distribution, depicted in Fig. 3.1 (a).
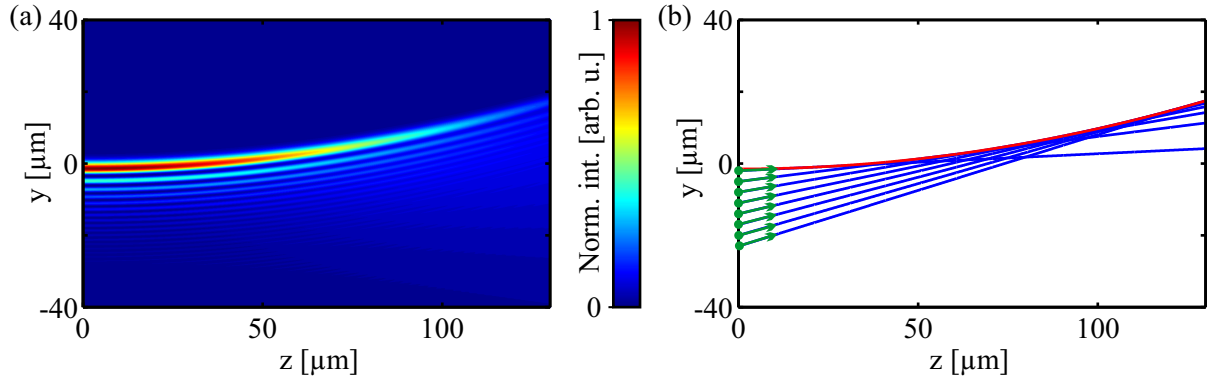
Figure 3.1: (a) Calculated intensity distribution of a paraxial Airy SPP beam. (b) Classical analog to a paraxial Airy SPP beam, built up by particles (green) that are simultaneously launched at different positions in y-direction. Together, they form a limiting caustic trajectory of parabolic shape (red).

This distribution is mainly determined by the Airy function Ai in (3.3). Therefore, it provides alternating dips and peaks of decreasing amplitude in the lower half space, as it is characteristic for an Airy function. In the present case, the overall decreasing intensity of the peaks in y-direction is further increased due to the used apodization factor. Additionally, the argument of

Ai depends on Z^2. Therefore, the main lobe of the paraxial Airy SPP beam follows an upwards bent parabolic trajectory.

By inspecting Fig. 3.1 (a), two further phenomena attract attention. On the one hand the main lobe exhibits only small broadening as expected for a beam, which is barely influenced by diffraction. On the other hand, the intensity is decaying in propagation direction. This originates from the absorption in the gold layer, described by the imaginary part of the effective refractive index (more details on this can be found in the discussion of the propagation length (2.19)).

Since the Airy SPP beam represents a solution of the Schrödinger equation (3.2), a classical analog can be obtained. It deals with families of particles, as they are sketched in Fig. 3.1 (b) [74]. The particles (depicted as green dots) are launched simultaneously with a constant horizontal velocity $[V_z(y, z = 0) = \text{const}]$ and a vertical velocity depending on the initial position $[V_y(y, z = 0) = B\sqrt{-y_i}$, B is a positive constant and y_i the initial coordinate at z = 0]. The limiting caustic trajectory of the particles' trajectories then corresponds to an upwards bent parabola (red line) with a form, determined by the Z-dependence of the Airy function's arguments in (3.3).

Analogously, using the integral equation of the Airy function [75], Airy SPP beams can be represented by a family of plane waves. Based on this, all their unique properties can be explained by constructive interference of these plane waves. This has already been demonstrated for the analog case of free space Airy beams [16, 17].

3.2 Excitation of Airy SPP beams

Since Airy SPP beams have a unique field distribution, their excitation cannot be achieved with a simple straight grating. In this thesis we concentrate therefore on a method proposed in [19, 22] that uses a special type of grating coupler for the excitation. The design, as provided by Alexander Minovich,[1] is sketched on the left side of Fig. 3.2 (a) for a free space wavelength of 785 nm.
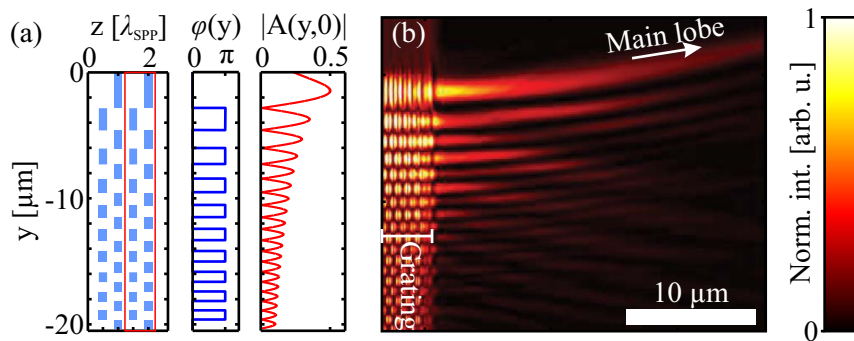
Figure 3.2: (a) Design of the grating used for the excitation of Airy SPP beams, based on [19]. One unit cell of the grating is marked with a red rectangle. Additionally depicted are the phase angle $\varphi(y)$ and the absolute value of $A(y, z = 0)$ as based on Eq. (3.3). (b) Calculated normalized intensity distribution of an excited Airy SPP beam 10 nm above the gold film. The data is taken from Ref. [74].

---

[1] Australian National University (ANU)

The working principle of this grating bases on the properties of $A(y, z = 0)$, as described by (3.3). However, in contrast to the previous section here an apodization factor of $a = 0.04$ and a main lobe width of $w = 1\,\mu m$ is applied. This combination deviates from the paraxial approximation, induces a stronger bending of the beam, and hence makes it possible to image the bending on an even shorter distance [76]. Nevertheless, the desired properties are maintained by this procedure [19].

The substructure of the grating's unit cell, marked by the red box in Fig. 3.2 (a), corresponds to a binary map of the absolute value and the phase angle $\varphi(y)$ of $A(y, 0)$, as extracted from (3.3) and plotted in Fig. 3.2 (a). It can be recognized that $|A(y, 0)|$ exhibits the well-known distribution of an Airy function, consisting of alternating zeros and peaks in the lower half space. It determines the subdivision of the grating in y-direction. The phase angle $\varphi(y)$ is a step function with two different values. It is included in the grating design by shifting each other grating element by $\lambda_{SPP}/2$ in z-direction, corresponding to a relative phase shift of π.

Finally, the unit cell of the grating is periodically repeated 10 times in z-direction with a period of λ_{SPP}, facilitating a coupling of free space radiation to the gold vacuum interface.

FDTD simulations

Since such grating emulates both, amplitude and phase distribution of an Airy SPP beam, it should facilitate its excitation via constructive interference by illumination with a plane wave [19]. In order to test the functionality of dielectric gratings ($n_d = 1.6$) of the proposed design and various thicknesses (h), full field simulations based on the Finite Difference Time Domain (FDTD) method were provided by our collaborators from the ANU. In these simulations, the grating is illuminated with a plane wave of 785 nm wavelength, impinging from the positive x-direction. These simulations showed that the thickness of the grating elements has a strong influence on the intensity distribution of the excited Airy SPP beams. While a grating, consisting of elements with a thickness of 200 nm, leads to a highly disturbed Airy SPP beam, a smaller thickness of $h = 100\,nm$ represents a more optimal choice. The resulting intensity distribution on a plane 10 nm above the gold surface is shown in Fig. 3.2 (b).

Although such grating leads to the excitation of two Airy SPP beams, one propagating to each side of the grating, only the right side is shown. In comparison to Fig. 3.1, these propagating SPPs clearly exhibit the intensity distribution of an Airy SPP beam. The main lobe of this distribution has a parabolic trajectory, pointing upwards with the expected small broadening due to small diffraction losses.

Deviations to the previous calculations

Although, the FDTD simulations resemble the intensity distribution of a paraxial Airy SPP beam, several deviations are apparent. The expected stronger bending of the not strictly paraxial Airy SPP beam, shown in Fig. 3.2, in comparison to the paraxial Airy SPP beam, depicted in Fig. 3.1, can be clearly seen. Furthermore, the FDTD simulation obtains components propagating downwards. However, since the used grating reflects only a binary map of the absolute value of the Airy function, the deviation can be explained by the chosen grating design. In fact, these unwanted components diffract faster than the Airy solution itself and hence do not disturb the

overall behavior [19].

Additionally, it has to be considered that the Airy SPP beam excited by the dielectric grating is truncated due to the finite length of the grating in y-direction. As it is explained more detailed in [19] this truncation differs slightly from a profile given by the exponential apodization, used in (3.3). It therefore leads to a finite so-called diffraction-free zone in propagation direction [76].

3.3 Manipulation of Airy SPP beams

The influence of a linear potential on the properties of propagating Airy wave packets was firstly addressed by Berry and Balazs in their paper on nonspreading wave packets [16]. Recently, Liu et al. transferred this idea to the plasmonic equivalent, the paraxial Airy SPP beams [23]. They proposed to mimic the linear potential by a linear gradient in the effective refractive index, described by $n_{\text{eff}}(y) = n_{\text{eff0}} + y \cdot \Delta n_{\text{eff}}$. This approach is fostered by the possibility to describe the evolution of the transverse beam profile $A(y, z)$ of propagating SPPs in such system by a 1D Schrödinger equation [23]:

$$\frac{1}{2} y_0^2 \frac{\partial^2 A}{\partial y^2} + i\beta_0 y_0^2 \frac{\partial A}{\partial z} + PA = 0, \tag{3.4}$$

including a potential defined as $P = fy/y_0$ with $f = \Delta n_{\text{eff}} \beta_0 k_0 y_0^3$, $\beta_0 = n_{\text{eff0}} k_0$, and k_0, depending on the main lobe width. Note, that for a vanishing gradient ($\Delta n_{\text{eff}} = 0$), this problem reduces again to the 1D-Schrödinger equation, described by (3.2).

In fact, a modified version of the already mentioned paraxial Airy SPP beam is a possible solution of the 1D Schrödinger equation including a non-vanishing linear potential. With the apodization factor a, the main lobe diameter $w = 2y_0$, as well as the new coordinates $Y = y/y_0$ and $Z = z/(\beta_0 y_0^2)$, it is given by [23]:

$$\begin{aligned}
A(y, z) = \text{Ai} &\left[Y - \frac{1}{4} \left(1 + 2f\right) Z^2 + iaZ \right] \\
&\cdot \exp\left[a \left(Y - \frac{1}{2} Z^2 (f + 1) \right) \right] \\
&\cdot \exp\left[i \left(-\left[\frac{f^2}{6} + \frac{f}{4} + \frac{1}{12} \right] Z^3 + \left[\frac{a^2}{2} + (\frac{1}{2} + f)Y \right] Z \right) \right].
\end{aligned} \tag{3.5}$$

In comparison to the free propagating paraxial Airy SPP beam, a non-vanishing gradient in the effective refractive index influences the evolution of the field. However, since (3.5) still represents an Airy function, the unique properties of a paraxial Airy SPP beam are maintained by this procedure. Consequently, the exact behavior is again described by the argument of the Airy function in (3.5). The parameters depend on Z^2 so that a parabolic trajectory of the main lobe can still be anticipated. Furthermore, an $f \neq 0$ influences the slope of the Z^2-dependency, but not its general form. This results in the possibility to control the bending of the Airy SPP beam's trajectory by a gradient in the effective refractive index.

Intensity evolution in a typical system

Based on (3.5), the intensity distribution of a propagating paraxial Airy SPP beam in a typical system can be calculated. For this purpose, we make use of the parameters listed in Sec. 3.1 and a typical gradient of the effective refractive index, which can be experimentally realized (see next section), as it is given by $\Delta n_{\mathrm{eff}} = -0.0319 - i0.0007 \frac{1}{\mu\mathrm{m}}$. The resulting distribution is imaged in Fig. 3.3 (a).
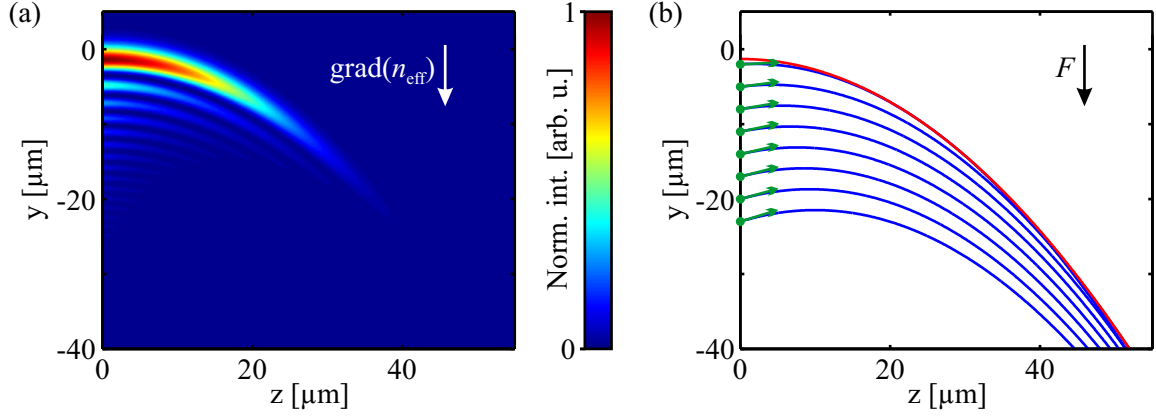

Figure 3.3: (a) Calculated intensity distribution of a propagating paraxial Airy SPP beam in a linear gradient of the effective refractive index. (b) Trajectories (blue) of classical particles (green dots), launched simultaneously at z = 0 and move in presence of an external force F. Their limiting trajectory is depicted in red.

In contrast to the undisturbed paraxial Airy SPP beam, imaged in Fig. 3.1, the main trajectory in the present case is bent downwards in the direction of the gradient, by still exhibiting a main lobe following a parabolic trajectory. The apparent stronger decrease of the overall intensity in propagation direction stems from the imaginary part of the Δn_{eff}. It induces an increasing damping in y-direction and hence, has to be considered in the subsequent experiments.

To understand the behavior of the paraxial Airy SPP beam, the simple classical analog, presented in Sec. 3.1, can be used again. In Fig. 3.3 (b) a family of particles (green dots) is started at z = 0 with the same starting conditions as in the previous chapter [$V_z(y, z = 0)$ = const and $V_y(y, z = 0) = B\sqrt{-y_i}$, as indicated by the green arrows]. Now, the particles move in presence of a constant external force, as for example gravity. Due to this force, the particles trajectories (blue lines) do not remain straight, but become parabolas that are pointing downwards. As a result, the limiting trajectory of all particles (red line) is still of parabolic shape, but bent downwards in this case.

This indicates that in an appropriate external potential the propagation direction of propagating paraxial Airy SPP beams can be manipulated by preserving their unique features.

3.3.1 Effective refractive index profiles

In order to introduce gradients in the effective refractive index of propagating SPPs, the optical properties have to be changed smoothly along the surface. For this purpose, we use in this thesis

a dielectric layer of variable thickness that is deposited on top of the gold film [15, 77]. In comparison to the also used approach of using sub-wavelength dielectric structures, which act as an effective medium and hence allow for the manipulation of SPPs [14], our approach provides a smaller proneness to scattering. Additionally, it is less demanding from a fabricational point of view.

In the following we consider a three layer system, as it is sketched in Fig. 3.4. In comparison to Fig. 2.1, an additional dielectric layer of thickness d with a refractive index higher than the one of vacuum is inserted between the gold and vacuum half-spaces.

Figure 3.4: Three layer system consisting of a dielectric layer with thickness d, sandwiched between the gold and vacuum half-spaces.

The allowed propagating modes in z-direction in this system can be found analogously to the two layer system, discussed in Sec. 2.3. By taking into account the permeabilities of the dielectric (ε_d), vacuum (ε_v), and gold (ε_g) it follows from the Maxwell equations and the continuity of the fields at the boundaries that the following condition has to be fulfilled [77]:

$$\tanh(k_d \varepsilon_d d) = -\frac{k_v k_d + k_d k_g}{k_d^2 + k_v k_g}, \tag{3.6}$$

with

$$k_j = \frac{\sqrt{\beta^2 - \varepsilon_j \frac{\omega^2}{c^2}}}{\varepsilon_j}, \qquad j \in \{v, d, g\}. \tag{3.7}$$

The exact dispersion relation of the system cannot be derived analytically from this formula, but it can be approximated by using Newton's algorithm for each set of wavelength and thickness. The resulting values for a system with a dielectric of thickness d and refractive index $n_d = 1.6$ at a vacuum wavelength of $\lambda_0 = 785$ nm are shown in Fig. 3.5.
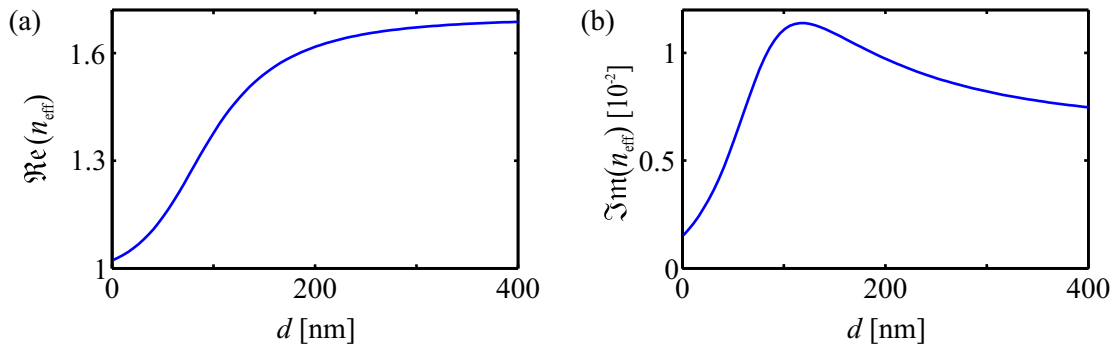

Figure 3.5: Real (a) and imaginary part (b) of the effective refractive index of propagating SPPs in a dielectric layer with thickness d, sandwiched between gold and vacuum for a free space wavelength of $\lambda_0 = 785$ nm.

For thicknesses between 20 nm and 150 nm, the real part of the effective refractive index increases

almost linearly with $\Re(n_{\text{eff}})/d = 2.6 \frac{1}{\mu m}$. The maximum value is reached for a thickness over 400 nm, where it approaches the effective refractive index of propagating SPPs in a two layer system, consisting of solely the dielectric and gold. Due to an increased fraction of the field contained in the lossy gold layer, the imaginary part has a maximum around 180 nm before it approaches also the value of the two layer system.

This behavior indicates that an additional dielectric layer can be used to manipulate propagating SPPs, by changing its thickness. It even facilitates the introduction of a gradient in the effective refractive index by gradually changing the thickness of the additional layer. For example, a linear ascending ramp with thicknesses between 20 nm and 150 nm induces an almost linear gradient in the effective refractive index.

3.3.2 Numerical calculations of Airy SPP beams in dielectric ramps

Based on the last sections of this chapter, it can be anticipated that also non strictly paraxial Airy SPP beams can be manipulated by fabricating dielectric ramps on top of the gold film. The trajectory of such a propagating Airy SPP beam should then be controllable by changing the slope of the dielectric ramps.

In order to test this method, full system FDTD simulations were provided by our collaborators from the ANU. The simulated geometry contains an excitation grating, identically to the one presented in the last section. Additionally, right next to the grating, a ramp made out of a dielectric with refractive index $n_{\text{d}} = 1.6$ and a slope of $8 \frac{nm}{\mu m}$, pointing in negative y-direction, is placed. The ramp begins slightly above the grating at $y_{\text{start}} = 2 \, \mu m$. This leads to a thickness of approximately 20 nm at the start of the grating, being in the linear range of the index-to-thickness dependency (see Fig. 3.5 (a)).

Similar to the above presented simulations, a perpendicular incident plane wave of 785 nm wavelength excites an Airy SPP beam at the grating. This leads to a propagating beam in the ramp, as it is shown in Fig. 3.6 (a). Beginning at the left border of the ramp at z = 0, the main lobe is pointing downwards in direction of the gradient. At the same time it follows a parabolic-like trajectory, similar to the paraxial Airy SPP beam imaged in Fig. 3.3. Additionally, again a strong increase of the damping due to the presence of the ramp is obvious. The remaining deviations can be assigned to the not strictly paraxial type of the Airy SPP beam excited with the chosen type of grating coupler.

Influence of the refractive index gradient

The influence of the gradient of the dielectric ramp on the bending of the Airy SPP beam is tested in an additional simulation of a ramp with a height gradient of $9 \frac{nm}{\mu m}$ and the same starting point ($y_{\text{start}} = 2 \, \mu m$). In order to compare all discussed cases of propagating Airy SPP beams, the trajectories of the main lobes are extracted. The results are shown in Fig. 3.6 (b). Herein, the main lobe of the free propagating Airy SPP beam, extracted from Fig. 3.2, is depicted in red. Furthermore, the one of the $8 \frac{nm}{\mu m}$-ramp is colored blue and the one of the $9 \frac{nm}{\mu m}$-ramp is shown in green. The comparison of all three trajectories reflects the anticipated behavior. While the free propagating Airy SPP beam has an upwards bent trajectory, the other two are bent in direction of the gradient. At the same time the bending is strongly influenced by the gradient of the ramps.
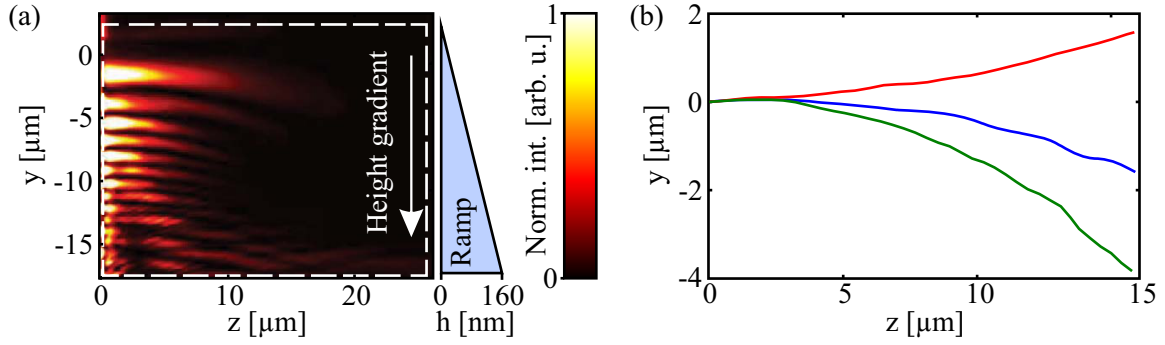
Figure 3.6: (a) Simulated intensity distribution of a propagating Airy SPP beam in a $8\,\frac{nm}{\mu m}$-ramp, $10\,nm$ above the gold film. Directly attached is a sketch of the corresponding ramp. (b) Extracted trajectories of the main lobes of a free propagating Airy SPP beam (red) and beams in a ramp with a height gradient of $8\,\frac{nm}{\mu m}$ (blue) and $9\,\frac{nm}{\mu m}$ (green). Data taken from Ref. [74].

This demonstrates that dielectric ramps of different gradients can be used to bent the trajectory Airy SPP beams in a tailored manner by changing the slope of the ramp.

3.4 Gray-scale electron beam lithography

In order to facilitate the experimental demonstration of freely propagating Airy SPP beams and their manipulation with the proposed method, we have to fabricate dielectric gratings as well as dielectric ramps on top of a gold layer, thin enough to allow the leakage radiation to be emitted. For this purpose we employ gray-scale electron beam lithography (gEBL) with PMMA (Polymethylmethacrylat) as negative tone resist. By this approach, as it is sketched in Fig. 3.7, the fabrication of all dielectric structures on top of the gold film is possible in one step [10]. The fabrication process is discussed in the following.

(a) Substrate preparation

The observation of the SPP propagation requires an oil-immersion microscope lens with large numerical aperture. For this purpose, we choose as substrates standard $170\,\mu m$ cover slides, made out of crown glass (BK-7) that are compatible with our microscope lens. In a first step, these cover slides are roughly cleaned by manually polishing with lens tissues soaked in acetone. Subsequently, they are soaked in acetone in an ultrasonic bath for $60\,min$ for thorough cleaning. After flushing the substrates with ethanol, the solvent residues are removed with pressured nitrogen gas.

On top of the cleaned substrates, a thin layer of approximately $1\,nm$ chromium is evaporated, acting as an adhesion layer for the subsequently evaporated gold. The gold layer itself has a thickness of $60\,nm$. Both metal layers are deposited by thermal evaporation at a typical pressure of $1.5 \times 10^{-6}\,mbar$ and evaporation rates of $1\,\frac{\text{Å}}{s}$ and $2\,\frac{\text{Å}}{s}$, respectively.

In the last step of the preparation, PMMA with a molecular weight of $950\,k$ and dissolved at

Figure 3.7: Basic principle of gray-scale electron beam lithography. (a) PMMA-Au-Cr coated glass substrate (b) Gray-scale electron beam lithography (c) Cross-linked structure in the PMMA layer (d) Resulting structure after removing the exposed areas.
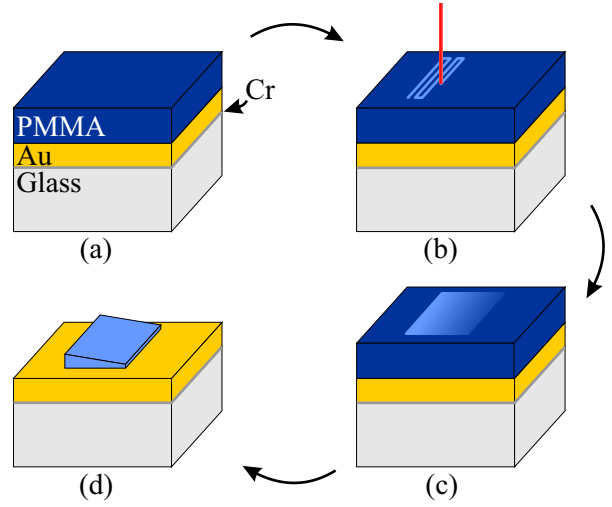
4 % in annisole[2] is spin-coated onto the sample in two steps: (i) For 3 s at 500 rpm, in order to distribute the solution over the sample (ii) For 90 s at 4000 rpm, to achieve a layer thickness of up to 200 nm. Subsequently the film is annealed for 45 min at 175 °C.

(b) Electron beam lithography

The slides are placed in a scanning electron microscope[3] (SEM) with an attached beam control system including a fast beam blanker[4] in order to perform the actual gEBL. Herein, the electron beam is moved over the sample in a controlled manner, tracing simple geometrical structures. The total write field containing such structures has a size of 100 μm times 100 μm. Hence, many of these fields can be placed on one sample.

The local electron beam exposure leads to chemical reactions in the used resist (in this case PMMA), depending on the locally applied dose and the used acceleration voltage. Here, we make use of the effect that for high doses, after a first polymer-chain cutting procedure, a subsequent cross-linking of the polymer-chains takes place in the PMMA layer [78, 79]. Due to the large contribution of the backscattered electrons in this procedure, the cross-linked area grows from the gold layer, resulting in a dose dependent thickness [10]. Since the cross-linked material has a higher resistivity against solvents such as acetone, PMMA effectively acts as a negative tone resist [78, 79].

In order to achieve the cross-linking in this fabrication step, the used nominal dose applied to the sample is 1400 μC/cm^2 (all subsequent mentioned doses are measured relatively to this value). To save time in the lithographic process, a rather large aperture of 30 μm, a low electron acceleration voltage of 10 kV, and a typical step-size of 0.0096 μm are chosen.

---

[2] Supplied by the micro resist technology GmbH, Germany
[3] Sigma, Carl Zeiss Microscopy GmbH, Germany
[4] ELPHY Plus, Raith GmbH, Germany

(c) Cross-linked structures

The actual form of the cross-linked structures in the resist depends not only on the written dose profile of single structures but also on the distances between them. If two structures are placed in near proximity, an overlap of the exposed areas can lead to an effectively increased locally applied dose, accompanied with an increased thickness and width. This effect is called proximity effect [80].

In the present case not only neighboring structures lead to this effect, but also the single lines that build up the structure influence each other. This leads to an increasing thickness for broader structures due to more neighboring lines. Additionally, the width of the structures is strongly affected, due to the absence of neighbors beyond the border of the structure.

Both effects can lead to strong deviations between design and fabricated structure, making it essential to consider the proximity effect in the design.

(d) Resulting structures

Finally, the cross-linked structures are revealed by soaking the sample in acetone for 60 s and subsequently blowing off the remaining residues with pressured nitrogen. As a result only the exposed and cross-linked areas remain on the surface of the sample.

3.4.1 Fabricated samples

In order to realize the manipulation of propagating Airy SPP beams experimentally, single standing PMMA gratings of the proposed design as well as similar gratings beside PMMA ramps of various height gradients are fabricated. All gratings are designed as discussed in Sec. 3.1 and based on sets of rectangles with a dose of 500 % of the nominal dose. An SEM image of such a grating, left to a typical ramp, is shown in Fig. 3.8 (a).
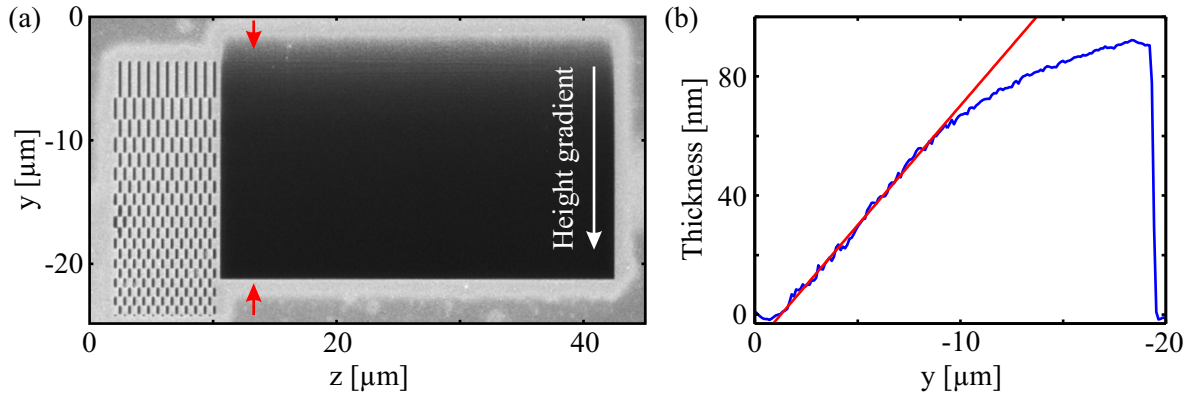

Figure 3.8: (a) SEM image of an Airy SPP beam grating coupler next to a dielectric ramp. (b) AFM measured height (blue) of the ramp imaged in (a) at the position marked by the red arrows, including a linear fit to the first part of the ramp (red). The data taken is from Ref. [74].

The ramps are designed as consisting of rectangles with a length of 32 μm in z-direction and a width of 50 nm in y-direction. The minimal dose is 70 % of the nominal dose, while the maximal

dose is 170 %. The number of elements in y-direction is variable in order to increase or decrease the slope of the ramp. The ramp depicted in Fig. 3.8 (a) has a width of 20 μm in y-direction and consists of 400 rectangles in total, resulting in dose steps of 0.25 percentage points. In addition, ramps with a length of 10 μm and 15 μm are fabricated, leading to larger dose steps of 0.33 and 0.5 percentage points, respectively. The position of the ramps in y-direction in combination with the chosen minimal dose are herein the most critical parameters since they define the real start of the ramp due to the proximity effect.

Sample characterization

In order to characterize the resulting samples after fabrication, an atomic force microscope (AFM) was used to measure the thickness of grating and ramp. The measurements were performed by Jakob Frohnhaus.[5] The measured thickness of the grating elements is approximately 140 nm. The profile of the ramp, depicted in Fig. 3.8 (a), is measured along a line as indicated by the red arrows. The results are plotted in Fig. 3.8 (b) (blue curve). After a linear slope within the first 10 μm, the gradient of the ramp drops. This is due to the fact that the relation between the applied dose and the resulting thickness is not exactly linear. However, the fit of a linear function to the first part of the ramp results in a gradient of approximately $8 \frac{\text{nm}}{\text{μm}}$, which is identical to the one of the simulated dielectric ramp in the last section.
Similar measurements are performed on the second ramp, with a length of 15 μm. The resulting gradient is measured to be approximately $9 \frac{\text{nm}}{\text{μm}}$, while due to the dose profile, the third ramp is expected to be even steeper.

The dimensions of the fabricated gratings and ramps are consistent with the theoretically demanded parameters. In contrast, the refractive index of the used material deviates. While unexposed PMMA has a refractive index of $n_{\text{PMMA}} = 1.49$, the one of cross-linked PMMA is not known exactly. However, in order to cover all fabricational uncertainties, such as a changing density of the cross-linking, we use the refractive index of the cross-linked PMMA as a free parameter to fit the numerical simulations to the experimental data. A good agreement can be found if we choose a value of 1.6 for the cross-linked PMMA in the simulations (see below).

3.5 Optical setup

As introduced in Subsec. 2.3.2, propagating SPPs emit leakage radiation that can be used to image the intensity distribution of propagating SPPs on top of the gold layer. The resulting imaging method is called leakage radiation microscopy (LRM) [67, 68] and can be realized with a setup as it is sketched in Fig. 3.9.
Starting point of the optical setup is the diode laser,[6] operating at a wavelength of 785 nm. In order to obtain a beam with a high quality Gaussian beam profile, the laser is coupled into a single mode fiber. This is necessary since in all experiments on propagating SPPs, the beam shape of the laser beam used for the excitation has a strong influence on the intensity distribution of the propagating SPPs (see Subsec. 2.3.1).

---

[5] Group of PD Dr. Elisabeth Soergel, Physikalisches Institut, Universität Bonn
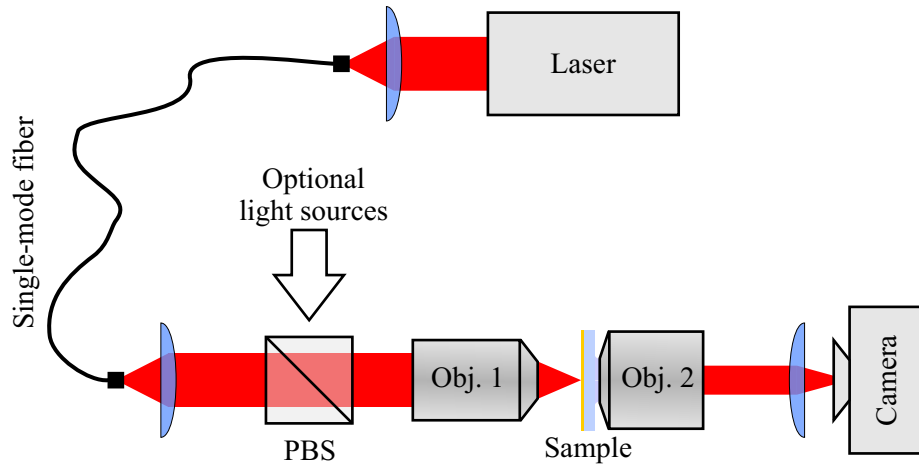[6] LaserBoxx, Oxxius, France

Figure 3.9: Optical setup used for the imaging of the leakage radiation, emitted by propagating Airy SPP beams. Additionally, the light of an optional white light source can be coupled into the beam path via a polarizing beam splitter (PBS), facilitating the imaging of the sample's surface.

The light emitted by the fiber is collimated with a lens. The resulting laser beam subsequently crosses a polarizing beam splitter, which serves two purposes. It ensures the linear polarization, needed for the excitation of propagating SPPs, and it can direct light of any additional collimated light source into the beam path. This allows for example the illumination of the sample with white light.

The laser light and the optional white light are focused onto the sample by making use of Obj. 1.[7] It is mounted on a XYZ translation stage to control the exact focal position on the sample. The gold chromium coated cover glass with a surface manipulated by PMMA structures is mounted in a self manufactured sample holder, attached to a second XYZ translation stage.

In order to collect the radiation leaving the backside of the sample with a high angular range, an immersion oil objective[8] is used (Obj. 2). It is infinity corrected and provides a back focal plane (BFP) laying in a $12\,\text{mm}$ distance from the objective's shoulder. With a numerical aperture of 1.49, it collects the sample's emission up to an angle of approximately 80° relatively to the optical axis. Based on the definition of the numerical aperture and (2.21), this objective hence facilitates the imaging of propagating SPPs with an effective refractive index of up to 1.49. This limit can only be exceeded if the sample provides a high surface roughness, which alters the emission angle of the leakage radiation [81].

Since the employed microscope objective is an infinity corrected objective (image distance is set to infinity), a real image plane of the sample is in the focal point of the lens behind the objective. The size of this image depends on the focal length of the tube lens. Hence, if a camera[9] is placed in the focal point, it captures a real image of the sample's surface. Additionally, due to the emitted leakage radiation, in this case also the intensity distribution of propagating SPPs is imaged [65].

---

[7] Plan N 10x, Olympus Deutschland GmbH, Germany
[8] Apo TIRF 100x, Nikon GmbH, Germany
[9] DCC1545M, Thorlabs GmbH, Germany

3.6 Experimental results

This section concentrates on the experimental investigation of the fabricated samples. It starts with the experimental demonstration of freely propagating Airy SPP beams. Subsequently, the influence of PMMA ramps is discussed in comparison to the presented FDTD simulations.

3.6.1 Excitation of Airy SPP beams

In order to investigate freely propagating Airy SPP beams, a sample containing an isolated standing grating of the proposed design is placed in the optical setup. The 785 nm laser is focused onto the sample, resulting in a spot with a waist radius of approximately 5 μm. In order to excite Airy SPP beams, this grating is placed in the laser spot. The coordinate-system is calibrated with the known dimensions of the grating. This procedure induces an uncertainty of approximately 2% on both axes. The resulting normalized intensity distribution of the excited Airy SPP beam is depicted in Fig. 3.10 on a logarithmic color scale.
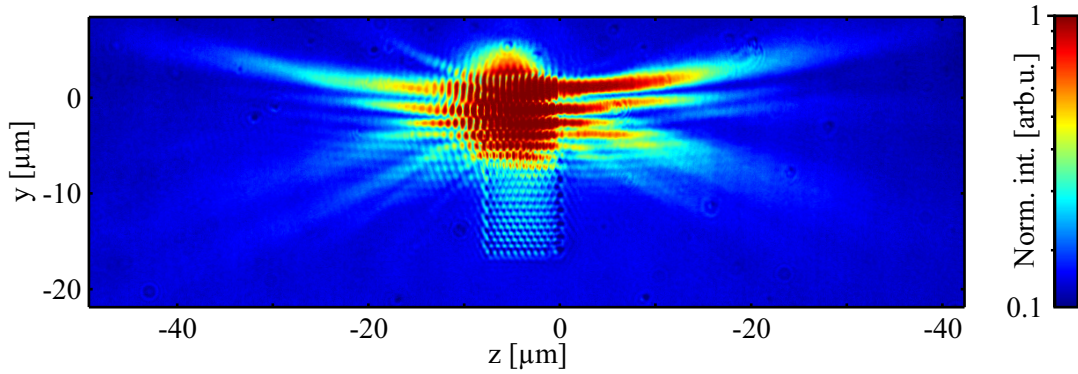

Figure 3.10: Normalized intensity distribution of Airy SPP beams excited by focusing the laser beam on a grating of the proposed design.

The grating itself is visible due to the usage of an additional white light source. It can be recognized that the spot of the laser beam covers the top half of the grating, leading to the excitation of Airy SPP beams. In accordance to the presented FDTD simulations, these beams are propagating in both directions away from the grating. The characteristic upwards bending of the main lobes is clearly visible on a total length of about 40 μm on each side. This short length is a consequence of the short propagation length at a free space wavelength of 785 nm (for more details see the discussion of (2.19)). In addition and accordingly to the presented FDTD simulations, some parts of the SPPs are propagating in negative y-direction without disturbing the Airy distribution of the Airy SPP beams.

A more detailed comparison of the theoretically expected and experimentally demonstrated bending of the main lobes of freely propagating Airy SPP beams takes place at the end of this chapter.

Influence of a longer wavelength

The same experiment is repeated again with a slightly changed optical setup. This new setup contains a laser of 980 nm wavelength, a new camera,[10] and facilitates angular filtering, as it can be used to suppress the exciting laser beam. It will be discussed in more detail in the next chapter.

In order to allow for the excitation of propagating Airy SPP beams at this wavelength, the proposed grating design was adjusted by increasing the inter-unit-cell separations. However, for their excitation, the laser is focused onto the sample similarly to the previous case. The resulting normalized intensity distribution is shown in Fig. 3.11 on a logarithmic color scale.
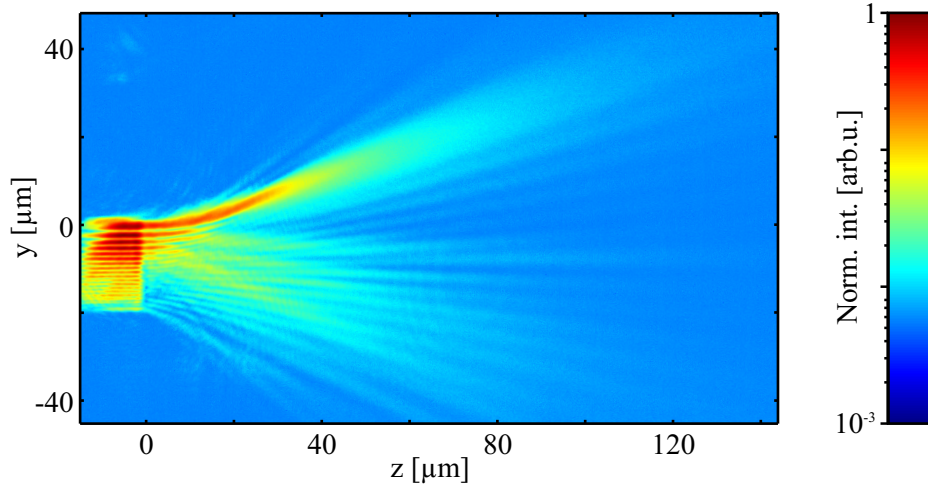

Figure 3.11: Normalized intensity distribution of an Airy SPP beam excited by focusing the 980 nm laser on an adjusted grating.

Since both, laser beam and left propagating Airy SPP beam are blocked by the angular filter, the grating can only be recognized due to the excited SPPs. Similarly to the previous case, the grating leads to the excitation of an Airy SPP beam, propagating in positive z-direction. Here, the upwards bended main lobe of the Airy SPP beam can be seen clearly over more than 100 μm. In comparison to Fig. 3.10 this increased propagation length is striking. However, it has to be considered that the reason for this behavior is the longer free space wavelength. It leads to a longer propagation length due to the decreased losses of gold in this spectral range (see (2.19)). As a result, this makes it possible not only to image the main lobe over a larger distance, but also to detect the broadening of the main lobe starting around z = 60 μm. This can be explained by the small illuminated part of the grating, leading to an additional truncation of the Airy function and hence a diffraction-free zone with finite length [19].

3.6.2 Bending of Airy SPP beams

As a next step the influence of PMMA ramps on propagating Airy SPP beams is investigated. For this purpose the sample is placed in the optical setup in a way that the laser is focused on the

---

[10] Zyla sCMOS, Andor Technology Ltd., United Kingdom

grating beside the ramp with the smallest height gradient ($8\,\frac{nm}{\mu m}$). In order to be in agreement with the FDTD simulations, the 785 nm laser is used again. The resulting logarithmic scaled and normalized intensity distribution, captured with the camera, is depicted in Fig. 3.12. The white light source is again used to ensure the imaging of the ramp and the grating.
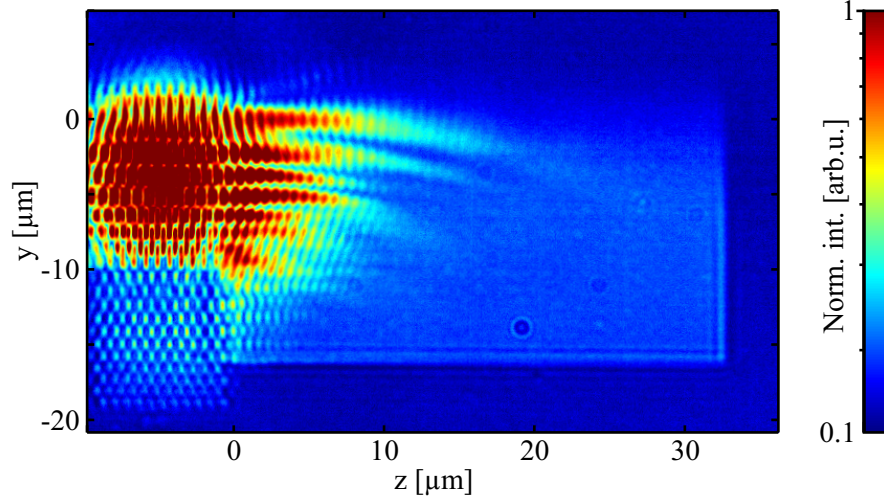

Figure 3.12: Normalized intensity distribution of an Airy SPP beam excited by focusing the 785 nm laser on the grating right next to the $8\,\frac{nm}{\mu m}$-ramp.

The laser beam has once more a waist radius of approximately 5 μm and is focused on the top half of the grating. The Airy SPP beam that propagates freely in negative z-direction is cropped for the sake of clearness. On the right side, the beam directly enters the ramp. Obviously, the main lobe is bent downwards in the direction of the ramp, as expected from the FDTD simulations (for a detailed comparison, see below). In comparison to Fig. 3.10 the influence of a higher damping in thicker PMMA structures can be seen as a fast drop of the intensity in the propagation direction. Additionally, a beating pattern is apparent in the intensity distribution in the inner of the ramp. It stems from interference of the directly transmitted laser beam and the leakage radiation on the camera. Both obtain a different phase on the camera due to the additional phase accumulated by the surface plasmons while propagating in the ramp before the leakage radiation is emitted. These fringes are therefore not visible in the FDTD simulations.

Gradient dependency

In order to investigate the dependency of the Airy SPP beam evolution on the refractive index gradient, the two remaining ramps are investigated. The Airy SPP beam excitation scheme is identical to one in the previous case. We start with the discussion of the structure with the $9\,\frac{nm}{\mu m}$-ramp. Its ramp part is shown in Fig. 3.13 (a).
Obviously, the bending of the Airy SPP beam's main lobe is stronger in comparison to the $8\,\frac{nm}{\mu m}$-ramp (for a detailed comparison see below). Here, an influence of the lower edge of the $9\,\frac{nm}{\mu m}$-ramp is still negligible, since the main part of the intensity distribution is located in the top part of the ramp. In comparison to Fig. 3.12, a stronger damping can be recognized, being in accordance to the higher gradient of the ramp.
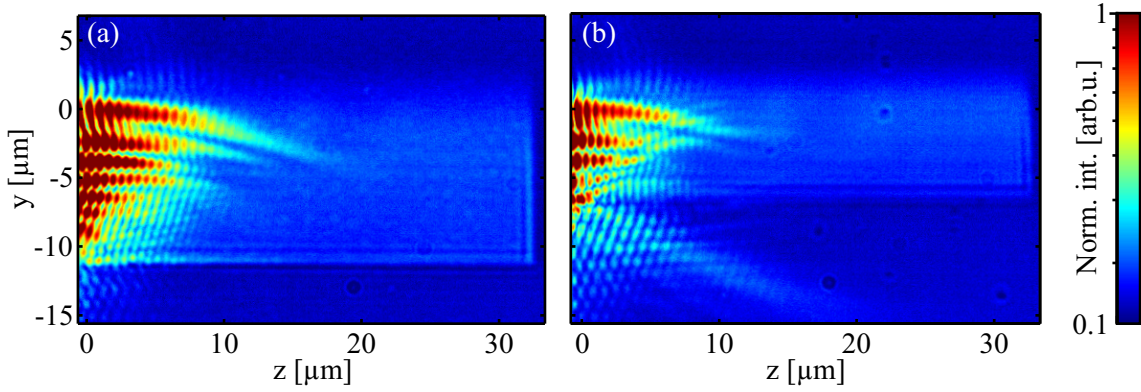
Figure 3.13: Normalized intensity distribution of an Airy SPP beam in the $9\,\frac{nm}{\mu m}$-ramp (a) and in a $10\,\mu m$ long and steeper ramp.

The bending should be more pronounced for the third ramp, fabricated with the steepest dose gradient. The resulting normalized intensity distribution for this ramp is depicted in Fig. 3.13 (b). Also in Fig. 3.13 (b), the excited Airy SPP beam directly enters the ramp after excitation. In contrast to the previous cases, however, the lower edge of the ramp has a strong influence on the beam. This leads to a strong disturbance of the distribution in the ramp due to an additional truncation of the Airy SPP beam. This explains the apparent weaker bending of the main lobe in this case. Hence, this ramp is not used for further investigations.

3.6.3 Comparison of the experimental results and numerical calculations

While the last sections showed that PMMA ramps on top of gold films have a large influence on propagating Airy SPP beams, a direct comparison especially to the theoretical predictions is still missing. To fill this gap, the main lobes of the Airy SPP beams in both FDTD simulations and experimental images are extracted by a manual read out. The read out error of each value, induced by this procedure is $\pm0.1\,\mu m$. The assembled values are plotted in Fig. 3.14.
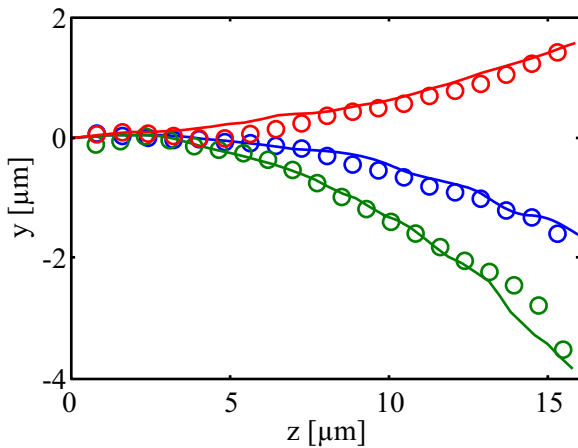

Figure 3.14: Main lobes of Airy SPP beams extracted from the experimental images (circles) and the FDTD simulations (lines). Herein, the freely propagating Airy SPP beam is depicted in red, the results of the $8\,\frac{nm}{\mu m}$-ramp in blue and of the $9\,\frac{nm}{\mu m}$-ramp in green. Data taken from Ref. [74].

The experimental data is marked as circles, while the numerical calculations are depicted as solid lines. The trajectory of the main lobe of a freely propagating Airy SPP beam is shown

in red. The main lobes of the Airy SPP beams propagating under influence of the ramps are depicted in blue (8 $\frac{nm}{\mu m}$-ramp) and green (9 $\frac{nm}{\mu m}$-ramp), respectively.

The behavior expected from the last sections, can be observed clearly. While the freely propagating Airy SPP beam is bent upwards, the Airy SPP beams in the ramps are bent downwards. On this occasion, the gradient of the ramp plays an important role since the steepest ramp leads to the strongest bending, as the deflection after 15 μm has doubled in comparison to the 8 $\frac{nm}{\mu m}$-ramp. It corresponds to even more than an inverted bending behavior in comparison to the freely propagating Airy SPP beam. The experimental data is in excellent agreement with the date extracted from the FDTD simulations.

Plasmonic waveguide arrays as quantum simulators

In this chapter, we will study arrays of evanescently coupled dielectric loaded SPP waveguides (DLSPPWs) as model systems to simulate condensed matter phenomena. After the discussion of the properties of a single DLSPPW, we will present the coupled mode theory that allows us to approximate the evolution of the SPP amplitude in the array.

The second part of this chapter underlines the mathematical analogy between the coupled mode theory (CMT) and the tight binding model that can be used to mimic the temporal evolution of electrons in a crystal lattice. As a concrete example, it is discussed how a simple 1D topological insulator, as described by the Su-Schrieffer-Heeger (SSH) model, can be implemented in a DLSPPW array. Subsequently, the method employed to fabricate such arrays on a gold film is introduced. The evolution of propagating SPPs in these DLSPPW arrays is then investigated with the help of leakage radiation microscopy (LRM) both, in real and Fourier space. Finally, the results are compared to the predictions of the numerical calculations.

4.1 Dielectric loaded surface plasmon polariton waveguides

In order to guide electromagnetic waves in a specific direction, it is necessary to confine them in a structure that prevents the lateral spreading of the waves. For propagating SPPs at a metal dielectric interface this can be achieved for example by fabricating grooves in the metal film [82–84], by reducing the size of the metal film to a wire [85–87], or by introducing an appropriate change to the dielectric medium on top of it [11–13]. In this thesis, we make use of the latter approach and form DLSPPWs consisting of dielectric ridges on top of a gold surface. This approach is less demanding from a fabricational point of view and allows for the tailoring of the DLSPPWs' properties by changing the profile of the ridge [13].

4.1.1 Single DLSPPW

The chosen design of such a DLSPPW is sketched in Fig. 4.1. It consists of a dielectric ridge of width w, height h, and infinite length in the z-direction, surrounded by vacuum, and deposited

on top of gold. In this context, the refractive index of the dielectric (n_d) is assumed to be larger than the one of vacuum ($n_\mathrm{vac} = 1$), while the optical properties of gold are taken from (2.8).

Figure 4.1: Cross cut of a dielectric ridge on top of a gold surface with thickness h, width w, and an infinite length, acting as a waveguide for SPPs propagating in z-direction.
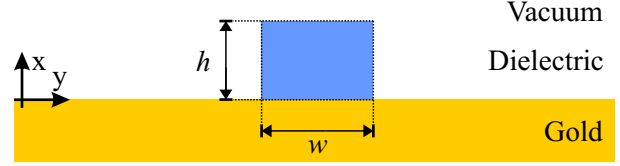
By limiting the dimensions of such ridge below the size of one wavelength of the intended propagating wave ($\lambda_0 = 980\,\mathrm{nm}$), solutions of the Maxwell equations exist with the field propagating along the dielectric ridge and being confined in the transverse direction [13]. These solutions correspond to the eigenmodes of a waveguide, the DLSPPW. As usual for waveguides, their properties highly depend on the used materials and especially on the size of the waveguide's core [69]. Since in the present case the dielectric ridge acts as the core of the waveguide a high influence of the ridge's dimensions on the DLSPPW's properties can be expected.

To get a better insight into these complex dependencies, we use the modal analyzer provided by the finite element method (FEM) solver of the Comsol Multiphysics software package.[1] We assume translational invariance along the z-direction and search for solutions of the Maxwell equations in a 2D geometry as it is imaged in Fig. 4.1. In order to reduce the computational effort, the simulated area is reduced to a rectangular area of $7\,\mu\mathrm{m}$ width and $4\,\mu\mathrm{m}$ height with the dielectric ridge in its center. Corresponding to the anticipated SPP field distribution of the exponentially decaying fields outside the ridge, as boundary conditions at the sides of the area, a zero tangential electrical field is assumed.

The modal solver is now used to find the solutions of the Maxwell equations corresponding to plasmonic modes propagating in the z-direction. With the transversal electric field distribution $\mathbf{E}_0(\mathrm{x}, \mathrm{y})$, they can be described by:

$$\mathbf{E}(\mathrm{x}, \mathrm{y}, \mathrm{z}) = \mathbf{E}_0(\mathrm{x}, \mathrm{y})e^{\mathrm{i}(\beta z - \omega t)}. \tag{4.1}$$

As a result, in case of a dielectric ridge ($n_\mathrm{d} = 1.49$) with height $h = 140\,\mathrm{nm}$, width $w = 250\,\mathrm{nm}$, and the given free space wavelength, only one mode is allowed, making the DLSPPW a single mode DLSPPW. The modal solver provides both, the complex magnetic and electric field distributions, as well as the effective refractive index $n_\mathrm{eff} = 1.058 + \mathrm{i}0.0027$ of the mode, as it is determined by (2.17). The corresponding magnetic field distribution is plotted in Fig. 4.2 (a). While a large fraction of the magnetic field is concentrated at the gold dielectric interface inside of the ridge, the field outside is of evanescent character. This confining behavior of the dielectric ridge is also reflected by the effective refractive index of the mode, which is larger than that of a free propagating SPP. Together, this underlines the expected behavior of a guided SPP mode [13].

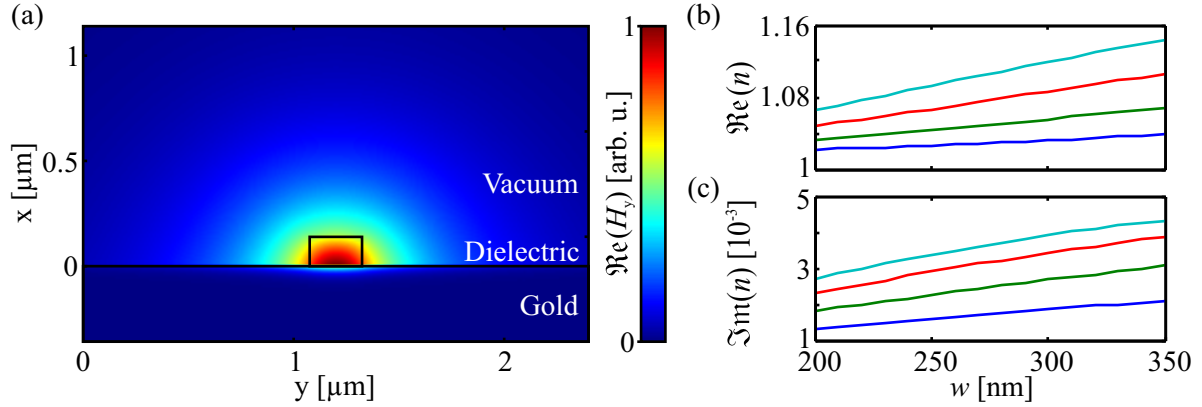[1] Supplied by the Comsol Multiphysics GmbH, Germany.

Figure 4.2: (a) Normalized field plot of $\Re(H_{\mathrm{y}})$ of a DLSPPW with width $w = 250$ nm and height $h = 140$ nm. The corresponding calculated real (b) and imaginary parts (c) of the complex effective refractive index of DLSPPWs as a function of the width w with heights h given by: 90 nm (blue), 120 nm (green), 150 nm (red), 180 nm (cyan).

Size dependence

We performed additional modal analyses in order to investigate the influence of the ridge's dimensions on the wave-guiding properties of the DLSPPW. In that process we considered different widths between 200 nm and 350 nm, as well as heights between 90 nm and 180 nm, in order to cover a wide range of parameters. In each case, the DLSPPW supports only one single mode. The resulting real and imaginary parts of the effective refractive indices, are shown in Fig. 4.2 (b) and (c).

In the given range both parts of the effective refractive index increase almost linearly with increasing height and width. In particular, the increase of the real part can be explained by the increasing influence of the dielectric at larger sizes. The increasing imaginary part stems from a stronger confinement of the field in the dielectric ridge, leading to more interaction with the gold layer and therefore higher losses. Together this let us anticipate that the properties of the DLSPPW can be tuned easily by changing the ridge's dimensions.

Shape dependence

Since a perfect dielectric rectangular ridge cannot be achieved in real experiments, the influence of deviations from this shape on the properties of the DLSPPW has to be discussed. For this purpose we performed additional modal analyses on different dielectric structures with rounded edges. These analyses revealed that a decrease of the cross-sectional area leads to an overall reduction of the effective refractive index. The reason for this behavior is the decreased influence of the dielectric due to its smaller profile.

4.1.2 Coupled mode theory

Now, a second DLSPPW is added to the system, resulting in the structure illustrated in Fig. 4.3. If the center to center distance p between both DLSPPWs is not too large, the field of the first

can penetrate the second one, leading to evanescent coupling [12, 88]. Hence, the field evolution in both DLSPPWs in the propagation direction is not independent any more and an exchange of intensity between both DLSPPWs can be expected.

In a weakly coupled system, the so-called coupled mode theory (CMT) [24, 25] can be used to model the field evolution in the DLSPPWs. For example, in the case of two DLSPPWs the CMT approximates the solution of the system by using the independent eigenmodes of the two single DLSPPWs as a basis.

Figure 4.3: Two dielectric DLSPPWs with permittivities $\varepsilon_v + \varepsilon_{a,b}$ and distance p, surrounded by a material with permitivity ε_v.
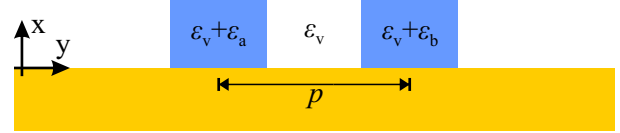
In order to follow this approach, we assume our system to consist out of two DLSPPWs (named a and b) with the permittivities $\varepsilon_v + \varepsilon_{a,b}$. Both are placed on top of a gold substrate and are surrounded by a dielectric with permittivity ε_v. The permittivities are included in the proceeding derivations by the function $\Delta\varepsilon_{a,b}(x, y)$, being equal to $\varepsilon_{a,b}$ only in the respective dielectric ridge.

At first, we treat the two DLSPPWs independently. Since all field components can be deduced from it, in this discussion we concentrate on one electric field component only (see (2.9)–(2.11)). Based on the results of the last section, the eigenmodes then provide the lateral field distribution $E_{a,b}(x, y)$ and the propagation constants $\beta_{a,b} = k_0 n_{\text{eff}:a,b}$. Hence, the electric fields of both modes can be written as [89]:

$$E_{a,b}(x, y, z, t) = E_{a,b}(x, y)e^{i(\beta'_{a,b}z - \omega t)}. \tag{4.2}$$

As propagating electromagnetic waves, both eigenmodes have to fulfill the Helmholtz equation (2.7) for the respective single DLSPPW geometry, given by:

$$\left(\frac{\partial^2}{\partial x^2} + \frac{\partial^2}{\partial y^2} + \frac{\omega^2}{c^2}[\varepsilon_v + \Delta\varepsilon_{a,b}(x, y)]\right) E_{a,b}(x, y) = \beta'^2_{a,b} E_{a,b}(x, y). \tag{4.3}$$

Due to their independence, they constitute a complete orthonormal set of modes, defined by the relation [89]:

$$\int_{-\infty}^{\infty} \int_{-\infty}^{\infty} E_i E_j^* \mathrm{dxdy} = \delta_{ij}\,\frac{2\omega\mu_0}{\beta'_i}, \qquad\qquad i, j \in \{a, b\}, \tag{4.4}$$

with the total power, being normalized to $1\,\text{W}$.

With the knowledge of the properties of both modes, we can now make use of the framework of the CMT. Here, the full field of the electromagnetic wave, propagating in the two DLSPPW structure is approximated by a linear combination of both eigenmodal fields of the single DLSPPWs, weighted with the z-dependent amplitudes $\tilde{A}(z)$ and $\tilde{B}(z)$ [89]:

$$E_{\text{tot}}(x, y, z, t) = \tilde{A}(z) \cdot E_a(x, y, z, t) + \tilde{B}(z) \cdot E_b(x, y, z, t). \tag{4.5}$$

In order to combine the total z-dependence of both summands, we introduce the new amplitudes $A(z) = \tilde{A}(z)e^{i\beta'_a z}$ and $B(z) = \tilde{B}(z)e^{i\beta'_b z}$. Then, by making use of (4.2), the total field can be

rewritten as:

$$E_{\text{tot}}(x, y, z, t) = A(z)E_{\text{a}}(x, y)e^{-i\omega t} + B(z)E_{\text{b}}(x, y)e^{-i\omega t}. \tag{4.6}$$

The field of the two DLSPPW structure has to fulfill the following Helmholtz equation of the complete geometry:

$$\left(\frac{\partial^2}{\partial x^2} + \frac{\partial^2}{\partial y^2} + \frac{\partial^2}{\partial z^2} + \frac{\omega^2}{c^2}[\varepsilon_v + \Delta\varepsilon_{\text{a}}(x, y) + \Delta\varepsilon_{\text{b}}(x, y)] \right) E_{\text{tot}}(x, y, z) = 0. \tag{4.7}$$

In the weakly coupled case, considered here, the influence of one DLSPPW on the other corresponds to a small perturbation so that we can restrict ourselves to amplitudes that vary slowly in the z-direction. This assumption implies:

$$\frac{d^2\tilde{A}}{dz^2} = \frac{d^2\tilde{B}}{dz^2} = 0. \tag{4.8}$$

By inserting (4.6) into (4.7) and by using (4.3) as well as (4.8), the following condition can be derived:

$$2i\beta_{\text{a}}'\frac{dA}{dz}E_{\text{a}} + 2i\beta_{\text{b}}'\frac{dB}{dz}E_{\text{b}} = -2\beta_{\text{a}}'^2 E_{\text{a}}A - \frac{\omega^2}{c}\Delta\varepsilon_{\text{b}}AE_{\text{a}} - 2\beta_{\text{b}}'^2 E_{\text{b}}B - \frac{\omega^2}{c}\Delta\varepsilon_{\text{a}}BE_{\text{b}}. \tag{4.9}$$

A multiplication with E_{a}^* and an integration over the xy-plane, by using (4.4), leads to:

$$2i\beta_{\text{a}}'\frac{dA}{dz}\frac{2\omega\mu_0}{\beta_{\text{a}}'} = -2\beta_{\text{a}}'^2\frac{2\omega\mu_0}{\beta_{\text{a}}'}A - \frac{\omega^2}{c}A\iint\Delta\varepsilon_{\text{b}}E_{\text{a}}E_{\text{a}}^*\text{dxdy} - \frac{\omega^2}{c}B\iint\Delta\varepsilon_{\text{a}}E_{\text{b}}E_{\text{a}}^*\text{dxdy}. \tag{4.10}$$

This can be rewritten as:

$$\frac{dA}{dz} = i(\beta_{\text{a}}' + \kappa_{\text{aa}})A + iC_{\text{ab}}B, \tag{4.11}$$

with the overlap integrals

$$\kappa_{\text{aa}} = \frac{\omega\varepsilon_0}{4}\iint E_{\text{a}}^*\Delta\varepsilon_{\text{b}}E_{\text{a}}\text{dxdy}, \tag{4.12}$$

$$C_{\text{ab}} = \frac{\omega\varepsilon_0}{4}\iint E_{\text{a}}^*\Delta\varepsilon_{\text{a}}E_{\text{b}}\text{dxdy}. \tag{4.13}$$

Analogously, by a multiplication of (4.9) with E_{b}^*, and a subsequent integration over the xy-plane, a similar equation results for the field in the second DLSPPW:

$$\frac{dB}{dz} = i(\beta_{\text{b}}' + \kappa_{\text{bb}})B + iC_{\text{ba}}A, \tag{4.14}$$

with

$$\kappa_{\text{bb}} = \frac{\omega\varepsilon_0}{4}\iint E_{\text{b}}^*\Delta\varepsilon_{\text{a}}E_{\text{b}}\text{dxdy}, \tag{4.15}$$

$$C_{\text{ba}} = \frac{\omega\varepsilon_0}{4}\iint E_{\text{b}}^*\Delta\varepsilon_{\text{b}}E_{\text{a}}\text{dxdy}. \tag{4.16}$$

The newly defined overlap integrals κ_{aa} and κ_{bb} can be understood as a measure for the perturbation of a single DLSPPW's mode, induced by its neighbor. Hence, they correspond to a correction of the propagation constants and can be included in a new definition of the propagation constants, given by $\beta_a = \beta_a' + \kappa_{aa}$ and $\beta_b = \beta_b' + \kappa_{bb}$. With this, the coupled equations can be simplified to [24]:

$$\frac{\mathrm{d}A}{\mathrm{d}z} = \mathrm{i}\beta_a A + \mathrm{i}C_{ab}B, \tag{4.17}$$

$$\frac{\mathrm{d}B}{\mathrm{d}z} = \mathrm{i}\beta_b B + \mathrm{i}C_{ba}A. \tag{4.18}$$

This formula reveals that the overlap integrals (C_{ab} and C_{ba}) of both modes describe the interaction of the fields in both DLSPPWs and thus act as coupling constants.

In order to simplify the solution of this system of two coupled differential equations, the problem can be written as a matrix equation:

$$\frac{\mathrm{d}}{\mathrm{d}z}\boldsymbol{a}(z) = \mathbf{A}_{\mathrm{CMT}}\,\boldsymbol{a}(z), \tag{4.19}$$

with the system matrix $\mathbf{A}_{\mathrm{CMT}}$ and the local amplitudes $\boldsymbol{a}(z)$ in the DLSPPWs, given by:

$$\boldsymbol{a}(z) = \begin{pmatrix} A(z) \\ B(z) \end{pmatrix}, \qquad \mathbf{A}_{\mathrm{CMT}} = \mathrm{i}\begin{pmatrix} \beta_a & C_{ab} \\ C_{ba} & \beta_b \end{pmatrix}. \tag{4.20}$$

With this as a basis, the resulting local amplitudes of in each DLSPPW, as described by the components $a_m(z)$ of $\boldsymbol{a}(z)$, can be calculated by an eigenmode expansion on the basis of the eigenvalues and eigenvectors of $\mathbf{A}_{\mathrm{CMT}}$.

Eigenmode expansion

In the following, we consider a M-dimensional matrix with eigenvalues χ_j and eigenvectors V_j ($j \in \{1 \dots M\}$). With the initial condition $a_m(0)$, the evolution of the electromagnetic field $a_m(z)$ along the z-direction in the m-th DLSPPW can be derived by an eigenmode expansion [90]:

$$a_m(z) = \sum_{j=1}^{M} \eta_j e^{\chi_j z} V_{m,j}, \tag{4.21}$$

with

$$\eta_j = \sum_m V_{j,m}^{-1} a_m(0), \tag{4.22}$$

and the components of the eigenvectors, being described by $V_{m,j}$. This expansion describes the field in the m-th DLSPPW as a superposition of plane waves (the eigenmodes), given by $e^{\chi_j z} V_{m,j}$, and weighted with the initial condition η_j. Herein, the eigenvectors V_j act as the amplitude distributions of the eigenmodes of the two DLSPPW system, possessing propagation constants $k_j = \chi_j/\mathrm{i}$. The input of the system ($a_m(0)$) finally determines which eigenmodes are excited.

4.1.3 System of two identical DLSPPWs

A simple system of two identical DLSPPWs ($\beta_a = \beta_b =: \beta$) can be used to understand the behavior of coupled DLSPPWs. In this case both coupling coefficients are also identical ($C_{ab} = C_{ba} =: C$) so that the eigenvalues and corresponding eigenvectors of this system can be calculated from (4.20). This results in:

$$\chi_1 = \mathrm{i}(\beta - C), \qquad\qquad V_1 = \begin{pmatrix} -1 \\ 1 \end{pmatrix}, \qquad\qquad (4.23)$$

$$\chi_2 = \mathrm{i}(\beta + C), \qquad\qquad V_2 = \begin{pmatrix} 1 \\ 1 \end{pmatrix}. \qquad\qquad (4.24)$$

These eigenvectors and eigenvalues represent the two eigenmodes of the system. The first one, described by (4.23), has an asymmetric amplitude distribution given by V_1, while the second one, given by (4.24), exhibits a symmetric amplitude distribution. At the same time, the propagation constants ($k_j = \chi_j/\mathrm{i}$, for $j \in \{1, 2\}$) of both modes split up symmetrically with respect to the propagation constant of a single DLSPPW system, given by β.
With a typical input field distribution of $a_m(0) = (1, 0)$ and (4.21)–(4.22), the field evolution in the z-direction can be derived for each DLSPPW:

$$a_1(z) = \frac{1}{2}e^{\mathrm{i}k_1 z} + \frac{1}{2}e^{\mathrm{i}k_2 z}, \qquad\qquad (4.25)$$

$$a_2(z) = -\frac{1}{2}e^{\mathrm{i}k_1 z} + \frac{1}{2}e^{\mathrm{i}k_2 z}. \qquad\qquad (4.26)$$

These equations describe a superposition of two modes, which are excited simultaneously. Because of their phase difference ($\Delta\phi(z) = (k_2 - k_1)z$), this superposition results in a beating pattern. Thus, after a given distance L_{Coupl}, a full exchange of intensity between both DLSPPWs takes place. This so-called coupling length, corresponds to the distance after which the phase difference equals π. Together with (4.23)–(4.24) this leads to:

$$L_{\mathrm{Coupl}} = \frac{\pi}{k_2 - k_1} = \frac{\pi}{2C}. \qquad\qquad (4.27)$$

Modal Analysis

To be able to utilize the CMT, the knowledge of the effective refractive indices of the single DLSPPWs as well as the coupling constants is essential. While the effective refractive indices of the single DLSPPWs were already discussed in Subsec. 4.1.1, the coupling constants are still unknown. This gap can be filled by using the modal solver of Comsol Multiphysics, again.
The complete simulated area, again, corresponds to a rectangle of 7 μm width and 4 μm height, now with the two DLSPPW structure in its center. Identical to the simulations performed for the one DLSPPW system, as boundary conditions zero tangential electrical fields at the sides of the rectangular area are chosen. The modal solver is then used to find the two allowed modes of the system, consisting of the two DLSPPWs with a width of 250 nm, a height of 140 nm, and a center to center distance of 600 nm. The resulting real parts of the H_y-fields of both modes are
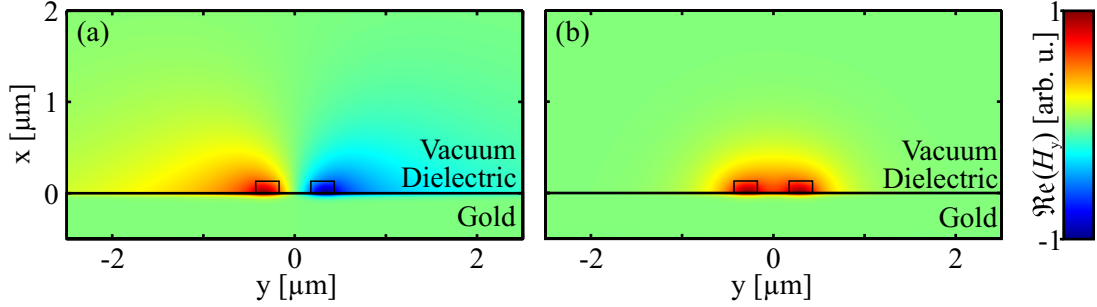
imaged in Fig. 4.4 (a) and (b).

Figure 4.4: Resulting simulated H_y-field of two DLSPPWs with a center to center distance of 600 nm, providing an asymmetric (a) and a symmetric mode (b).

Both modes can be clearly identified as an asymmetric (Fig. 4.4 (a)) and a symmetric mode (Fig. 4.4 (b)), in accordance to the results expected from the CMT. While the symmetric mode is tightly confined to the DLSPPWs, the asymmetric mode is broadly spread.

The effective refractive indices of both modes, provided by the simulation, are $k_1/k_0 = 1.015 + i0.0018$ and $k_2/k_0 = 1.084 + i0.003$, respectively. With this and by using (4.27), the coupling constant of this system can be calculated to $C = 0.22 + i0.0035 \, \frac{1}{\mu m}$. While the real part of C describes the actual coupling between the DLSPPWs, from (4.17) and (4.18) it can be deduced that the imaginary part characterizes an additional damping of the system induced by the coupling.

Field evolution

With the calculated values for the coupling constant and effective refractive indices of the two DLSPPW system, the field evolution in the propagation direction can be calculated by using (4.25)–(4.26). The resulting intensity evolution in the z-direction is then simply given by the squared absolute value of the field.

In order to obtain a representation of the data which resembles the experimental leakage radiation images, a 2D-plot of the intensity evolution in the z-direction is produced. For this purpose, the intensity distribution in each DLSPPW (as calculated from (4.25) and (4.26)) is plotted as a horizontal, colored pixel line. These lines are copied several times to achieve an aspect ratio corresponding to the chosen distances. Finally, the space in between the waveguides is padded with lines of zero intensity. The resulting distribution is shown in Fig. 4.5 (a).

Corresponding to the assumed input field distribution ($a_m(0) = (1,0)$), the electromagnetic wave in the two DLSPPW system is excited at z = 0 in the top DLSPPW. Due to the evanescent coupling, the intensity is periodically exchanged between both DLSPPWs, with a characteristic length given by $L_{Coupl} \approx 7 \, \mu m$. At the same time, due to the damping, the overall intensity is decreasing along the propagation direction.
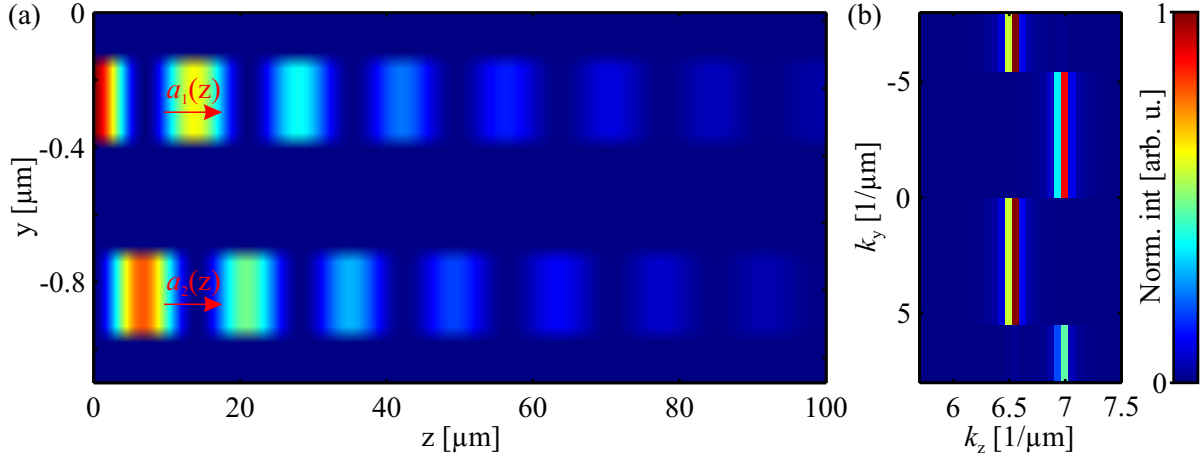
Figure 4.5: (a) Field evolution of an electromagnetic wave in two coupled DLSPPWs with a center to center distance of 600 nm. (b) A 2D FFT of the field distribution corresponding to (a).

Fourier analysis

In an experiment, the exact values of the effective refractive indices and the coupling constants are usually not known. Using Fourier space imaging (see below in the experimental part of this chapter), it is possible to image also the k-space intensity distribution of propagating SPPs in DLSPPWs. From this distribution all necessary parameters can be deduced.

This idea can be theoretically reproduced, by applying a 1D Fourier transform on the field distribution of the two coupled DLSPPWs, represented by (4.25) and (4.26). This leads to:

$$\mathcal{F}\{a_1(z)\}(k) = 2\pi(-\delta(k - k_1) + \delta(k - k_2)), \tag{4.28}$$

$$\mathcal{F}\{a_2(z)\}(k) = 2\pi(\ \ \delta(k - k_1) + \delta(k - k_2)). \tag{4.29}$$

Obviously, these Fourier transforms are nonzero only for the values of the propagation constants of the excited eigenmodes. Hence, it is a promising method to measure the effective refractive indices in an experimental environment.

To imitate now the experimental case, a 2D fast Fourier transform (FFT) is performed on the complex field distribution, corresponding to the intensity distribution shown in Fig. 4.5 (a). The resulting Fourier intensity distribution is depicted in Fig. 4.5 (b).

The plot shows the excited eigenmodes of the system in the k-space. Hence, two different levels in the z-direction can be recognized, corresponding to the two eigenmodes of the system, obtaining the two propagation constants k_1 and k_2. The higher value in k_z-direction corresponds to the symmetric eigenmode of the system, while the lower corresponds to the asymmetric eigenmode.

4.1.4 Accuracy of the coupled mode theory

The CMT allows to calculate the evolution of the SPP distribution in the waveguides with little computational effort, once the effective refractive indices and coupling constants are known.

However, it is not obvious whether the underlying assumption of weak coupling is fulfilled in our structures. In order to fill this gap, the CMT and Comsol Multiphysics simulations are compared in the following, regarding the mode profile and the coupling constants.

Mode profile

While the mode profile simulated with Comsol Multiphysics is already displayed in Fig. 4.4, the field distribution approximated by the CMT, can be derived as a superposition of the modal field distributions of the single DLSPPWs, weighted with the components of the eigenvectors (see (4.6)). With the components $V_{i,j}$ ($i, j \in \{1, 2\}$) as well as the magnetic field distributions of the single DLSPPWs H_{ya} and H_{yb}, this results the two modal field distributions:

$$H_{y,j} = V_{1,j} H_{ya} + V_{2,j} H_{yb} , \qquad\qquad j \in \{1, 2\}. \qquad\qquad (4.30)$$

Discussing again a system with two DLSPPWs of 250 nm width, 140 nm height, and a center to center distance of 600 nm, the field distributions of each DLSPPW can be extracted from Fig. 4.2. With the eigenvalues, taken from (4.23) and (4.24), the resulting normalized H_y-field can be calculated. The resulting real part of H_{y1} and H_{y2} is plotted in Fig. 4.6 (a) and (b), respectively.
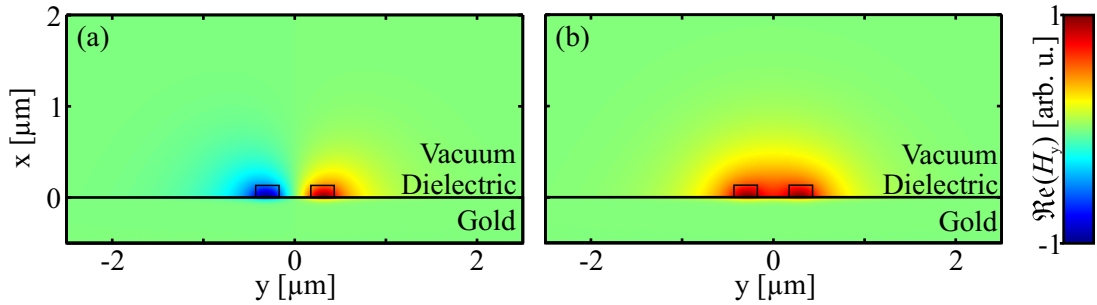

Figure 4.6: Real part of H_{y1} (a) and H_{y2} (b), describing the asymmetric and symmetric mode of a two DLSPPW system obtaining a center to center distance of 600 nm, as calculated by using the CMT.

As expected, the symmetric and asymmetric modes can be clearly distinguished. In comparison to Fig. 4.4, large differences are obvious primarily in the evanescent part of the field beside the DLSPPWs. In order to simplify the comparison, in Fig. 4.7 line plots of the electric field 10 nm above the gold surface are plotted for the asymmetric (a) and symmetric (b) mode. The CMT calculations are depicted in green, while the Comsol Multiphysics simulations are shown in blue. For both modes, deviations between the CMT calculations and the Comsol Multiphysics simulations are evident. The deviation of the spatially wider asymmetric mode is, however, more pronounced.

In order to check the dependence of these deviations on the distance between the DLSPPWs, the same simulations and calculations are performed again for a center to center distance of 800 nm. In order to simplify the comparison also here, the field along a line located 10 nm above the gold surface is extracted and imaged in Fig. 4.7 (c) and (d). Again, deviations of the CMT calculations from the Comsol Multiphysics simulations can be observed. However, in contrast to the smaller DLSPPW distance, the differences decreased.
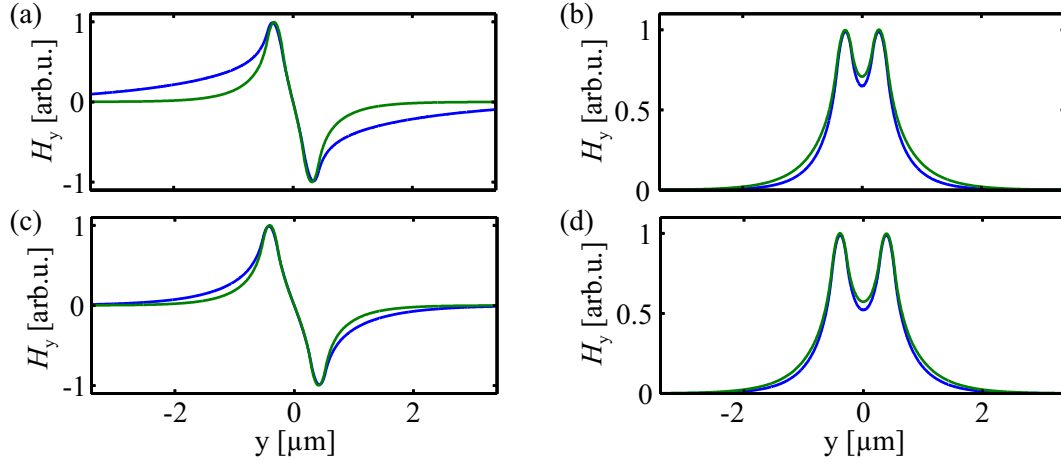
Figure 4.7: Line plots of the asymmetric (a) and symmetric (b) mode of a two DLSPPW system with a center to center distance of 600 nm. The data lines are extracted from the field plots obtained from the modal analyses (blue) and the CMT calculations (green), 10 nm above the gold surface. (c) and (d) show the corresponding plots for an increased center to center distance of 800 nm.

As the Comsol Multiphysics simulations are based on a rigorous solution of the Maxwell equations, deviations between the two sets of calculations can be attributed to the approximations made in the CMT. These deviations are smaller for larger distances and hence weaker coupling. In the light of this discussion, one has to take care when comparing experimental data with results of the CMT calculations.

Coupling constants

Since the coupling constants correspond to the overlap integrals of the fields in each waveguide, it can be expected that they are also affected by the deviated field distributions. In order to test the dependency of the coupling constants on the DLSPPWs' separations, Comsol Multiphysics simulations were performed for systems with center to center distances between 540 nm and 3300 nm, without changing the profile of the DLSPPWs. The resulting effective refractive indices of the symmetric (n_{sym}) and asymmetric modes (n_{asym}) are plotted in Fig. 4.8 (a).
With an increasing distance, the difference of the effective refractive indices reduces, due to the decreasing influence of the DLSPPWs on each other. As a result, for large separations both values approach the value of a single DLSPPW system. In contrast to the CMT, the modes exhibit an asymmetric splitting with respect to this effective refractive index. In fact, the values of the asymmetric mode deviate stronger in comparison to the values of the symmetric mode. This behavior is, however, in accordance to the deviations observed in the comparison of the modal field distributions calculated from the Comsol Multiphysics simulations and the CMT calculations, respectively.

Nevertheless, by using (4.27), the Comsol Multiphysics based coupling constants can be calculated from the values depicted Fig. 4.8 (a). The real and imaginary parts of the coupling constants as a function of the distance are plotted in Fig. 4.8 (b) and (c). For larger distances, the real part of the coupling constants decreases as the perturbation of the second DLSPPW gets
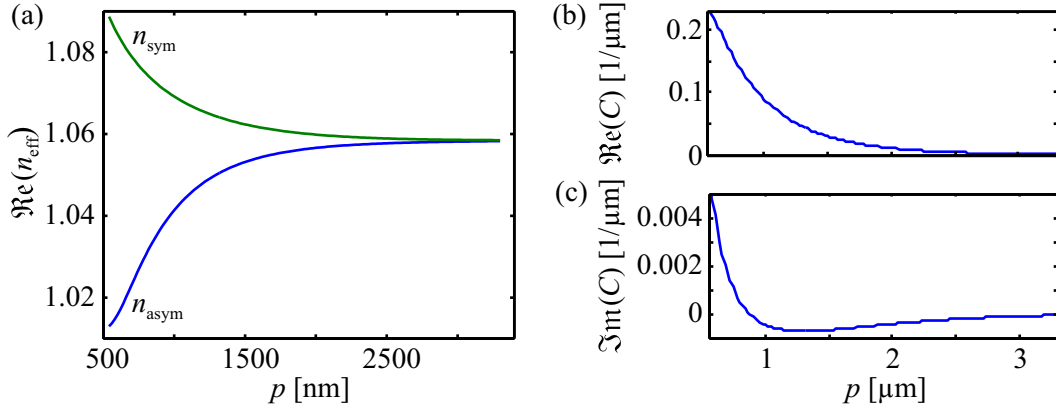
Figure 4.8: (a) Effective refractive indices of the symmetric (green) and asymmetric (blue) modes in two DLSPPW systems with different DLSPPW separations. (b) Real part and (c) imaginary part of the corresponding coupling constants.

smaller and smaller. Furthermore, due to the asymmetric splitting of the effective refractive indices, the imaginary part has a minimum and becomes negative at distances in the range of $1200\,\mu m$, before it approaches zero. However, this reduction of the losses, induced by the negative coupling constants, is small in comparison to the losses in each DLSPPW (see Fig. 4.2 (c)). Hence, it does not play an important role here.

4.1.5 The coupled mode theory in DLSPPW arrays

We can easily extend our discussion of the evolution of an electromagnetic wave in a system of two coupled DLSPPWs to systems with more than two DLSPPWs. In this thesis, we will restrict ourselves to a system of M DLSPPWs, considering only next neighbor coupling, as it is sketched in Fig. 4.9.
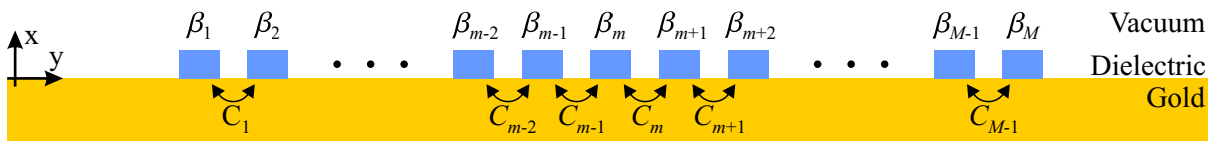

Figure 4.9: A DLSPPW array on top of a gold surface with coupling constants C_m and propagation constants β_m.

Completely analogue to (4.17) and (4.18), the spatial development of the field amplitude in the m-th DLSPPW can be written as [31]:

$$\frac{d}{dz}a_m(z) = iC_{m-1}\,a_{m-1}(z) + i\beta_m\,a_m(z) + iC_m\,a_{m+1}(z)\,, \qquad (4.31)$$

with the amplitudes $a_m(z)$ in each DLSPPW, the coupling constants C_m corresponding to the coupling between the DLSPPWs m and $m+1$, and the propagation constants β_m in each DLSPPW.

This system of coupled differential equations can, similarly to the two DLSPPW system (see (4.19)), be rewritten as a matrix equation with the system matrix $\mathbf{A}_{\mathrm{CMT}}$ [90]:

$$
\mathbf{A}_{\mathrm{CMT}} = \mathrm{i}
\begin{pmatrix}
\beta_1 & C_1 & & & & & \\
C_1 & \beta_2 & C_2 & & & \text{\huge 0} & \\
 & & \ddots & & & & \\
 & & C_{m-1} & \beta_m & C_m & & \\
 & & & & \ddots & & \\
\text{\huge 0} & & & & C_{M-2} & \beta_{M-1} & C_{M-1} \\
 & & & & & C_{M-1} & \beta_M
\end{pmatrix} .
\tag{4.32}
$$

With this notation, the complicated problem for M DLSPPWs also reduces to an eigenvalue problem. Similar to the two DLSPPW system, the field evolution in the z-direction can be calculated by applying an eigenmode expansion, based on (4.21) and (4.22).

4.1.6 Comsol Multiphysics based eigenmode expansion

With knowledge of the limits of the CMT, the necessary next step is to find an alternative approach to efficiently calculate the intensity evolution in a DLSPPW array. Due to the large size of the simulated area, full field simulations are rather time and memory consuming. Therefore, we make use of the fact that the eigenvectors and eigenvalues, used in the CMT, can also be derived from the Comsol Multiphysics modal analyses. This stems from the fact that the eigenvectors correspond to the normalized amplitude distribution of the eigenmodes, while the eigenvalues describe the propagation constant of these eigenmodes. Performing an eigenmode expansion with these eigenvalues and eigenvectors has the advantage that it is both, numerically very efficient and not restricted to the conjectured values of the effective refractive index and the coupling constants.

The resulting numerical procedure employed in this thesis will be introduced with the two DLSPPW system, serving as example.

Two DLSPPW system

A CMT-like eigenvector of the asymmetric mode of the present two DLSPPW system can be derived from the lines in Fig. 4.7 (a) and (c), by taking one field value out of the center of each DLSPPW. These values are composed to a two element vector and subsequently normalized. Analogously, the eigenvector of the symmetric mode can be approximated from Fig. 4.7 (b) and (d). The resulting vectors form together the matrix of CMT-like eigenvectors $\mathbf{V}$. Simultaneously, the eigenvalues can be derived from the effective refractive indices, provided by Comsol Multiphysics for the two DLSPPW system. They are placed on the diagonal of a new matrix $\boldsymbol{\Lambda}$.

The system matrix $\mathbf{A}_{\mathrm{COM}}$ can then be calculated by a simple transformation from the eigenvector space to the real space:

$$
\mathbf{A}_{\mathrm{COM}} = \mathbf{V}\boldsymbol{\Lambda}\mathbf{V}^{-1} .
\tag{4.33}
$$

The resulting matrix is of the same form as the system matrix resulting from the pure CMT, shown in (4.20). Hence, the propagation constants can be calculated from its diagonal and the coupling constants from the neighboring entries. Additionally, with this matrix the spatial field evolution can be calculated, analogously to the CMT.

4.2 DLSPPW arrays as condensed matter simulators

The spatial evolution of the SPP field distribution in a DLSPPW array, approximated by the CMT (see (4.31)), has a remarkable similarity with the temporal evolution of an electron's probability amplitude in a lattice, according to the condensed matter tight binding model. This is fostered by the possibility to describe the temporal evolution of the probability ψ_m of an electron to be at the lattice site m by [26]:

$$\frac{\mathrm{d}}{\mathrm{d}t}\psi_m(t) = -\mathrm{i}T\,\psi_{m-1}(t) - \mathrm{i}E_m\,\psi_m(t) - \mathrm{i}T\,\psi_{m+1}(t)\,, \tag{4.34}$$

with the nearest neighbor intersite overlap integrals T and the on-site energies E_m.

The direct comparison to (4.31) reveals that the temporal evolution of the electron can be simulated by the spatial evolution of propagating SPPs in a coupled DLSPPW array. In this case the propagation constants correspond to the on-site energies E_m, while the coupling constants are the plasmonic equivalent to the nearest neighbor inter-site overlap integrals. This makes condensed matter effects simpler to investigate as it was already shown, e.g., for Bloch oscillations [31] and Anderson localization [32].

4.2.1 The Su-Schrieffer-Heeger model

In this thesis, we concentrate on the simulation of the Su-Schrieffer-Heeger (SSH) model with a plasmonic system. This is a model based on the work of W. P. Su, J. R. Schrieffer and A. J. Heeger on the soliton formation in polyacetylene and describes the evolution of electrons in an 1D chain of identical atoms [35, 36].

For the discussion of the model, it is convenient to define a unit cell and a labeling of the system. Based on the fact that the exact choice is arbitrary, we chose the unit cell as marked in Fig. 4.10, containing two identical atoms, labeled with A and B. Since the choice affects the pursuing calculations, as it will be shown at the end of this section, it is kept fixed for the following derivations.

Figure 4.10: Atomic chain of an infinite number of identical atoms named A and B with two different hopping amplitudes J and J'.
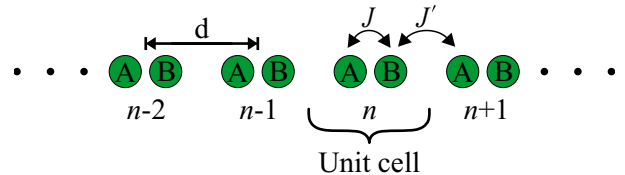
Based on the chosen unit cell, the distance between two so-called dimers can be described by d. With this as a basis, the electron hopping amplitudes describing the probability of an electron to change the lattice site can be divided into two groups, the inter-dimer hopping amplitude J'

and the intra-dimer hopping amplitude J. By neglecting the non nearest neighbor hopping, the Hamiltonian describing the system can be written as [91]:

$$\mathbf{H}_{\text{SSH}} = -\sum_n [J c_{\text{B,n}}^\dagger c_{\text{A,n}} + J' c_{\text{A,n+1}}^\dagger c_{\text{B,n}} + \text{H.c.}]\,, \tag{4.35}$$

with the annihilation operators for each lattice site, given by $c_{\text{A,n}}$ and $c_{\text{B,n}}$.

As the next sections will demonstrate, a system described by such Hamiltonian is a simple 1D example of a topological insulator, a material exhibiting a band gap in the bulk material and furthermore, under certain circumstances, states in the gap localized at the surface/edge of the system [37, 38].

Bulk states

In the bulk material, periodic boundary conditions can be applied. By using Bloch's theorem and performing a change of basis to a two particle system the corresponding momentum space Hamiltonian for each momentum k can be then derived to [91]:

$$\mathbf{H}_{\text{SSH,B}} = -\begin{pmatrix} 0 & \rho_k \\ \rho_k^* & 0 \end{pmatrix}, \tag{4.36}$$

with

$$\rho_k = J + J' e^{-ikd} =: |\rho_k|\, e^{-i\theta_k}, \tag{4.37}$$

and the newly defined internal phase factor θ_k.

If a unitary operator Γ (with $\Gamma^2 = \mathbb{I}$) can be found, such that the following condition holds true:

$$\Gamma^\dagger\, \mathbf{H}_{\text{SSH,B}}\, \Gamma = -\mathbf{H}_{\text{SSH,B}}\,, \tag{4.38}$$

the Hamiltonian exhibits chiral symmetry. Since this condition in the present model is fulfilled by the Pauli matrix σ_z [91], it serves as the chiral-symmetry operator of $\mathbf{H}_{\text{SSH,B}}$. This symmetry herein implicates that each eigenvalue of this Hamiltonian for each value of k has a counterpart of same absolute value but changed sign. As a result, the eigenvalue distribution is symmetric with respect to zero energy [92].

The eigenvalue problem itself, as it is given by $\mathbf{H}_{\text{SSH}}\, \psi_k = E_k \psi_k$, reduces for the momentum space Hamiltonian to one 2D eigenvalue problem for each value of the momentum k, described by:

$$-\begin{pmatrix} 0 & \rho_k \\ \rho_k^* & 0 \end{pmatrix}\begin{pmatrix} \alpha_k \\ \beta_k \end{pmatrix} = E_k \begin{pmatrix} \alpha_k \\ \beta_k \end{pmatrix}. \tag{4.39}$$

The eigenvalues (E_k) and eigenvectors ($\boldsymbol{u}_{\pm,k}$) of this problem, are then given by [91]:

$$E_k = \pm\sqrt{J^2 + J'^2 + 2JJ'\cos(kd)}\,, \tag{4.40}$$

and

$$\boldsymbol{u}_{\pm,k} = \frac{1}{\sqrt{2}}\begin{pmatrix} e^{-i\theta_k} \\ \pm 1 \end{pmatrix}. \tag{4.41}$$

These eigenvectors describe the eigenmodes of the complete system on an dimer basis, with each entry corresponding to an atom of type A and B, respectively. Obviously, the eigenmodes provide a clear dependence on the distribution of the hopping amplitudes. It is therefore convenient to discuss the most important cases $J' = J$, $J' > J$, and $J' < J$. The corresponding band schemes for the three cases are extracted from (4.40), while the internal phases of the eigenvectors are calculated for the top band by using (4.41) and an inter-dimer distance of d = 1.
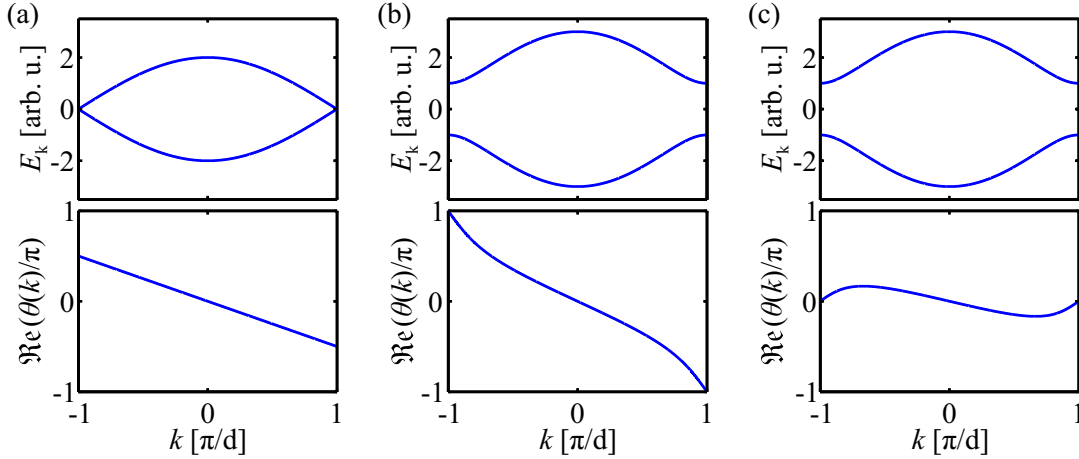
Figure 4.11: Energy eigenvalues and the corresponding internal phase distributions for the top band, as provided by the SSH model in case of a system with $J' = J = 1$ (a), $J' = 2 > 1 = J$ (b), and $J' = 1 < 2 = J$ (c).

(a) $J' = J$: The eigenvalues for the case $J = J' = 1$ are plotted in Fig. 4.11 (a). Clearly, the two bands of the system do not form a band gap. Hence, this system does not act as an insulator. The corresponding phase distribution is plotted in Fig. 4.11 (d). It shows a linear dependence on the momentum k. By moving along one band from $-\pi/d$ to π/d, a total phase of $\Delta\theta_k = \pi$ is accumulated.

(b) $J' > J$: The energy eigenvalues for a dimerized system with $J = 1$ and $J' = 2$ are plotted in Fig. 4.11 (b). Now, the system is described by two cosine-shaped bands separated by a band gap. Herein, the gap size at $k = \pm\pi/d$ equals $\Delta J = 2(J' - J)$, while maximal distance of both bands at $k = 0$ equals $2(J' + J)$. In addition, the phase distribution, plotted in Fig. 4.11 (e), has changed. The accumulated phase across the Brillouin zone in this case equals $\Delta\theta_k = 2\pi$.

(c) $J' < J$: If the value of the hopping amplitudes is exchanged, one might expect an identical behavior of the system with the changed dimerization. In fact, this is fostered by the equality of the energy eigenvalues of both bands, plotted in Fig. 4.11 (c) and (b). However, the phase distribution, depicted in Fig. 4.11 (f), differs drastically from Fig. 4.11 (e). Now, the accumulated phase by moving along one band in this case is given by $\Delta\theta_k = 0$.

Due to their insulating behavior and their difference in the accumulated phase, the latter two cases are the most interesting. Since the difference between both is induced solely by a change

of topology, both cases represent two so-called topological phases of the SSH topological insulator [91], manifested by the different accumulated phases. A general measure of this is the so-called Zak phase, based on the work of Zak [93] and Berry [94]. For the present system, it is given by [91]:

$$Z_{\text{zak}} = \frac{1}{2} \int \mathrm{d}k \frac{\mathrm{d}\theta_k}{\mathrm{d}k} = \frac{\Delta\theta_k}{2}. \tag{4.42}$$

Hence, for the described system, the Zak phases be calculated to $Z_{J'<J} = 0$ and $Z_{J'>J} = \pi$, respectively.

Note, that the absolute value of the Zak phase of each dimerization highly depends on the chosen unit cell [95]. The difference of the phase between two dimerizations is, however, an invariant, which can be used to describe the system [96].

Edge states

A particular interesting case appears, when two domains of a different topological phase are brought into proximity, e.g., if the system contains a finite number of atoms and both types of dimerization (the hopping amplitudes labeled such that always $J > J'$), as sketched in Fig. 4.12.
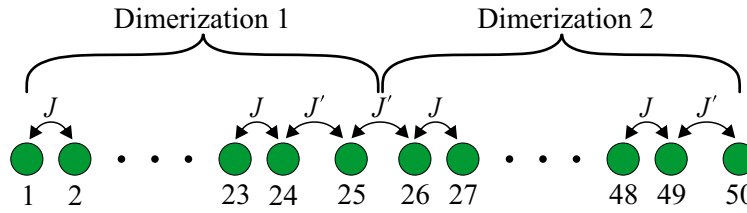
Figure 4.12: Dimerized chain of 50 atoms with two different hopping amplitudes J and J', providing in total two domains of different dimerizations and hence topological phases.

Now, there are two atoms (number 25 and number 50) being only weakly coupled to the nearest neighbors, as described by J'. Due to the chiral symmetry of the system, both atoms act as their own symmetry partners, leading to the occurrence of two localized states with zero energy [91, 92]. Such states are the so-called topological protected edge states, because of their position at an edge of the respective topological phase and the protection by topological arguments. Namely, they cannot disappear by continuous deformation of the system's parameters J and J', unless the gap is closed ($J = J'$) [37, 38].

This behavior can be verified, by considering a system of the proposed design with exemplary hopping amplitudes, given by $J' = 1$ and $J = 2$. Due to the finiteness of the system, Bloch's theorem cannot be applied any more, however, by using a single particle basis the Hamiltonian can be written as a matrix:

$$\mathbf{H}_{\text{SSH}} = \begin{pmatrix} 0 & J & & & \\ J & 0 & J' & & \large 0 \\ & J' & 0 & & \\ & & & \ddots & \\ \large 0 & & & & \end{pmatrix}. \tag{4.43}$$

Analog to the CMT, the eigenvalues and eigenvectors of this Hamiltonian can be calculated numerically for each arrangement of hopping amplitudes. Then, after sorting them in energetically ascending order the eigenvalues correspond to the energy E_n and the eigenvectors A_n to the amplitude distribution of the eigenmodes, with the mode number given by $n \in \{1...50\}$. The resulting eigenvalues are plotted in Fig. 4.13 (a).
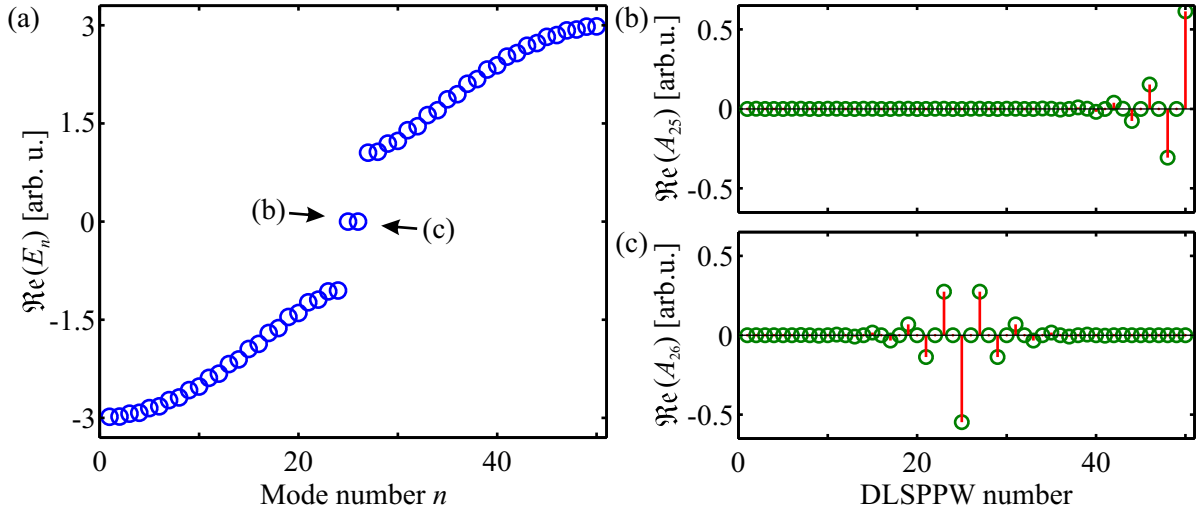

Figure 4.13: (a) Energy eigenvalues of the proposed system. (b) Eigenvector of the eigenstate number 25, indicated by an arrow in (a). (c) Eigenvector of the eigenstate number 26, indicated by an arrow in (a).

Similar to the discussed case of a dimerized chain of atoms of infinite length, the energy eigenvalues provide two bands and a band gap. Again, the maximal splitting of both bands is determined by the doubled sum over the hopping amplitudes, while the width of the band gap is defined by the difference $2(J' - J)$. From the amplitude distributions of the modes can be deduced that the bands are formed by the eigenvalues, corresponding to symmetric (top band) and asymmetric eigenmodes (lower band) of the system. However, in contrast to the discussed system of infinite length, two states are located in the gap at zero energy. In order to gain more information on these two states, their corresponding eigenvectors are plotted in Fig. 4.13 (b) and (c).

The eigenvectors describe the character of the corresponding states. Both exhibit a unique amplitude distribution. While the largest amplitude can be found in the central and rightmost DLSPPW, respectively, it is decaying away from them. Hence, as expected, both states are localized: one at the outer border of the system and the other one in the center of the system. Furthermore, the depicted amplitude distributions are zero on each other lattice site. This follows from the chiral symmetry of the system, since for a edge state with zero energy $\Gamma_s A = A$, with Γ_s being the chiral-symmetry operator of (4.43), has to apply [97].

These two states are hence examples of the expected topologically protected edge states. As experimentally demonstrated in similar systems, they are characterized by the presented localization [98] and offer a high robustness against perturbations [99, 100].

Temporal evolution

The temporal evolution of the finite system can be calculated, by making use of (4.43) and the Schrödinger equation. This leads to:

$$i\hbar \frac{\mathrm{d}}{\mathrm{d}t} \boldsymbol{\psi}(t) = \mathbf{H}_{\text{SSH}} \boldsymbol{\psi}(t). \tag{4.44}$$

In fact, the overall behavior of this system does not change if the on-site energy eigenvalues are simply shifted. Hence, the CMT can be used to mimic the SSH model by using (4.32) and an appropriate arrangement of coupling constants. Therefore, the temporal evolution will be discussed in the next section in the context of coupled DLSPPW arrays.

4.2.2 Implementation of the plasmonic SSH model

The design of the DLSPPWs, used for the realization of plasmonic SSH model, can be chosen based on the results of Sec. 4.1. There it was shown that DLSPPWs consisting of a dielectric structure ($n_{\mathrm{d}} = 1.49$) with a width of 250 nm and a height of 140 nm can be used to guide propagating SPPs. Furthermore, the coupling of such DLSPPWs can be tailored over a wide range by changing their center to center distances. For this reason, we restrict ourselves to this design for the following investigations.

The desired alternating coupling constants are achieved by using alternating center to center distances (d_{small} and d_{large}), as sketched in Fig. 4.14. In order to facilitate also the investigation of topologically protected edge states this design further includes two domains of different dimerization with a tunable transition area in between, determined by d_{gap}.
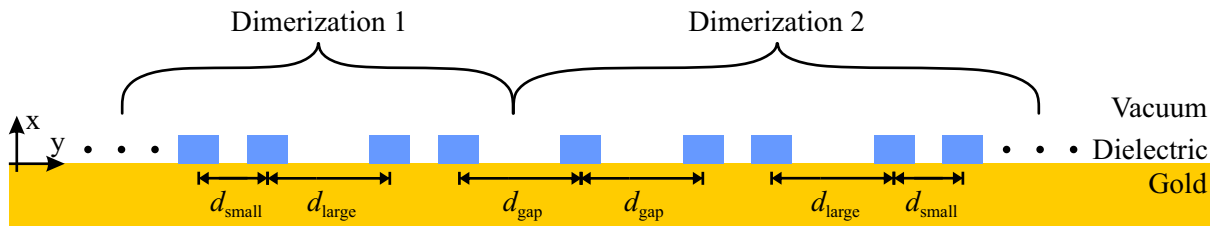

Figure 4.14: Design of a DLSPPW array utilized for the realization of the plasmonic SSH model. Two domains of different dimerization with alternating DLSPPW separations d_{small} and d_{large} are divided by a transition area, including one single waveguide with a center to center distance of d_{gap} to its neighbors.

To reduce the overall set of parameters this section concentrates only on center to center distances $d_{\text{small}} = 600$ nm and $d_{\text{large}} = 1000$ nm. Based on the results of the previous discussions this leads to an effective refractive index of $n_{\text{eff}} = 1.058 + \mathrm{i}0.0027$, as well as coupling constants of $C_{\text{small}} = 0.22 + \mathrm{i}0.004 \, \frac{1}{\mu\text{m}}$ and $C_{\text{large}} = 0.089 - \mathrm{i}0.0005 \, \frac{1}{\mu\text{m}}$. These parameters offer at the same time a large $\Delta C = (C_{\text{small}} - C_{\text{large}})$ and $W = 2(C_{\text{small}} + C_{\text{large}})$. Based on (4.40), this leads to a large band gap and a large band structure and hence to distinct features.

Bulk states in arrays with identical waveguide separations

We start with the investigation of the intensity evolution of propagating SPPs in a simple system of 48 DLSPPWs with identical center to center distances, given by $d_{small} = d_{large} = d_{gap} = 600\,nm$. This system represents the plasmonic equivalent to a crystal lattice consisting of equally spaced, identical atoms.

Corresponding to an electron located in the middle of the atomic chain at a time $t = 0$, propagating SPPs are excited in the middle of the array at z = 0 with a Gaussian shaped intensity distribution, obtaining a FWHM² of $w_{FWHM} = 350\,nm$. By using (4.21) and (4.22) we approximate the evolution of SPPs, propagating in this array in positive z-direction. The resulting intensity distribution is depicted in Fig. 4.15 (a).
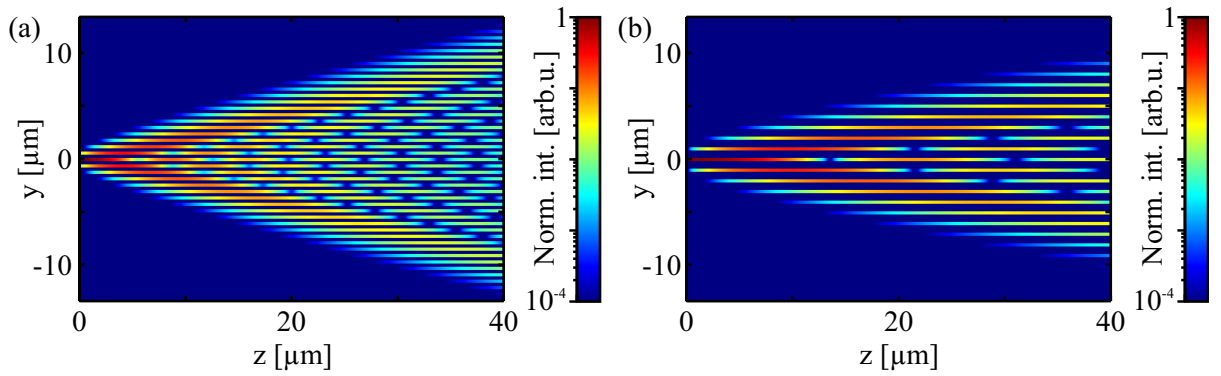
Figure 4.15: Intensity evolution of propagating SPPs in DLSPPW arrays with center to center distances of 600 nm (a) as well as 1000 nm (b).

While directly at the input (z = 0), the intensity is confined mostly to the central DLSPPW, the distribution gets broader with increasing distance, due to coupling to the adjacent DLSPPWs. It exhibits two main lobes of higher intensity at the sides and an enclosed interference pattern, being characteristic for the well-known discrete diffraction [28, 31, 101], the plasmonic analog to a quantum random walk [31].

In order to investigate the influence of increasing center to center distances in the DLSPPW array on this distribution, the same procedure is repeated for the larger $d_{small} = d_{large} = d_{gap} = 1000\,nm$. The resulting intensity distribution of SPPs, excited at z = 0 in the central DLSPPW and propagating in positive z-direction, is depicted in Fig. 4.15 (b).

This image exhibits the same characteristic intensity distribution of discrete diffraction, including two main lobes of higher intensity. However, the influence of the larger separations, which results in a decreased coupling, is obvious. The opening angle of the cone, formed by the two main lobes is drastically reduced resulting in narrower intensity distribution.

The broadening of both intensity distributions in propagation direction, can be explained by the excited eigenmodes of the systems. The systems exhibit extended eigenmodes, distributed over the whole array in y-direction. Due to the chosen excitation, many of these modes obtaining different propagation constants are excited simultaneously. The resulting dephasing then leads to the depicted interference phenomena.

---

² Full width at half maximum

The band structures, resulting from the excited eigenmodes in both cases, as imaged in Fig. 4.15, can be obtained by performing two-dimensional FFTs on the corresponding complex field distributions, as motivated by Sec. 4.1.3. The resulting Fourier space intensity distributions of both cases of discrete diffraction are depicted in Fig. 4.16.
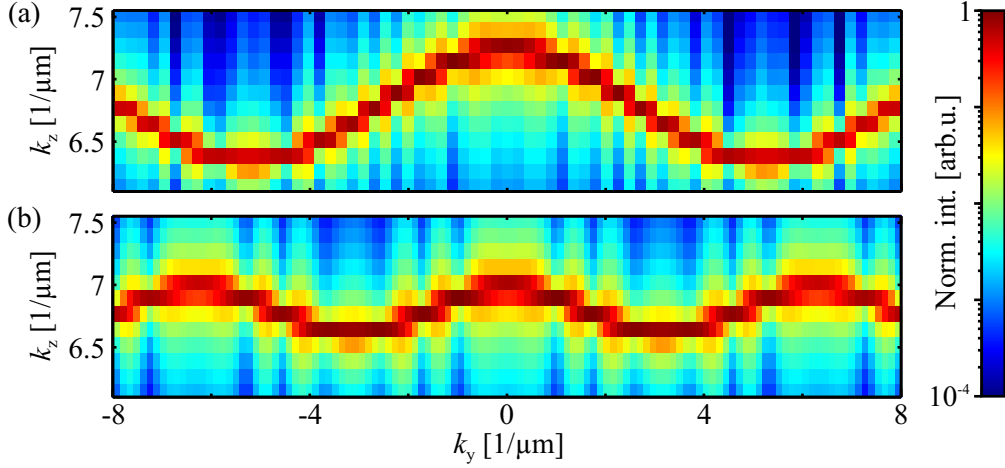

Figure 4.16: 2D FFT of the field evolution in equally spaced DLSPPW arrays with the center to center distances given by 600 nm (a) and 1000 nm (b), respectively. The corresponding real space intensity distributions are depicted in Fig. 4.15.

Both distributions exhibit one cosine-shaped band, which is the plasmonic analogue to the band structure depicted in Fig. 4.11 (a). A direct comparison of both plasmonic band structures reveals two features of considerable interest. The increase of the DLSPPW separations, accompanied by a decrease of the coupling constants, leads to deceased band widths and smaller periods of the cosine-shaped bands. Both is consistent with the behavior expected from the pure SSH model.

Bulk states in arrays with dimerized separations

Based on the theoretical considerations on the SSH model dimerized systems are of even more interest compared to the previously discussed non-dimerized systems. Therefore, as a next step, domains with a constant dimerization (d_{small} = 600 nm, d_{large} = 1000 nm) are investigated (see Fig. 4.14).

In order to avoid the excitation of edge states, we chose a sub-set of the array consisting of 48 DLSPPW located far away from each topological change (Dimerization 1). We use the CMT to approximate the intensity evolution of propagating SPPs, excited in the center of this sub-set with a Gaussian intensity distribution (w_{FWHM} = 350 nm). The resulting intensity distribution is depicted in Fig. 4.17 (a), on a logarithmic color scale.

Again, at z = 0 most intensity is confined in the central DLSPPW. In propagation (z-) direction, the distribution is broadening similar to the previously discussed cases. However, in the dimerized system the bright side lobes disappeared and the remaining intensity distribution is more diffuse and obtains an even narrower distribution, as imaged in Fig. 4.15. This is also confirmed by the line plot of the intensity distribution along the y-direction at z = 40 μm, which
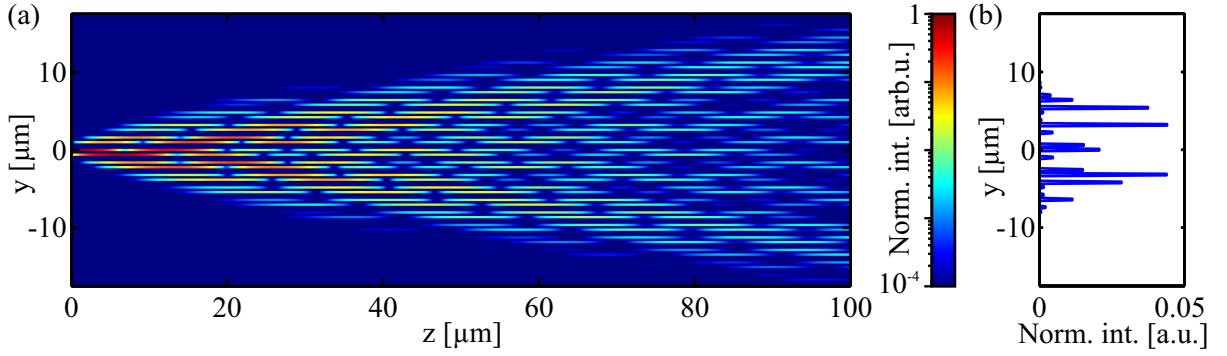
Figure 4.17: (a) Normalized intensity distribution of propagating SPPs in a DLSPPW array with alternating distances of d_{small} and d_{large}, originating from a Gaussian input in the central DLSPPW. (b) Line plot of the normalized intensity distribution in y-direction at z = 40 μm.

is depicted in Fig. 4.17 (b). The reason for this deviation is the dimerization of the coupling constants, which is accompanied by a small coupling between every second set of DLSPPWs.

Based on the considerations on the pure SSH model in the last section, this dimerization of the coupling constants should lead to the generation of two distinct bands in the band structure. This can be confirmed by performing a 2D FFT on the field distribution, corresponding to the intensity distribution imaged in Fig. 4.17 (a). The result is shown in Fig. 4.18.
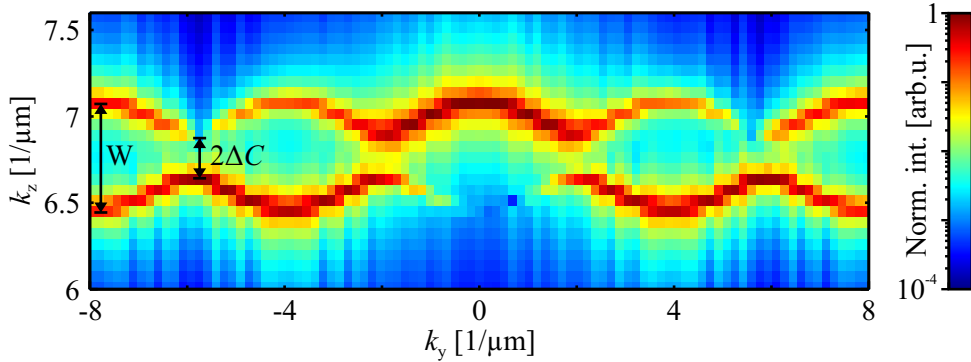
Figure 4.18: 2D FFT of the field distribution corresponding to the intensity distribution shown in Fig. 4.17 (a). Additionally marked are the band width W and the size of the band gap $2\Delta C$.

Indeed, this plot shows a two cosine-shaped bands, separated by a band gap, resembling the band structure, depicted in Fig. 4.11 (b). In accordance to this, the two bands in the plasmonic system provide a band gap and total widths as determined by $2\Delta C$ and W, respectively. In addition, the position of the complete structure relatively to $k_z = 0$, as related to a non-zero on-site energy, is determined by the effective refractive index of the DLSPPWs:

$$k_{mean} = \Re e(n_{eff}) \cdot k_0 \approx 6.8 \, \frac{1}{\mu m}. \tag{4.45}$$

Hence, this DLSPPW array represents the plasmonic realization of the bulk material, as described by the SSH model.

Edge states between two domains of different dimerization

The SSH model predicted that in the case of two adjacent domains with different topological properties, topologically protected edge states can occur (see Fig. 4.13). Since, the plasmonic realization of this case is depicted in the center of Fig. 4.14, for the proceeding investigations, we choose a subset of 49 DLSPPWs, arranged in a way that the isolated DLSPPW is in the center. This corresponds to the investigation of the temporal evolution of electrons in a system as it is described in Fig. 4.13.

The resulting intensity distribution of propagating SPPs, excited with a Gaussian intensity distribution ($w_{FWHM} = 350\,\mathrm{nm}$) in the central DLSPPW of an array with $d_{small} = 600\,\mathrm{nm}$ and $d_{gap} = d_{large} = 1000\,\mathrm{nm}$, is shown in Fig. 4.19 (a).
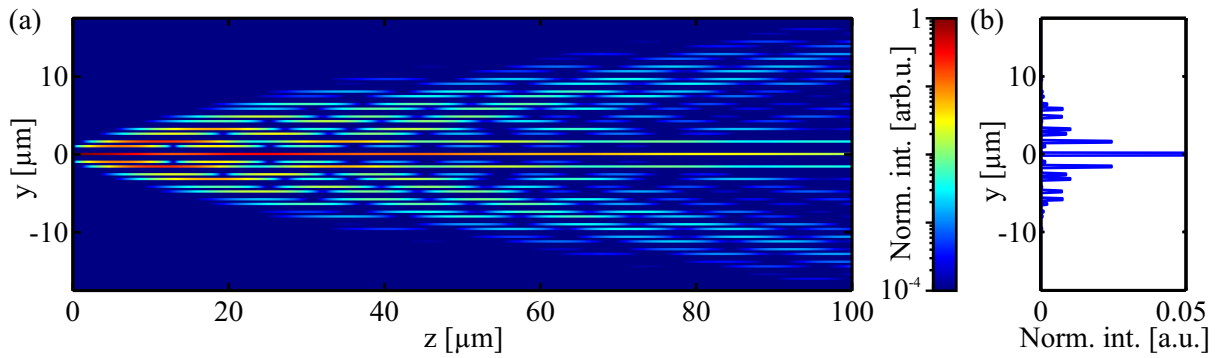
Figure 4.19: (a) Intensity distribution of propagating SPPs, excited in the central DLSPPW of an array containing two areas of dimerization. (b) Line plot of the normalized intensity distribution in y-direction at $z = 40\,\mu\mathrm{m}$.

The difference to the bulk case is evident. A large fraction of the intensity is confined in the central DLSPPW, leading to a sharp peak in the line plot of the intensity distribution in y-direction at $z = 40\,\mu\mathrm{m}$, shown in Fig. 4.19 (b). Based on the mode distribution of a topologically protected edge state, as depicted in Fig. 4.13 (b) and (c), this localized field evolution can be assigned to the excitation of a topologically protected edge state. Simultaneously, also bulk modes are excited, leading to a broadening of the intensity distribution in propagation direction, analogously to the previously discussed case.

More information can be deduced from this calculations after performing a 2D FFT of the field distribution. The resulting intensity distribution is shown in Fig. 4.20, on a logarithmic scale. In this field plot, two cosine shaped bands, as corresponding to the excited bulk modes, can be recognized again. In contrast to the previous case, however, an additional horizontal line in the middle of the band gap is apparent. This line corresponds to a mode confined to a single DLSPPW [102]. Together with the position in the middle of the gap (see Fig. 4.13 (a)), in fact, it can be assigned to the excited topologically protected edge state in the DLSPPW array, as already shown in Fig. 4.19.

Due to the confinement, the Fourier space position of this mode can be addressed by a manipulation of the optical properties of the central DLSPPW. A change of its effective refractive index for example leads to an upward or downward shift of this mode in the Fourier space.
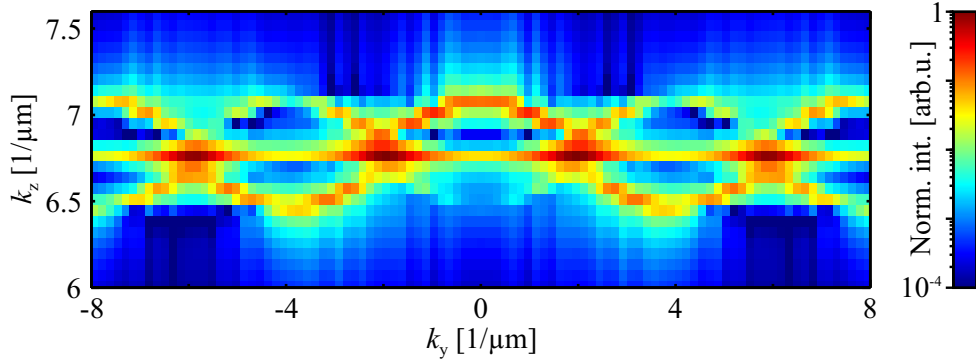
Figure 4.20: 2D FFT of the field distribution corresponding to the intensity distribution shown in Fig. 4.19 (a).

Because of a breaking of the chiral symmetry, the edge mode even can disappear, if the effective refractive index is changed in a way, that the mode is not lying in the band gap any more.

Note that, corresponding to the amplitude distribution of the edge mode, shown in Fig. 4.13 (c), the edge mode has a vanishing amplitude in every second waveguide. As a result, it can not be excited if the input is in the nearest neighbors of the central DLSPPW.

Edge states in a larger transition area

A particular interesting situation was not discussed so far: larger transition areas between two domains of a different topological phase. In a plasmonic system, this can be easily achieved for example by choosing $d_{gap} = d_{small} = 600\,nm$ and $d_{large} = 1000\,nm$. In this case, in the center of an array of 49 DLSPPWs, as shown in Fig. 4.14, a closely spaced group of five DLSPPWs appears. The resulting intensity distribution of propagating SPPs in such DLSPPW array, stemming from a Gaussian input ($w_{FWHM} = 350\,nm$) in the central waveguide, is shown in Fig. 4.21 (a).
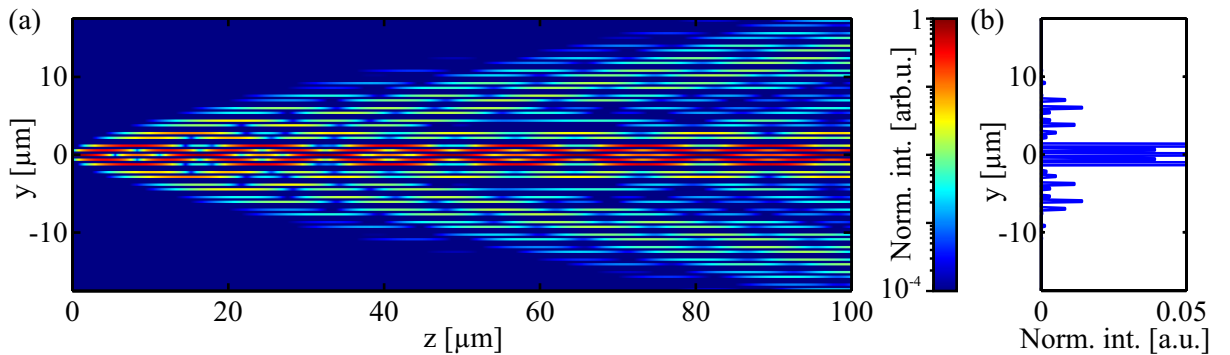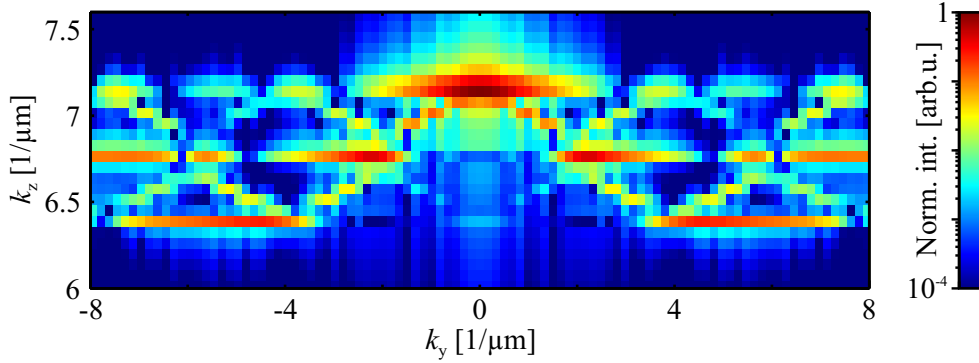

Figure 4.21: (a) Intensity distribution of propagating SPPs excited in the center of a larger transition area between two domains of different dimerization. (b) Line plot of the normalized intensity distribution in y-direction at z = 40 μm.

As in the two previously discussed cases, the intensity distribution exhibits a divergent behavior

in the propagation (z-) direction. However, in contrast to the case discussed last, a beating pattern around the central DLSPPW occurred. Consequently, in the data extracted from a line in y-direction at $z = 40\,\mu m$ and being shown in Fig. 4.21 (b), the intensity in the middle is confined to more than one DLSPPW. This behavior leads to the assumption that additional modes in the central region occurred. In order to confirm this we perform again a 2D FFT on the corresponding complex field distribution. The resulting intensity distribution is shown in Fig. 4.22, on a logarithmic color scale.

Figure 4.22: 2D FFT of the field distribution corresponding to the intensity distribution shown in Fig. 4.21 (a).

Here, in addition to the two cosine-shaped bands and the edge state in the middle two new states occurred localized above and below the bands. This behavior can be explained by treating the central five DLSPPWs in the middle as a third domain, obtaining a vanishing dimerization ($J' = J$). This domain supports bulk-type modes located within the area. In addition it exists one single topological protected edge state, due to the neighboring two areas of different topological properties. Consequently, a potential modification of the transition area in z-direction could lead to a dissolution of the bulk states, while the topologically protected edge state survives until the gap is closed ($J' = J$ in the outer areas). Also, the number of bulk-type modes increases with an increased size of this transition area, while always only one topologically protected edge state exists. If the extension of the new equally spaced area becomes larger then the field distribution, the resulting field evolution corresponds to pure discrete diffraction, again. In this case, the topologically protected edge state, however, still exists, but is not excited any more due to the missing field overlap.

4.2.3 Comsol Multiphysics based eigenmode expansion

In the last sections the evolution of the SPP intensity in the DLSPPW arrays was modeled by the CMT. Herein, we have chosen the CMT to model the SPP intensity in the DLSPPW arrays because of its mathematical equivalence with the discrete Schrödinger equation that governs the evolution of states in the SSH model. Since deviations between the CMT and the Comsol Multiphysics calculations already appeared in the two DLSPPW system, the same can be expected for larger DLSPPW arrays.
In order to investigate the deviations in case of such arrays we apply the Comsol Multiphysics

based eigenmode expansion, described in Subsec. 4.1.6. For this purpose, modal analyses of DLSPPW arrays with the same designs as presented in the last sections are performed. For all 48 DLSPPWs (49 in the systems with a additional single DLSPPW in the center), one eigenmode is provided by the software with both, field distribution and effective refractive index.

As described more detailed in Subsec. 4.1.6, the CMT-like eigenvectors of each system are derived from the field distributions of each mode, by taking one field value per waveguide, while the eigenvalues are directly provided by Comsol Multiphysics. From these values, an eigenvectors and the corresponding eigenvalue matrix is assembled. Then, by using (4.33), the system matrix $\mathbf{A}_{\mathrm{COM}}$ is calculated. Since, this matrix is of the same form as (4.32), the coupling constants and refractive indices are extracted. Additionally the field evolution in the corresponding DLSPPW array is calculated.

System matrix comparison

We start with a comparison of the system matrices assumed for the CMT ($\mathbf{A}_{\mathrm{CMT}}$) and the one originating from the Comsol Multiphysics based eigenmode expansion ($\mathbf{A}_{\mathrm{COM}}$), for the system discussed in the context of edge states between two domains of a different dimerization. As a first step, the distribution of the coupling constants are extracted from the non-diagonal entries of both matrices. The results are depicted in Fig. 4.23 on a logarithmic color scale.
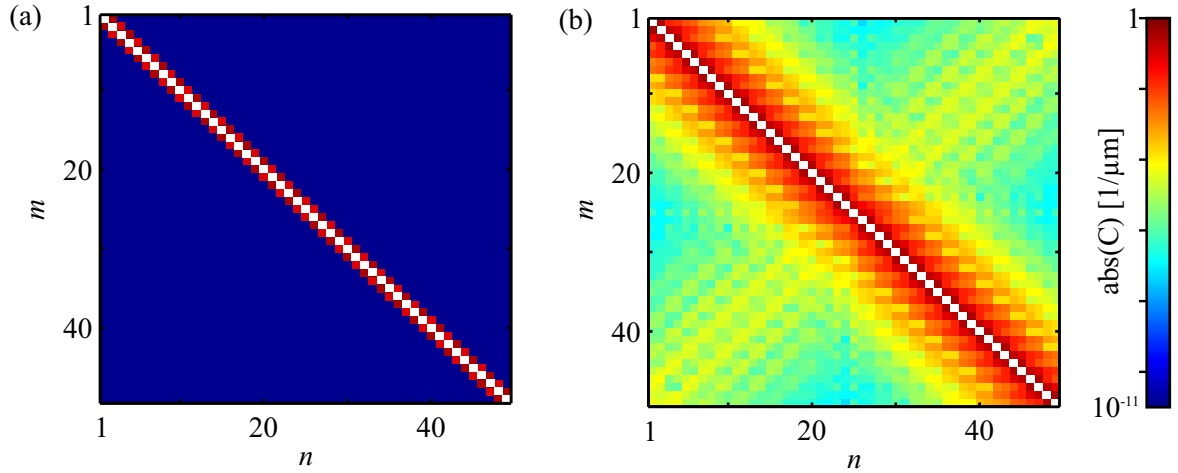

Figure 4.23: (a) Distribution of coupling constants deduced from the CMT ($\mathbf{A}_{\mathrm{CMT}}$) calculations. (b) Distribution of coupling constants as described by the system matrix $\mathbf{A}_{\mathrm{COM}}$.

The plots describe the coupling between the m-th and n-th DLSPPW of the array, the diagonal is masked. Consequently, in Fig. 4.23 (a), corresponding to the next neighbor CMT, only the secondary diagonals contain non-zero values. In fact, the alternating coupling due to the dimerization can be observed, including the edge in the center.

In contrast to that the distribution of the coupling constants, calculated from the Comsol Multiphysics based eigenmode expansion, depicted in Fig. 4.23 (b), deviates. Clearly, it exhibits more than only next neighbor coupling and is even influenced by the transition area in the middle of the array. The direct comparison of the values of both cases reveals that the nearest neighbor

coupling extracted from Fig. 4.23 (b), is 30 % larger than the one expected from the pure CMT.

As a second step, the effective refractive index distribution in the DLSPPW array is extracted from the masked main diagonal of both system matrices. While in the matrix assumed for the CMT all effective refractive indices are equal, the indices calculated from the Comsol Multiphysics simulations are smaller and strongly influenced by each edge of the system.

Similar to the discussed two DLSPPW system, all these deviations depend strongly on the DLSPPW spacings. However, as additional simulations confirmed, the deviation of coupling constants and effective refractive index distributions have to be considered in all arrangements of separations used in this thesis. Furthermore, such a non-vanishing non next neighbor coupling breaks the chiral symmetry of the system [103]. Therefore, the existence of a topologically protected edge state is not guaranteed. In order to gain more information on this, the next section will discuss the influence of the field evolution within the simulated DLSPPW array.

Field evolution

As discussed in Subsec. 4.1.6, from the system matrix $\mathbf{A}_{\text{COM}}$ the field evolution of propagating SPPs in a DLSPPW array can be calculated. However, with the coupling constant distribution and effective refractive index values, extracted from the Comsol Multiphysics simulations. As an example, it is performed for the design and the excitation scheme, discussed in the context of edge states between two domains of different topological phase. The resulting intensity distribution is shown in Fig. 4.24 (a) on a logarithmic color scale.
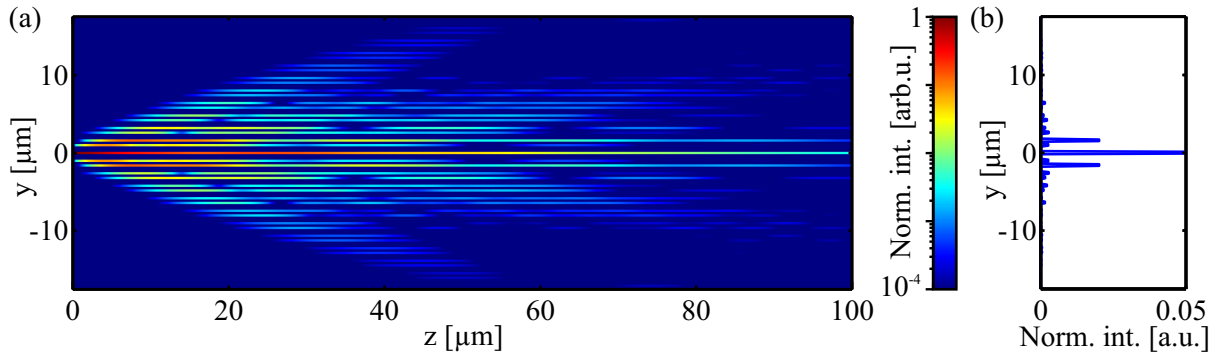

Figure 4.24: (a) Intensity evolution of SPPs in a DLSPPW array, as calculated with the Comsol Multiphysics based eigenmode expansion. (b) Line plot of the normalized intensity distribution in y-direction at z = 40 μm.

In contrast to Fig. 4.19, the calculated intensity distribution exhibits two additional side lobes with a large opening angle. As additional calculations obtained, they are mainly generated by the non next neighbor coupling constants, neglected in the CMT calculations, and depend highly on the excitation scheme. Nevertheless, still a large fraction of the intensity is confined in the central DLSPPW. This behavior is also confirmed by the plot of the intensity at z = 40 μm, shown in Fig. 4.24 (b). It exhibits a similar distribution as the topologically protected edge state, depicted in Fig. 4.19.

However, before the excitation of a topologically protected edge state can be declared, a 2D FFT has to be performed. It will give even more insight into the band structure of the excited

eigenmodes of the system and the properties of the potential edge state. The resulting intensity distribution is plotted in Fig. 4.25.
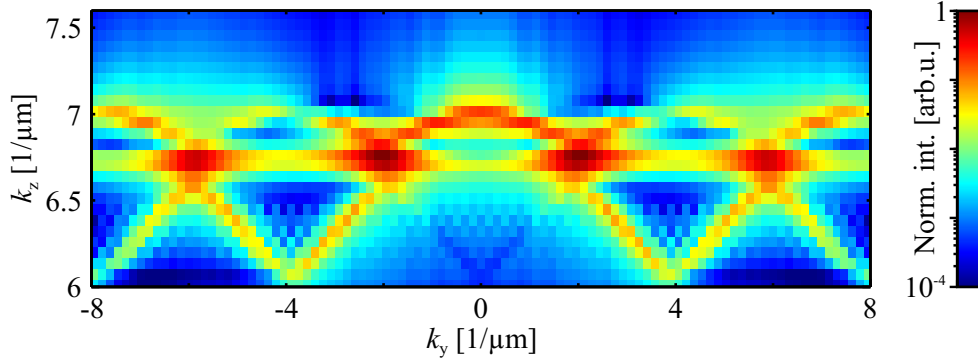

Figure 4.25: 2D FFT of the field distribution, corresponding to the intensity distribution imaged in Fig. 4.24 (a).

The Fourier intensity distribution still exhibits two bands and a horizontal line of high intensity in between. However, several deviations to the already discussed results as obtained from the CMT, can be recognized. The top band has a smaller band width than the lower band and the gap state is not exactly located in the middle of the gap. Both contrasts to Fig. 4.20. Additionally a regular pattern can be recognized in the lower band. It stems from the fact that the newly occurred side lobes, shown in Fig. 4.24 (a), are reflected from the edges of the array.

The reason for both mentioned deviations from the pure SSH model and the CMT, is the present non nearest neighbor coupling. It acts as a small symmetry breaking perturbation [103]. This perturbation is, however, not sufficient to shift the state out of the band gap. Therefore, by neglecting the non next neighbor coupling this state is to first order approximation still a topologically protected edge state.

Distance dependence

In order to investigate the different widths of the two bands as a function of the chosen DLSPPW distances, several simulations for $d_{small} = 600$ nm as well as $d_{small} = 800$ nm, combined with a d_{large} from 1000 nm up to 1600 nm are performed. The assumed design herein corresponds to systems with the same topological phase (i.e. choice of the dimerization), as previously discussed in in the context of bulk states in arrays with dimerized separations. From the resulting eigenvalues, the band gap g as well as the widths of both bands are extracted (A_{bottom} and A_{top}). The asymmetry of the bands is calculated by A_{bottom}/A_{top}. The results are plotted in Fig. 4.26 (a) and (b), together with the gap sizes, extracted from the corresponding CMT calculations.

The asymmetry of both bands, as indicated by the circles in Fig. 4.26 (a), increases with decreasing d_{small} and increasing d_{large}. In detail, the reduction of the asymmetry for larger d_{small} stems from the transition to a weaker coupled system. The increase of the asymmetry for lager d_{large}, however, indicates on a stronger influence of the non next neighbor coupling in systems with a significant dimerization of the DLSPPWs.

At the same time, the gap sizes obtained by the CMT calculations (solid lines in Fig. 4.26 (b)) increase as expected with an increasing difference of the coupling constants. The results from
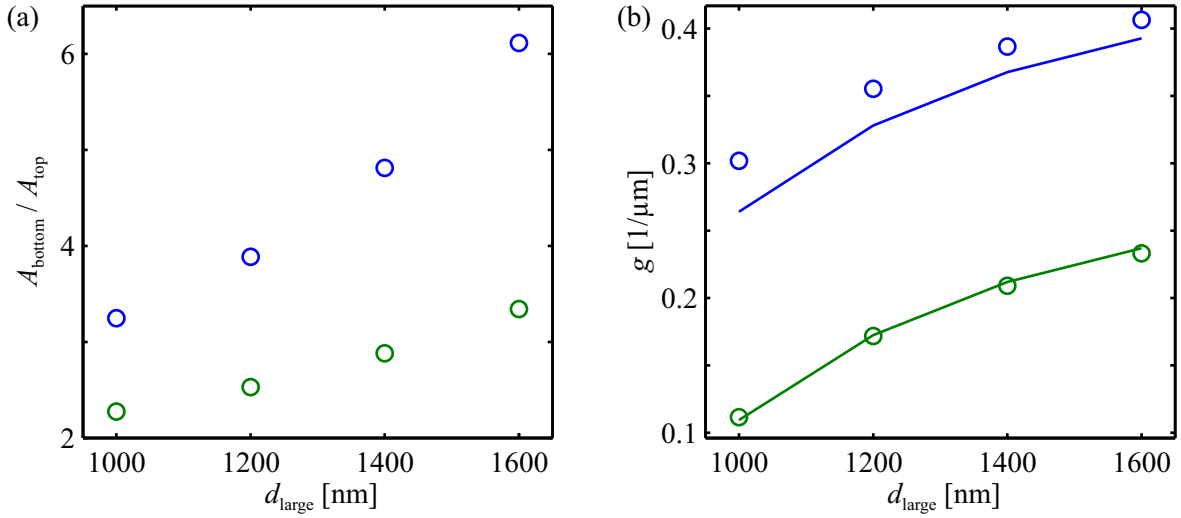
Figure 4.26: (a) Asymmetry of the bands in dependence on d_{large} for $d_{small} = 600\,$nm (blue) and $d_{small} = 800\,$nm (green), respectively. (b) Band gaps as a function of d_{large} for fixed $d_{small} = 600\,$nm (blue) and $d_{small} = 800\,$nm (green), respectively. The solid lines represent the results expected from the CMT, while the circles represent the results from the Comsol Multiphysics based eigenmode expansion.

the Comsol Multiphysics based calculations, however, offer a d_{small}-dependent deviation. As discussed in context of the system matrix comparison this can, however, be explained by the previously neglected non next neighbor coupling.

4.3 Fabricated samples

All DLSPPW arrays, discussed in this section, are fabricated on top of a gold chromium coated cover slide, by making use of the fabrication method presented in Sec. 3.4. In account for the new type of experiment, two parameters are changed. On the one hand the thickness of the PMMA coating is increased by reducing the rotation velocity in the second part of the spin-coating procedure to 1500 rpm. This facilitates the fabrication of structures with a thickness exceeding 200 nm. In addition, the thickness of the chromium layer is increased to 10 nm in oder to suppress unwanted SPP excitations at the gold glass interface by the large absorption of chromium.

The plasmonic implementation of the SSH model is realized by fabricating DLSPPW arrays with alternating DLSPPW separations. While the exact values of the two separations differ from array to array, the DLSPPWs themselves are designed as rectangles with 350 nm width, 180 µm length and a dose of 140% (relative to the nominal dose, given in Sec. 3.4). As additional parameter, the dose of the central DLSPPW is varied between 133% and 161%, facilitating the manipulation of its behavior and a compensation of the proximity effect (see Sec. 3.4 (c) for more details).

In order to cover a broad range of coupling constants, two sets of structures are fabricated on one sample. Following the results from the previous sections, based on the design imaged in Fig. 4.14, one set is with a d_{small} = 600 nm and the other one with d_{small} = 800 nm. In both sets, d_{large} = d_{gap} is varied between 1000 nm and 1600 nm. In addition arrays with d_{large} = d_{gap} = d_{small} are fabricated, covering the same range. Furthermore, in order to investigate a smoother transition area, arrays with a smaller d_{gap} = 600 nm are fabricated.

An SEM micrograph of a typical DLSPPW array with a center to center distance of d_{small} = d_{large} = d_{gap} = 600 nm, is shown in Fig. 4.27.
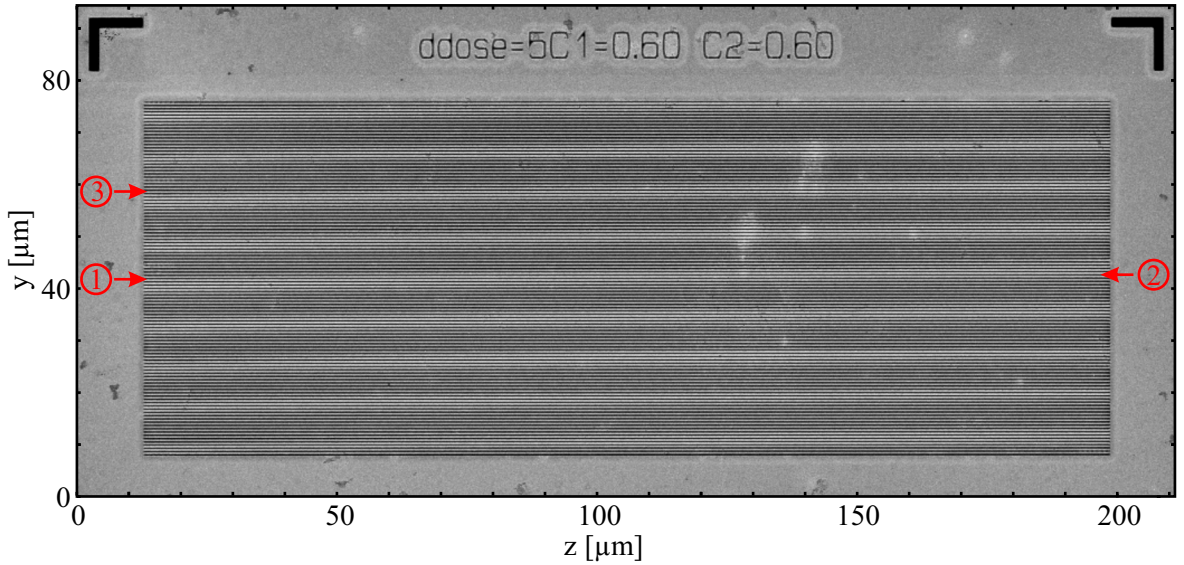
Figure 4.27: SEM image of a DLSPPW array with d_{large} = d_{small} = d_{gap} = 600 nm. The arrows indicate the position of three grating couplers, fabricated on top of DLSPPWs.

The right-angled structures on the top left and top right are markers, indicating the edges of the write field with a size of 200 μm × 200 μm. With their known edge length of 10 μm, they can be used for the distance calibration of the optical setup. The actual DLSPPW array can be recognized as dark, horizontal lines in the central area of the image. The red arrows indicate on the position of three grating couplers that are fabricated on top of different waveguides in order to facilitate different excitation schemes. They consist of small rectangles with a period of p = 890 nm, written with a dose of 40% on top of the DLSPPWs.

Each of the arrays contains two domains with different topological phases and a transition area in between, as it can be seen in the zoomed SEM image of a DLSPPW array with d_{small} = 600 nm and d_{large} = d_{gap} = 1000 nm, depicted in Fig. 4.28.

The DLSPPWs with separations given by d_{gap}, d_{large}, and d_{small}, can be clearly distinguished. The positions of the three grating couplers (the arrows point on their relative position) are chosen in such a way that one is on top of the central DLSPPW (1), a second one on top of the right end of the neighboring DLSPPW (2), and the last one in the bulk material of the upper domain (3).
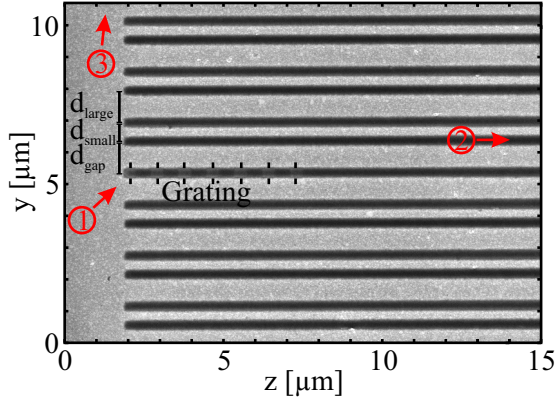
Figure 4.28: SEM image of a DLSPPW array with $d_{small} = 600$ nm and $d_{large} = d_{gap} = 1000$ nm, and a grating with period $p = 890$ nm on top of the central DLSPPW (1). The red numbers and arrows point in direction of the additional grating couplers (for the exact positions see Fig. 4.27).

Width of the DLSPPW

The width of isolated DLSPPWs from two arrays with different DLSPPW separations is measured with the SEM. The first array provides separations, given by $d_{small} = d_{large} = 600$ nm. A magnified SEM micrograph is depicted in Fig. 4.29 (a). This fabricated DLSPPW does not have a perfectly rectangular shape, however, a thin core structure of approximately 190 nm width, surrounded by a region of decreasing thickness (shadowed region) with a width of approximately 320 nm.

The second investigated DLSPPW is contained in an array with larger separations, as given by $d_{small} = 600$ nm and $d_{large} = 1600$ nm. In this case both widths (core structure and shadowed region) decreased to approximately 290 nm and 160 nm, respectively.

While the obtained width indications are rather coarse due to the profile of the fabricated DLSPPWs, the broadening influence of the proximity effect is still obvious and has hence to be considered in the discussion of the experimental results.
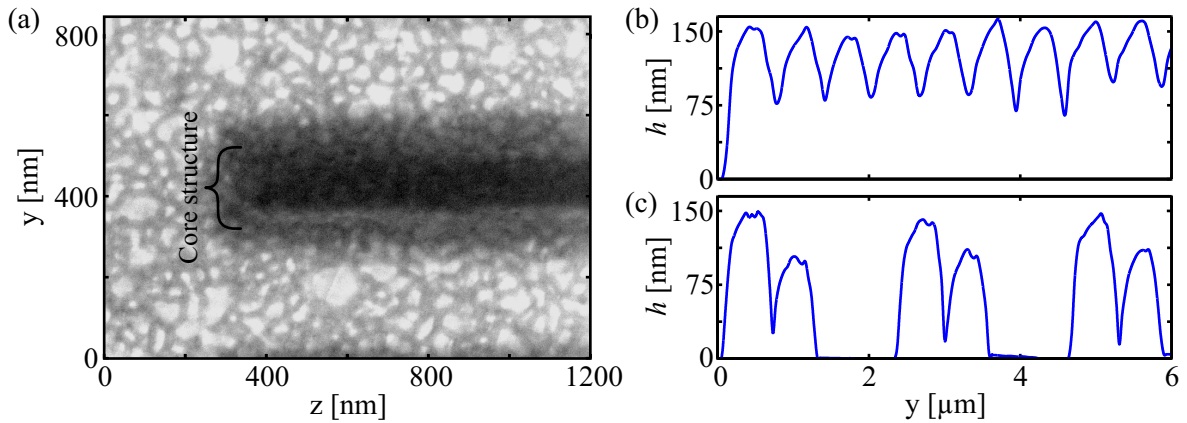

Figure 4.29: (a) Magnified SEM image of a DLSPPW contained in an array with $d_{small} = d_{large} = 600$ nm. In addition, the AFM measured heights of the same array as well as a second one with $d_{large} = 600$ nm and $d_{large} = 1600$ nm are depicted in (b) and (c), respectively.

Height of the DLSPPW

In order to investigate the profile of the fabricated structures, the height distribution of the DLSPPW arrays are measured with an AFM, operated by Tim Flatten[3]. The resulting profiles of two DLSPPW arrays of the same dose profile, both with d_{small} = 600 nm, however, with a differing d_{large} = 600 nm and d_{large} = 1600 nm, are imaged in Fig. 4.28 (b) and (c).
Obviously, the height of the structures depends on the distance to the nearest neighbor. While for $d_{small} = d_{large}$ = 600 nm, the height of the DLSPPWs is approximately 150 nm, it drops to an average height of approximately 125 nm for d_{large} = 1600 nm. Additionally, the height of the DLSPPWs within one unit cell can differ. Both effects demonstrate again the influence of the proximity effect and the type of path, traced by the electron beam.

Note that we can not use the AFM data to accurately determine the width of the DLSPPWs. The reason for that is the finite size of the AFM tip which leads to the measurement of a convolution of the tip and the structured surface [104].

4.4 Optical setup

The experimental setup, used for the investigation of propagating SPPs in the DLSPPW arrays, is based on the one discussed in the context of the manipulation of propagating Airy SPP beams (see Fig. 3.9). However, in order to image not only the intensity distribution on top of the gold film, but also the corresponding angular distribution of the emitted leakage radiation of the new samples, this setup is extended by making use of Fourier space imaging.

4.4.1 Fourier space imaging

The working principle of the Fourier space imaging in the context of leakage radiation microscopy is sketched in Fig. 4.30 for different bundles of rays, leaving the sample.
While the red bundle of rays corresponds to the directly transmitted laser beam, the gray bundles of rays correspond to leakage radiation, leaving the sample at a given position with an angle, depending on n_{eff}. To simulate the path of the bundles of rays in the inner of the objective, it is modeled as one simple lens.
In the back focal plane of the objective (BFP) all bundles of rays, leaving the sample under the same angle, are imaged onto the same position. It is relatively to the optical axis denoted by d and depends on the emission angle Θ of the radiation. In case of a high-NA objective, this dependency can be modeled as [105]:

$$d = f_{obj} n_{Oil} \sin \Theta, \tag{4.46}$$

with f_{obj} being the focal distance of the objective and n_{Oil} the refractive index of the utilized immersion oil.
Subsequently, all bundles of rays leave the objective, obtaining an angle to the optical axis, depending on the originating position on the sample. Note that for large distances between

---

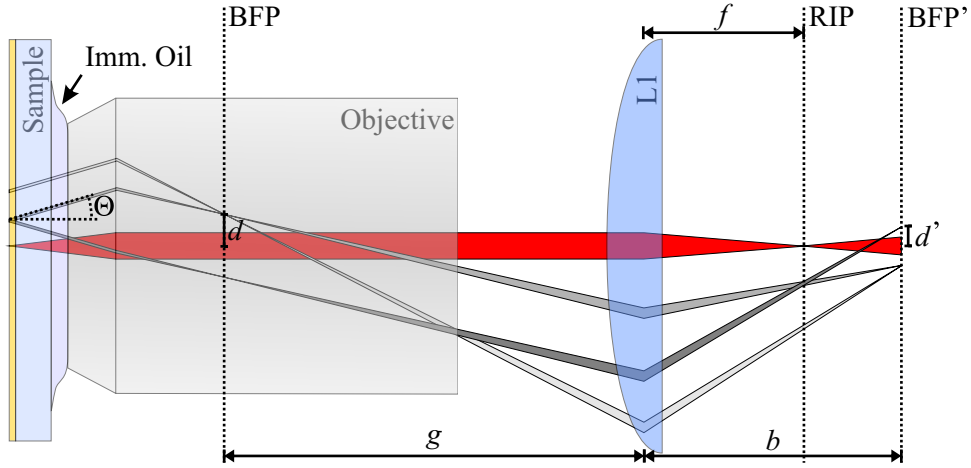[3] Group of PD Dr. Elisabeth Soergel, Physikalisches Institut, Universiät Bonn

Figure 4.30: Principle of Fourier space imaging of propagating SPPs with an objective and one additional tube lens. As examples the paths of several bundles of rays are depicted, as they pass a system modeled with two simple lenses. As image planes, the back focal plane (BFP) of the objective, as well as the real image plane (RIP) and back focal plane (BFP') behind the lens (L1) are marked.

objective and tube lens (a large so-called infinity space), only a fraction of the emitted radiation is collected by a lens of finite diameter, resulting in potential imaging artifacts.

The tube lens generates two images. On the one hand, a real image of the sample's surface is generated in the focal plane of the tube lens, in Fig. 4.30 labeled as real image plane (RIP). On the other hand an image of the BFP is generated (labeled as BFP'). The distance to the tube lens herein can be calculated via the imaging equation.

The resulting form of the angular spectrum in BFP' depends on both, the used tube lens and the objective. In combination with (4.46), the influence of all these components can be assembled in the proportionality factor D. The corresponding dependence of d' (see Fig. 4.30) and Θ, can be written as:

$$d' = D \sin \Theta. \qquad (4.47)$$

In comparison with (2.21) it follows that:

$$d' = D \cdot \frac{\beta}{k_{\text{glass}}} = D \cdot \frac{n_{\text{eff}}}{n_{\text{glass}}}. \qquad (4.48)$$

Hence, in BFP' the distance from the optical axis is directly proportional to the effective refractive index of the propagating SPPs. By considering the rotational symmetry of the used optical components, this derivation can now be easily extended to two dimensions. Then, the resulting intensity distribution corresponds to the Fourier transform of the complex SPP field distribution on the sample's surface [106]. For this reason this type of imaging is called Fourier space imaging.

For the calibration of BFP', the numerical aperture (NA) of the objective can be used. From its definition follows that the highest accepted angle of the objective corresponds to the highest

occurring distance from the optical axis in BFP' [69]. This dependency can be written as:

$$d'_{\text{max}} = D \cdot \frac{\text{NA}}{n_{\text{glass}}}. \tag{4.49}$$

Note, that RIP and BFP' can also be used as intermediate image planes in a more elaborate setup. Then, by using a simple knife edge, the different spatial or angular components can be selectively blocked. For example, this allows for the blocking of the directly transmitted laser beam in BFP' [107].

4.4.2 Imaging system

The first part of the used optical setup is similar to the one used for the Airy SPP beam experiments (compare Fig. 3.9). However, the laser source is exchanged by a diode laser of 980 nm wavelength, as this results in an increased propagation length of the SPPs, due to the decreased damping in the gold layer [57]. Furthermore, to facilitate the Fourier space imaging, the imaging part of the setup is extended. The exchanged components are sketched in Fig. 4.31.
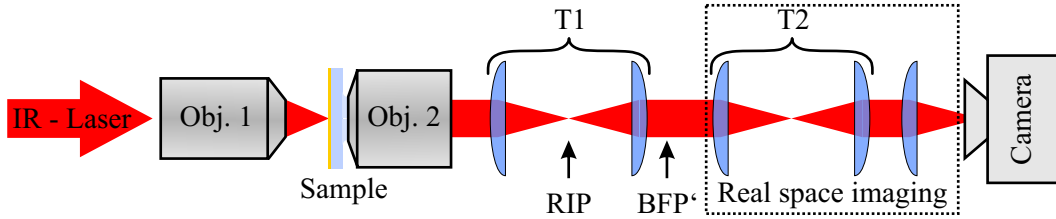

Figure 4.31: Basic optical system utilized to perform leakage radiation microscopy on propagating SPPs in DLSPPW arrays. Beside two telescopes (T1 and T2) also the intermediate real image plane (RIP) and back focal plane (BFP') are marked.

The TM polarized laser beam is focused onto the sample with Objective 1,[4] obtaining a larger magnification as the previously used one. It hence leads to a smaller spot and higher intensity on the sample's surface, compared to the previous experiments.
All light emitted by the sample is collected by objective 2,[5] and subsequently passes the first telescope (T1). This telescope provides a magnification of $M = 1$ and has a distance to Objective 2, being smaller than the focal length of its first lens. As a result, it generates a RIP in its center, as well as an image of the back focal plane (BFP') behind the telescope, that corresponds to a Fourier space image plane. In the present setup, both image planes act as intermediate image planes, which can be used for angular and spatial filtering with knife edges, as it was explained in the previous section.
The remaining optical components are mounted on removable posts, in oder to facilitate the imaging of both image planes onto the camera, without moving it. The dotted rectangle in Fig. 4.31 depicts the combination of lenses, used for the real space imaging. It contains a second telescope (T2) of magnification $M = 1$, which is used to reduce the size of the infinity space.

---

[4] M Plan Apo NIR 20x, Mitutoyo Europe GmbH, Germany
[5] Apo TIRF 100x, Nikon GmbH, Germany

66

The actual imaging is then performed by focusing the light with a single lens onto the camera.[6] Alternatively, the optical components in the dotted rectangle can be exchanged by one single lens, used for the Fourier space imaging. The position of the camera is kept fixed during this procedure.

4.5 Experimental results

In the next step, the fabricated samples are investigated by utilizing the described optical setup to perform real and Fourier space imaging of propagating SPPs on the gold surface.

4.5.1 Discrete diffraction in equally spaced DLSPPWs

We start with the simplest case, the investigation of the field evolution of propagating SPPs in two DLSPPW arrays with equally spaced, identical DLSPPWs. In both cases, the sample is placed in the optical setup in such a way that the laser is focused onto one of the grating couplers on the array. By using the knife edge placed in BFP', the left propagating SPPs as well as the directly transmitted laser beam, are filtered out.

Real space images

As a first step, the resulting real space intensity distribution in a DLSPPW array with $d_{\text{small}} = d_{\text{large}} = d_{\text{gap}} = 600$ nm, is imaged on the camera. The known length of the markers is used to calibrate the length scale, leading to an uncertainty of the axes's values of approximately 2%. Based on this, the coordinate system is defined in a way that the origin coincides with the position of the grating coupler and the SPPs propagate in positive z-direction. The resulting normalized intensity distribution in the array is shown in Fig. 4.32 (a), on a logarithmic color scale.

Consistent with the theoretical considerations, directly at the input (z = 0), most of the intensity is confined in the central DLSPPW. Due to coupling to the neighboring DLSPPWs, the intensity distribution broadens in y-direction with increasing propagation distance. It exhibits two outer lobes of high intensity and a regular intensity pattern in between. Based on the theoretical considerations, this corresponds to the well-known discrete diffraction [28, 31, 101].

In order to compare the experimental image to the theoretical calculation based on the CMT in detail, the theoretically determined course of the main lobes is extracted from Fig. 4.15 (a) and included in Fig. 4.32 (a) as dotted black lines. Several deviations of the experimental intensity distribution can be observed. Firstly, the opening angle of the outer lobes in the experimental image is larger. This is mainly related to an increased coupling as it was predicted by the Comsol Multiphysics based eigenmode expansions. Secondly, the abrupt ending of the intensity distribution in the top part of the experimental image (indicated by the red arrow), as it simply originates from the end of the fabricated DLSPPW array, leading to a reflection of propagating SPPs. Finally, the discrete type of the patterning is blurred out in the experimental image. This stems from the fact, that here the intensity distribution of the total field on the surface is imaged,

---

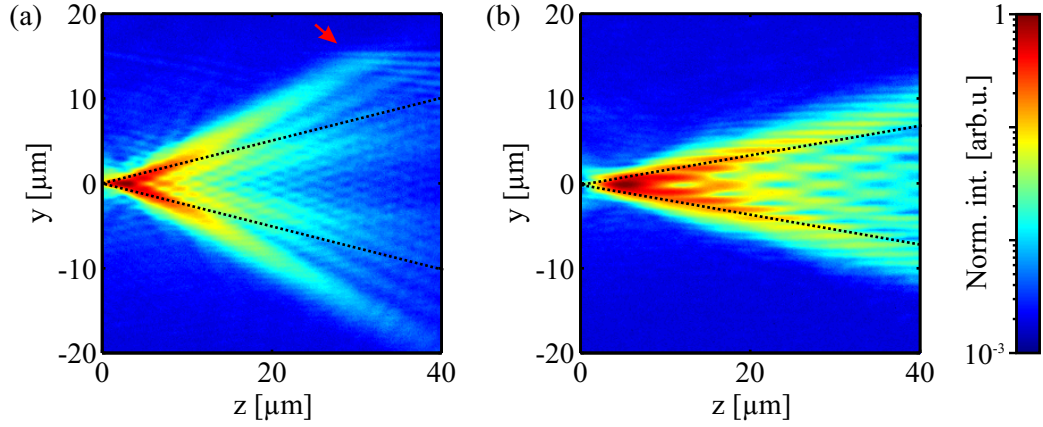[6] Zyla sCMOS, Andor Technology Ltd., United Kingdom

Figure 4.32: Discrete diffraction of propagating SPPs in DLSPPW arrays with center to center distances of 600 nm (a), as well as 1000 nm (b). The dotted black lines indicate the form of the calculated intensity distributions, as extracted from Fig. 4.15. The red arrow in (a) marks the edge of the DLSPPW array.

in contrast to the discrete amplitude distribution of the single DLSPPWs, which is displayed in Fig. 4.15 (a).

Based on the theoretical considerations it is further expected that increasing the center to center distances, leads to a reduced coupling and hence a narrowing of the main lobes' opening angle. In order to test this dependency, the same measurement is repeated on a DLSPPW array with the increased separations given by $d_{small} = d_{large} = d_{gap} = 1000$ nm. The resulting intensity distribution is shown in Fig. 4.32 (b), together with the course of the theoretically expected main lobes, extracted from Fig. 4.15 (b).

In comparison to the smaller DLSPPW separations, in the present case the opening angle between both main lobes, generated by the propagating SPPs, decreased. Furthermore, originating from the larger separations, the intensity distribution is less blurred and resembles again the one expected for discrete diffraction [28, 31, 101]. The fact that the opening angle of the main lobes in the experimental image deviates less from the theoretically expected courses, demonstrates the higher accuracy of the CMT at larger DLSPPW separations, due to the smaller coupling constants.

Fourier space images

The following procedure is performed for both systems to investigate the band structure of the excited eigenmodes in the DLSPPW arrays. Without moving the sample, the real space imaging arm of the optical setup is replaced by the single lens, used for the Fourier space imaging. Subsequently, the Fourier space is calibrated, by manually fitting a circle to the circular border of the objective's back focal plane. The radius of this structure corresponds to the numerical aperture of the objective [34]. Therefore, it can be used together with the center of the circle to define the coordinate system of the Fourier space, by considering (4.48) and (4.49). The error, induced by this procedure, leads to an uncertainty of the coordinate system axes of approximately 2 %. Fig. 4.33 shows the resulting normalized Fourier space intensity distributions of both cases on a logarithmic color scale.
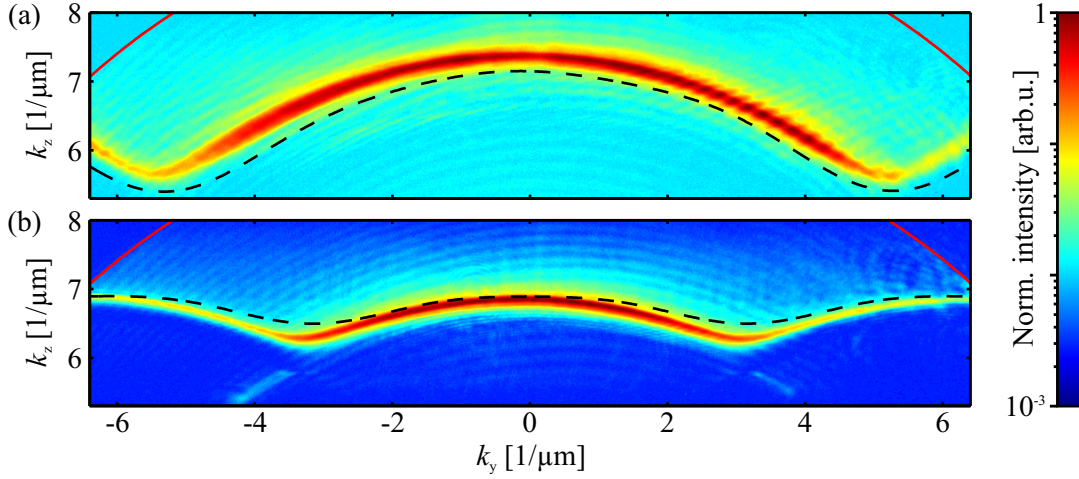
Figure 4.33: Fourier space intensity distribution corresponding of the plasmonic discrete diffraction, shown in Fig. 4.32 (a) and (b), respectively. The red dotted circles correspond to the border of the objective's BFP, while the black dotted lines correspond to the result of the Comsol Multiphysics based eigenmode expansions.

Both Fourier space images of the discrete diffraction in a plasmonic system, as depicted in Fig. 4.32, exhibit one band of excited modes, symmetrically arranged around $k_y = 0$. In comparison to the CMT calculations both results resemble the expected behavior as period and band width of the structures decrease with increasing DLSPPW separations. However, in comparison to Fig. 4.16, a clear deviation of the absolute amplitude values is obvious, related to the previously neglected non next neighbor coupling effects.

In contrast, the experimental data is in quantitative agreement with the band structure, calculated with the help of Comsol Multiphysics (see black dotted lines in Fig. 4.33). The remaining small distortion and shift can be explained with deviations of the fabricated sample from the shape assumed in the calculations. Based on the AFM measurements, presented in the last section, the denser packed array has a slightly higher DLSPPW thickness compared to the simulated environment, leading to a higher effective refractive index. In case of the second array, the contrary explanation takes place.

4.5.2 Plasmonic implementation of the SSH model: Bulk properties

Next, we consider DLSPPW arrays with a constant dimerization, corresponding to a single topological domain of the SSH model. Similar as it was the case in the theoretical discussions, in these domains we investigate the evolution of an SPP wavepacket launched in the bulk material. Therefore, the following procedure is repeated for each fabricated array: the laser is focused on the grating coupler, fabricated on top of a DLSPPW in the middle of such a single topological domain. Similar to the last section, the laser spot as well as the left propagating SPPs are filtered out before the images of real and Fourier space are captured. On both types of images the same post-processing is applied, as described in the last section.

Real space image

We start with the captured real space images of the DLSPPW arrays. The intensity distribution of propagating SPPs in an array with $d_{small} = 600\,nm$ and $d_{large} = 1000\,nm$ is shown in Fig. 4.34, on a logarithmic color scale.
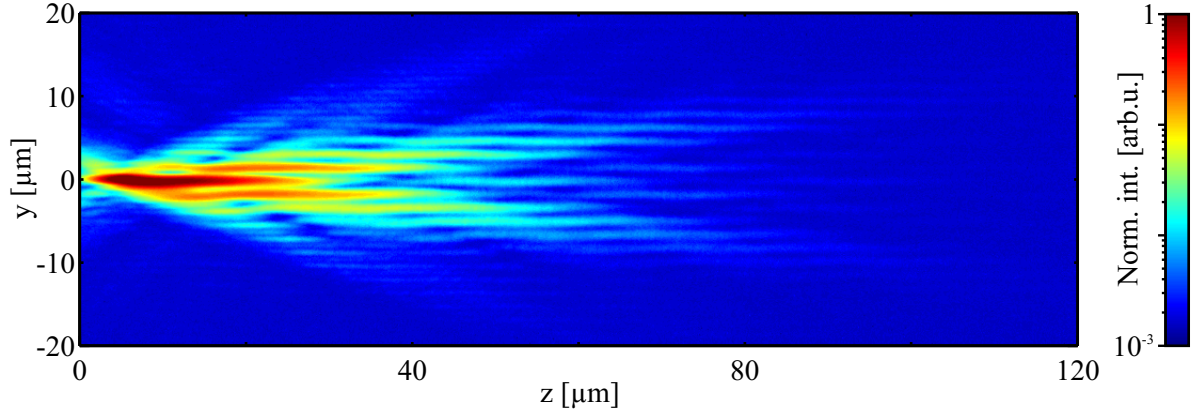

Figure 4.34: Real space intensity distribution of propagating SPPs in the bulk material of a single topological domain, consisting of a DLSPPW array with $d_{small} = 600\,nm$ and $d_{large} = 1000\,nm$. The excitation of the propagating SPPs takes place at z = 0.

The SPPs are excited at z = 0 and propagate in the positive z-direction. While at the origin, all the intensity is confined in the central DLSPPW, the distribution broadens with increasing distance, similar to the already discussed case of discrete diffraction. However, due to the smaller coupling in every second DLSPPW, the width of the distribution in y-direction is narrower. In contrast to the numerical results resulting from the CMT calculations, shown in Fig. 4.17, two additional side lobes can be recognized. In accordance to the results based on the Comsol Multiphysics eigenmode expansion, this can, however, be explained by a non vanishing non next neighbor coupling. It thus successfully mimics the behavior of the bulk material as described by the SSH model.

Note, that similar to the previous case, Fig. 4.34 images the intensity distribution on top of the gold film and not the discrete amplitude distribution of the DLSPPWs. Hence, the broader lines in the experimental image stem from merging intensities of neighboring DLSPPWs and hence correspond to more than one DLSPPW.

The theoretical calculations predicted that a change of the coupling has a strong influence on the propagation of SPPs in a DLSPPW array. This dependency is investigated by exciting propagating SPPs in a DLSPPW array with an increased d_{large}. The resulting intensity distribution in an array with the same d_{small} but $d_{large} = 1600\,nm$, is shown in Fig. 4.35.

Clearly, a narrowing of the intensity distribution in the z-direction can be observed. In contrast to Fig. 4.34, the final intensity distribution at the right end of the image is, in y-direction, distributed over approximately $10\,\mu m$, only. In accordance to the theoretical calculations, however, this arises from the drastically reduced coupling due to the larger DLSPPW separations between every second DLSPPW.

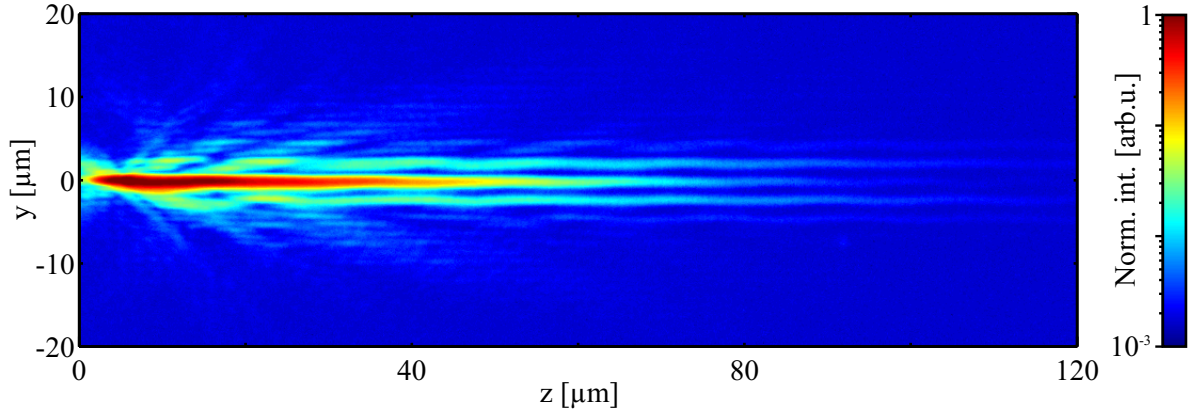Similar measurements were performed on arrays with $d_{small} = 800\,nm$, but the same values of

Figure 4.35: Real space intensity distribution of propagating SPPs, excited at z = 0 in a DLSPPW array with d_{small} = 600 nm and d_{large} = 1600 nm. This array mimics single topological domain with a larger d_{large} than the one imaged in Fig. 4.34.

d_{large}. They provided the same behavior. Simply the opening angle was further reduced due to the larger d_{small}. Also these results were in good agreement with the corresponding eigenmode expansions based on Comsol Multiphysics and demonstrated the plasmonic realization of the SSH model.

Fourier space image

The Fourier space image of propagating SPPs in an array with d_{small} = 600 nm and d_{large} = 1000 nm, corresponding to the real space distribution, shown in Fig. 4.34, is depicted in Fig. 4.36.

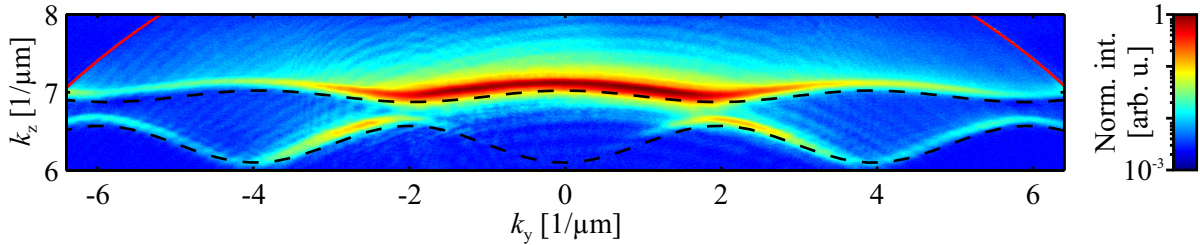Figure 4.36: Fourier space image of propagating SPPs in an array with d_{small} = 600 nm and d_{large} = 1000 nm, corresponding to the bulk material of an SSH topological insulator (see the real space image in Fig. 4.34). The dashed black lines correspond to the two bands provided by the Comsol Multiphysics based calculations, while the red lines indicate the border of the objective's BFP.

As expected from the theoretical results, this image exhibits two distinct bands of high intensity, separated by a band gap. Here, in comparison to the lower band the top band is strongly squeezed in k_z-direction. This significant asymmetry deviates from the expectations based on the CMT calculations. It was, however, already anticipated by the results of the Comsol Multiphysics based eigenmode expansion. Consequently, the positions of the experimentally determined bands resemble the bands calculated with the help of Comsol Multiphysics that are depicted as dashed black lines. The remaining deviations can be explained once more by the previously

neglected non next neighbor coupling and the proximity effect. Therefore, this image mimics a band structure representing the excited bulk modes of a topological insulator, described by the SSH model.

In order to further investigate the influence of an increasing separation d_{large} on the angular spectrum, the Fourier space image of a DLSPPW array with $d_{small} = 600$ nm and $d_{large} = 1600$ nm is captured and shown in Fig. 4.37.
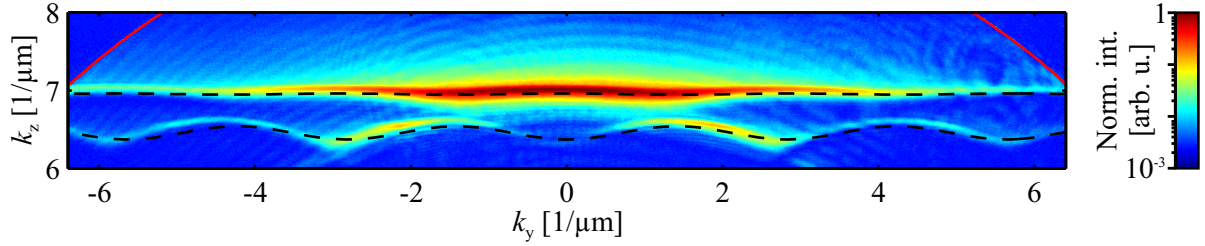

Figure 4.37: Fourier space image of propagating SPPs in an array with $d_{small} = 600$ nm and an increased $d_{large} = 1600$ nm (see the real space image in Fig. 4.35). This array mimics the bulk material of a single topological domain with a smaller coupling compared to the one shown in Fig. 4.36. The dashed black lines correspond to the two bands provided by the Comsol Multiphysics based calculations, while the red lines indicate the border of the objective's BFP.

Again, two distinct bands separated by a band gap can be recognized. In comparison to the previously discussed case, the asymmetry of the widths of both bands in the Fourier space increased, while the size of the band gap remains almost unchanged. This trend was already expected from the theoretical considerations based on Comsol Multiphysics. In this case the calculations (depicted as dotted black lines), however, the experimental results offer larger deviations than in Fig. 4.36. This deviation stems from the changed DLSPPW heights and widths, due to the proximity effect, as confirmed by the AFM measurements. The decreased size of the DLSPPW profile in this particular case leads to a smaller effective refractive index, which is accompanied by a shifted position of the bands in the Fourier space image.

Gap size and band asymmetry

In order to characterize the deviations between the experimental results and the ideal SSH model, the gap sizes and band asymmetries are investigated for all fabricated bulk material structures. Therefore, the following procedure is performed on the corresponding Fourier space images. The course of both bands is extracted from the images by performing Gaussian fits along the k_z-direction. Subsequently, each band is fitted by a cosine-shaped function. From the fitted functions the widths (A_{top} and A_{bottom}), as well as the maxima of the lower bands (K_{max}) and the minima of the top bands (K_{min}) are extracted. The band gap sizes are then calculated by $K_{max} - K_{min}$, while the asymmetry of both bands is determined as A_{bottom}/A_{top}. The resulting data is plotted in Fig. 4.38, together with values stemming from the Comsol Multiphysics based calculations.

Considering initially the measured asymmetries of the two band widths, as plotted in Fig. 4.38 (a), the experimental results obtain an increasing asymmetry for larger separations d_{large}. This trend

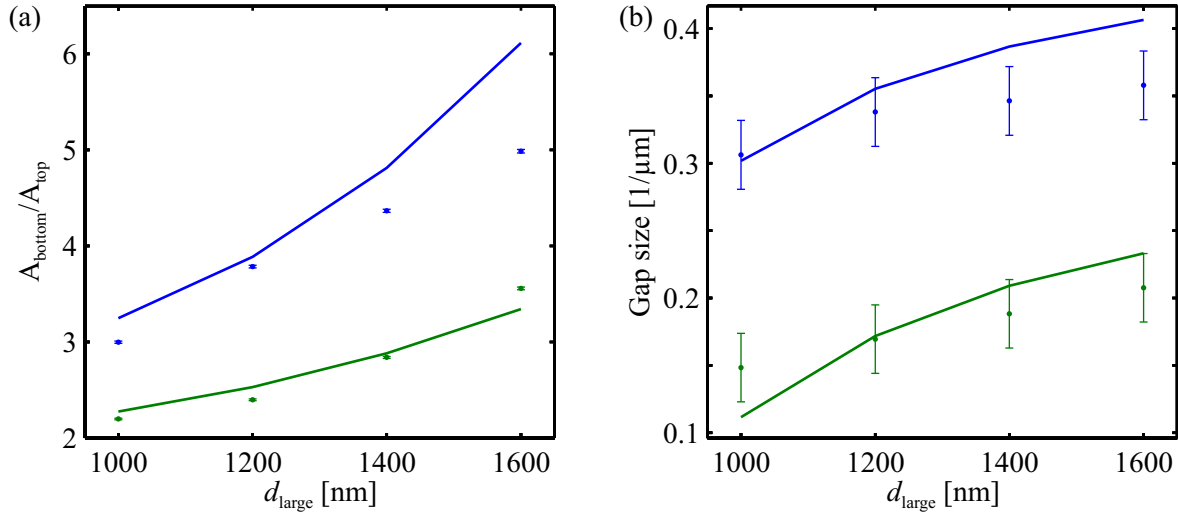Figure 4.38: (a) Asymmetry ($A_{\text{bottom}}/A_{\text{top}}$) of the bands for $d_{\text{small}} = 600$ nm (blue) and $d_{\text{small}} = 800$ nm (green) as a function d_{large}, as extracted from the Comsol Multiphysics based calculations (solid lines) and experimental results (circles), respectively. (b) The corresponding gap sizes.

is in good agreement with the Comsol Multiphysics based calculations (lines in Fig. 4.38 (a)). However, as a result of the decreasing size of the fabricated structures related to the proximity effect, the deviations from the calculations increase for larger values of d_{large}. A similar behavior is obtained by the by the experimentally determined band gap sizes (depicted as points in Fig. 4.38 (b)). They also exhibit the expected increase with increasing d_{large}. In this case, the slope deviates from the Comsol Multiphysics based calculations (lines in Fig. 4.38 (b)) with increasing d_{large}. Analog to the previous case, also this can be explained by the proximity effect.

Note, that the measurement errors, depicted in Fig. 4.38, take into account only the errors stemming from the manual fitting procedure, being a part of the calibration of the Fourier space images. The fabricational errors, induced by the proximity effect, are not included. In fact, they are the main contribution to the observed deviations.

4.5.3 Plasmonic implementation of the SSH model: Edge states

As a next step, edges between two different topological domains are investigated. Such geometries are of particular interest, since the SSH model as well as the theoretical calculations predicted the possibility of an excitation of topologically protected edge states in this case.
In order to experimentally demonstrate this behavior, the following procedure is repeated for all fabricated arrays. The sample is positioned in the setup in such a way, that the laser is focused on the isolated DLSPPW in the middle of the transition area, being equivalent to the excitation in the central DLSPPW discussed in the theoretical calculations. In order to reduce the influence of the proximity effect, in the fabrication of the structure, the dose of the central DLSPPW was slightly increased relatively to the design dose (to 147% of the nominal dose).
Similar to the previous cases, again, the left propagating SPPs and the directly transmitted laser beam are filtered out by placing a knife edge in BFP'. Subsequently, on both types of resulting

images, the same post-processing is applied as discussed in the previous sections.

Real space images

The normalized real space image of propagating SPPs, excited in the center of a DLSPPW array with $d_{small} = 600\,\text{nm}$ and $d_{large} = d_{gap} = 1000\,\text{nm}$, is shown in Fig. 4.39.
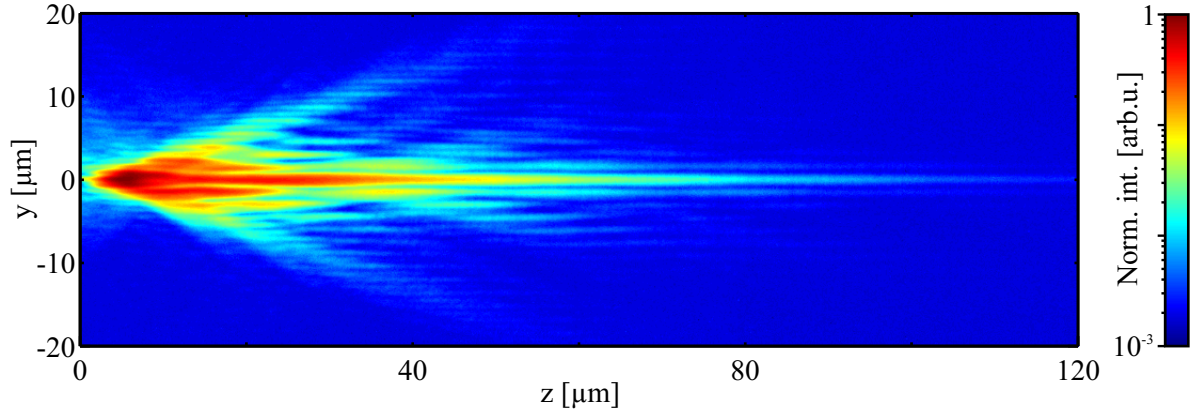

Figure 4.39: Real space image of an excited topologically protected edge state in a DLSPPW a array with $d_{small} = 600\,\text{nm}$ and $d_{large} = d_{gap} = 1000\,\text{nm}$. The excitation takes place at z = 0.

Clearly, beginning at the point of excitation (z = 0), a high fraction of the intensity is confined to the central DLSPPW for the complete imaged distance of $120\,\mu\text{m}$. It is therefore, according to the theoretical considerations, in fact, the experimental demonstration of the excitation of a topologically protected edge state in a plasmonic system. Analogue to the previously discussed case, the remaining broadening in y-direction, which can be observed mainly in the left half of the image, can be explained by the excitation of bulk modes of the DLSPPW array. A comparison to the results calculated with the Comsol Multiphysics based eigenmode expansion that are depicted in Fig. 4.24, reveals an excellent agreement.

In order to further investigate the dependency of the excitation of such an edge state on the DLSPPW separations, the same measurement is performed for a DLSPPW array with the same $d_{small} = 600\,\text{nm}$ but a larger $d_{large} = 1600\,\text{nm}$. The resulting intensity distribution of SPPs propagating in this array, is depicted in Fig. 4.40 on a logarithmic color scale.
Similar to the previous case, a large fraction of the intensity is confined to the central DLSPPW in the complete depicted area. Here, due to the decreased coupling to every second DLSPPW, the intensity in the neighboring DLSPPWs even decreased. Therefore, this image represents a second experimental demonstration of the excitation of a topologically protected edge state in a DLSPPW array. Again, the broadening of the intensity distribution in the left half of the image can be assigned to the excitation of bulk modes. Its reduced spreading in propagation direction is also induced by the decreased coupling as it is accompanied by the larger DLSPPW separations. This behavior is consistent with the theoretical predictions and the already presented experimental results. Furthermore, the overall form also of this intensity distribution is again in good correspondence with the theoretical results obtained from Comsol Multiphysics.
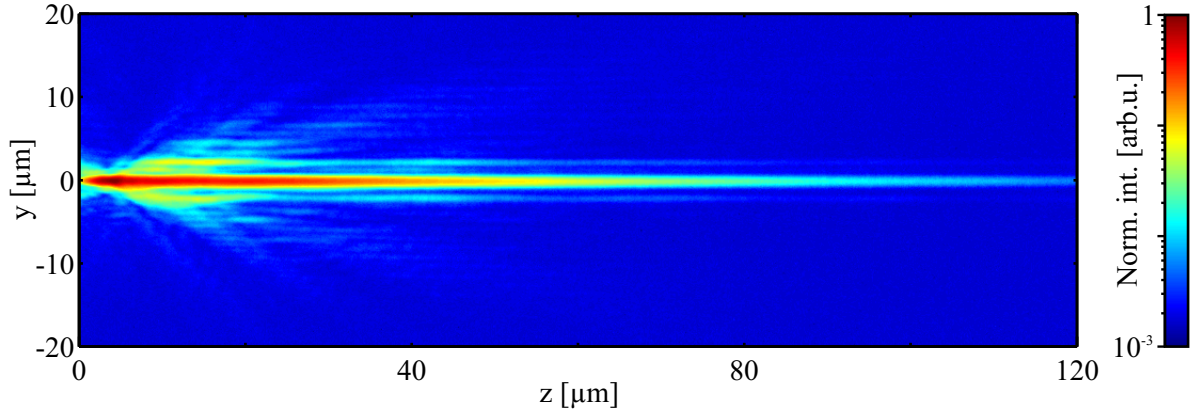
Figure 4.40: Real space image of an excited topologically protected edge state in a DLSPPW array with $d_{small} = 600$ nm and a larger $d_{large} = d_{gap} = 1600$ nm. The excitation takes place at z = 0.

Fourier space images

Since the real space images already demonstrated the excitation of a topologically protected edge state in a plasmonic system, the investigation of the corresponding band structure is expected to contain more information on this states. The Fourier space image corresponding to Fig. 4.39, is shown in Fig. 4.41.
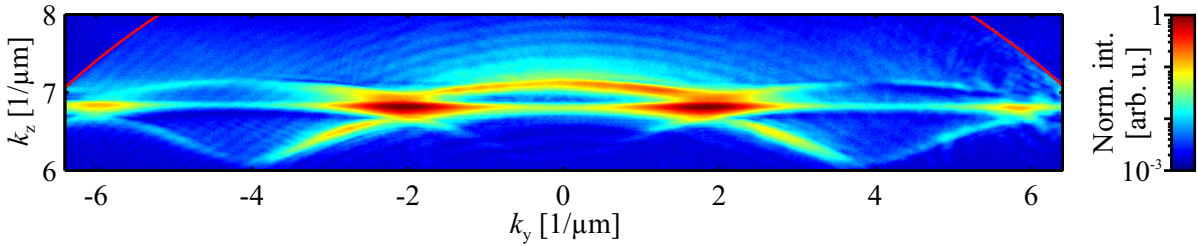

Figure 4.41: Fourier space image of an excited topological protected edge state, corresponding to the real space image depicted in Fig. 4.39. The red lines correspond to the border of the objective's BFP.

The horizontal line of high intensity in the band gap of the already known two cosine-shaped bands represents a mode, confined in a single DLSPPW. Based on the theoretical considerations, this line corresponds to the excited topologically protected edge state in the central DLSPPW (see Fig. 4.39). Hence, this image represents the first experimental observation of a band structure including an excited topologically protected edge state in a plasmonic system. It herein exhibits an excellent agreement to the theoretical results, depicted in Fig. 4.25. Consistent with the theoretical results, also in the experimental image, the edge state is not located in the middle of the band gap, since the symmetry of the SSH model is not perfectly fulfilled in realistic DLSPPW arrays.

In order to investigate the dependence of the edge state's properties on the effective refractive index of the central DLSPPW, the dose of the central DLSPPW and with it its height is varied. Initially, it is decreased to 133% and in a second step increased to 161%, relatively to the nominal

dose. The Fourier space images of excited propagating SPPs in the resulting DLSPPW arrays are shown in Fig. 4.42.
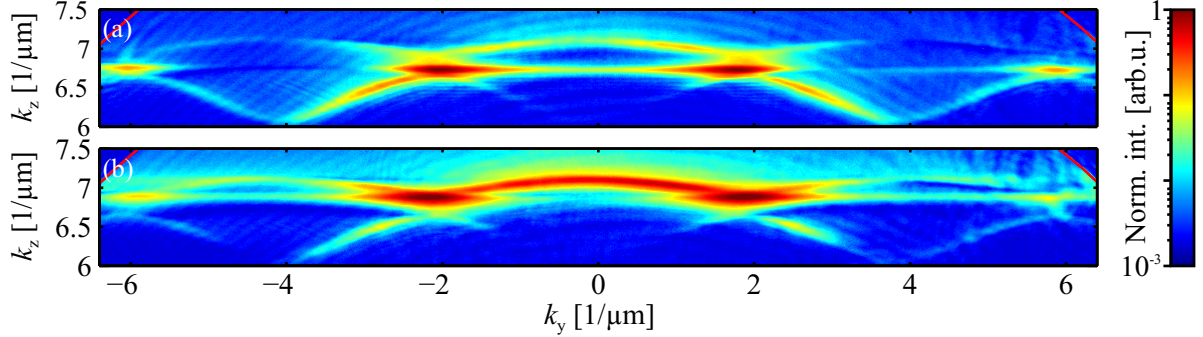

Figure 4.42: Fourier space images of excited topologically protected edge states in DLSPPW arrays with $d_{small} = 600\,\text{nm}$ and $d_{large} = d_{gap} = 1000\,\text{nm}$ an a slightly smaller (a) and larger (b) design dose of the central DLSPPW. The red lines correspond to the border of the objective's BFP.

Both cases exhibit a state in the band gap in between the two cosine-shaped bands similar to the previously discussed case. However, the changed design dose of the central DLSPPW has a strong influence. While a smaller design dose of the central DLSPPW (Fig. 4.42 (a)) leads to a shifting down of the edge mode, an increased dose (Fig. 4.42 (b)) leads to a lifting of the edge mode. In the latter case the edge mode even touches the top band and is hence strongly disturbed. This corresponds to the theoretically expected behavior of a system with a changing effective refractive index of the central DLSPPW.

Now, the influence of a larger separation d_{large} on the gap state is investigated for a DLSPPW array with $d_{large} = d_{gap} = 1600\,\text{nm}$, and an identical $d_{small} = 600\,\text{nm}$. The design dose of the central DLSPPW is chosen to be again 147%. The resulting Fourier space image (corresponding to the real space image shown in Fig. 4.40) is depicted in Fig. 4.43.
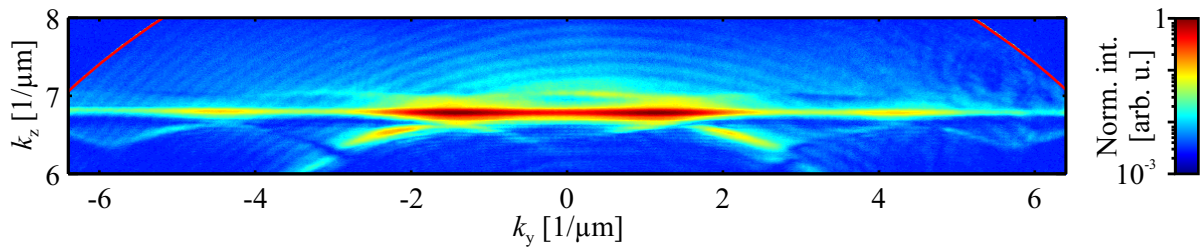

Figure 4.43: Fourier space image of an excited topological protected edge state, corresponding to the real space image depicted in Fig. 4.40. The red lines mark the border of the objective's BFP.

The horizontal line of high intensity represents once more a mode confined to a single DLSPPW. Due to its position in the band gap, in combination with the real space image depicted in Fig. 4.40, it can be assigned once more to the excitation of a topologically protected edge state in the central DLSPPW. Therefore, it is a further experimental observation of a band structure including an excited topologically protected edge state. Furthermore and in accordance to the theoretical

considerations, the absolute width of the band structure and the band widths decreased due to the smaller coupling, as induced by the larger separations (see Fig. 4.38).

Investigation of the edge state's mode profile

As discussed in section Subsec. 4.2.1(SSH model), the edge state has a vanishing amplitude on every other site. Hence, it should not be excited if we launch a SPP in one of the direct neighbors of the central DLSPPW. To test this prediction we have fabricated a grating coupler on the right end of the DLSPPW which is located directly above the central waveguide (see Fig. 4.28). Due to the changed excitation scheme, the knife edge in BFP' is now placed in such a way, that the right propagating SPPs and the laser beam is filtered out. The remaining post-processing performed on the real space image is the same as in the previous sections.
The resulting normalized intensity distribution of SPPs, propagating now in negative z-direction in an array with $d_{small} = 600\,nm$ and $d_{large} = d_{gap} = 1000\,nm$ is depicted in Fig. 4.44.
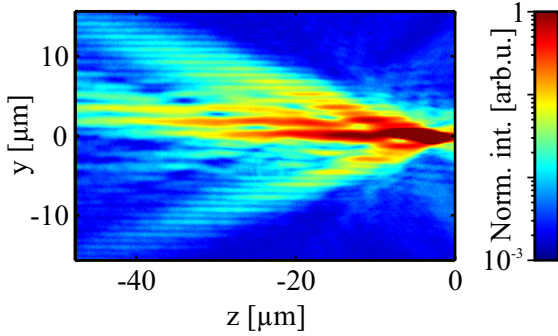

Figure 4.44: Intensity distribution of SPPs, propagating in negative z-direction, excited on the right end of the DLSPPW right next to the central DLSPPW, in an array with $d_{small} = 600\,nm$ and $d_{large} = 1000\,nm$.

In contrast to the already discussed cases, this image exhibits a clear asymmetric intensity distribution, due to the transition between the two topological domains, centered at y = 0. However, no intensity is confined to the central DLSPPW and hence the distribution does not contain an excited topologically protected edge state. In excellent accordance to the theoretical considerations, this experimentally demonstrates the mode profile of the topologically protected edge state. The remaining broadening can again be explained by the excitation of bulk modes, similar to the previous cases. However, in contrast to Fig. 4.34, a larger fraction of the intensity is contained in the outer lobes of the distribution. As expected from the theoretical considerations, this can be traced back to a slightly changed excitation scheme of the propagating SPPs.

4.5.4 Plasmonic implementation of the SSH model: Larger transition area

The last section concentrated on the investigation of propagating SPPs, excited at the boundary of two domains with different topological properties. This section focuses on a larger transition area. For that purpose d_{gap} is reduced to 600 nm, as it leads to a closely spaced realization of five DLSPPW in the central region of the array, corresponding to the case discussed in the theoretical part of this chapter. The remaining design is kept fixed. Again, SPPs are excited by the grating on top of the central DLSPPW and propagate in positive z-direction. The knife edge in the BFP' is once more placed such that it blocks the laser beam and the SPPs, propagating to the left.

The corresponding real space image of a DLSPPW array with $d_{small} = d_{gap} = 600\,nm$ and $d_{large} = 1000\,nm$ is calibrated analogously to the previous images. The resulting intensity distribution, is shown in Fig. 4.45.
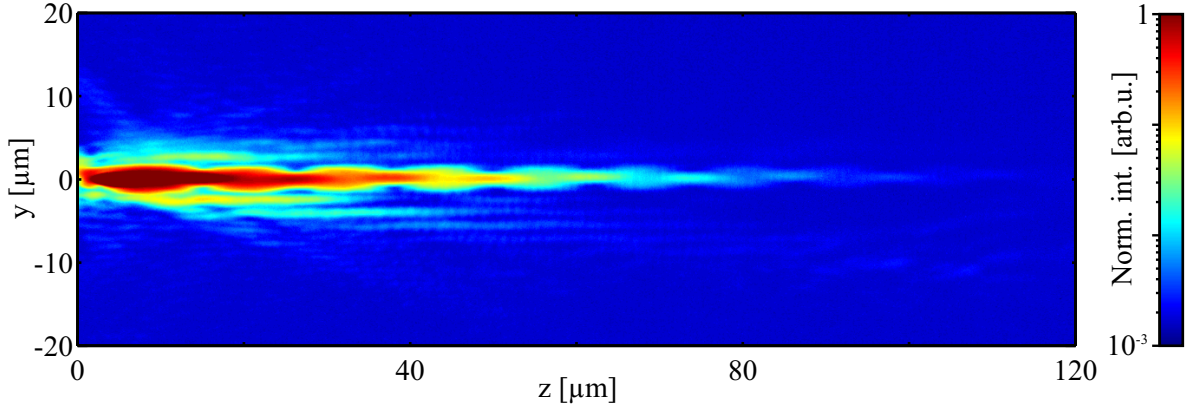

Figure 4.45: Real space image of a DLSPPW array with $d_{gap} = d_{small} = 600\,nm$ and $d_{large} = 1600\,nm$, implementing a larger transition area in a plasmonic system.

In contrast to the previously discussed results, this distribution exhibits a clear beating pattern in the central area of the DSLPPW array, starting directly after the SPP excitation at z = 0. Based on the theoretical predictions (see Fig. 4.21) this indicates on the presence of more states, localized in the center of the array. Analogously to the previous discussions, the slight broadening of the intensity distribution can be assigned once more to the additional excitation of bulk modes.

In order to verify the assumption of the excitation of additional localized states and to investigate the topologically protected edge state, the corresponding Fourier space image has to be examined. The resulting intensity distribution is depicted in Fig. 4.46, on a logarithmic color scale.
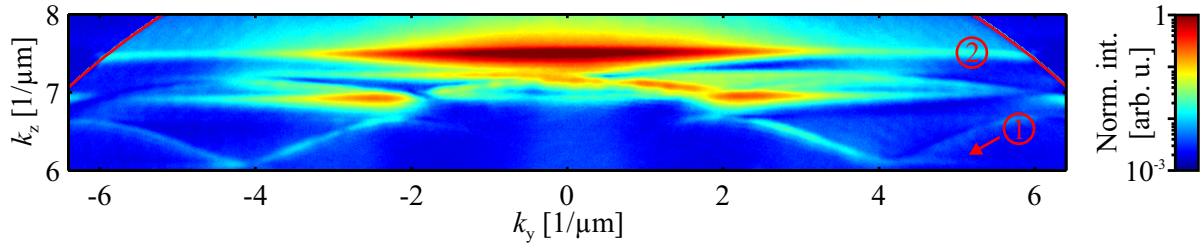

Figure 4.46: Fourier space image, corresponding to Fig. 4.45. The numbers highlight the newly occurred modes. The red lines correspond to the border of the objective's BFP.

In comparison to the case of two different and directly attached topological domains (compare to Fig. 4.41), the *k*-space image contains new excited modes. One additional state can be seen below the lower band (1) and a bright one above the former top band (2). In accordance to the theoretical discussion, both correspond to modes, localized in the central area of the array, as expected from the discussion of the corresponding real space image. Nevertheless, still an edge state is visible in the band gap. However, due to the changed type of geometry it is slightly

covered. In comparison to the theoretical results shown in Fig. 4.22, one deviation is apparent. The horizontal line indicated by (2) is shifted to higher values of k_z, than expected. This again stems from the influence of the proximity effect, since the distances of the central DLSPPW are strongly reduced, leading to a larger size, accompanied by a larger effective refractive index. This demonstrates the presence of a topologically protected edge state in a system including also a large transition area and more localized states in the central part of the array.

Photochromic switching of surface plasmon polaritons

This chapter concentrates on the investigation of the photochromic switching of plasmonic systems. After a short introduction on the functionality of the used photochromic materials, two different plasmonic systems are discussed in detail.

In the first plasmonic system, photochromic materials are used to manipulate Fano resonances in photochromic metallic photonic crystal slabs. The working principle of this approach is explained with the help of a coupled oscillator model, supported by more rigorous scattering matrix based calculations. After introducing positive tone electron beam lithography (pEBL) as the applied fabrication method and the optical setup, utilized for the experimental investigations, the experimental results are presented.

The second part of this chapter focuses on the manipulation of SPPs, propagating at the interface of a gold film, covered with a photochromic material. On this occasion, two possible manipulation methods are discussed theoretically: the globally and the locally switching of the photochromic material's state. Based on leakage radiation microscopy, both approaches are investigated experimentally. As a result, the manipulation of propagating SPPs by globally switching the photochromic layer is presented. In addition, also first results on the manipulation of SPPs by switching the layer even locally, are discussed.

5.1 Photochromic materials

Photochromic molecules belong to a chemical species that provides two different isomers with differing properties, e.g., a different complex refractive index. Upon illumination with light, these molecules undergo chemical reactions, leading to a reversible conversion from one isomer to the other. Out of the great variety of molecules offered by this chemical species, in this thesis, we make use of the two cross-linkable photochromic molecules XDTE and XTPA, provided and synthesized by the group of Prof. Dr. Klaus Meerholz.[1]

---

[1] Institut für Physikalische Chemie, Universität zu Köln

XDTE

The first molecule presented in this thesis is the dithienylethene derivative XDTE [108]. It exhibits two thermally stable and non-volatile [109] isomers (the molecular strucutre is sketched in Fig. 5.1 (a)), which can be reversibly transferred into each other by light induced chemical reactions [110]. The complex refractive indices of both isomers (n_{XDTE-A} and n_{XDTE-T}) are plotted in Fig. 5.1 (b).
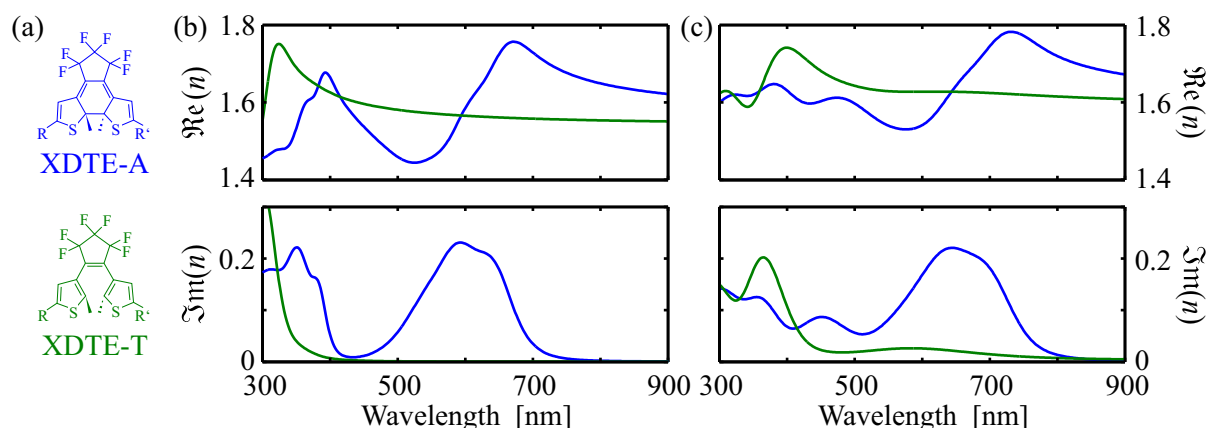

Figure 5.1: (a) Molecular structure of XDTE-A and XDTE-T [111]. (b) Real and imaginary part of the complex refractive indices of XDTE-A (blue) and XDTE-T (green), with the data taken from Ref. [111]. (c) Complex refractive indices of XTPA-A (blue) and XTPA-T (green), respectively.

The complex refractive index of XDTE-A (depicted as blue lines in Fig. 5.1 (b)) exhibits a large imaginary part, in the visible spectral range with a maximum at approximately 610 nm wavelength. Simultaneously and in accordance with the Kramers-Kronig relation, its real part is strongly dispersive in this spectral range.

The illumination of these molecules with red light induces a ring opening reaction, transferring XDTE-A to the other isomer XDTE-T. The optical properties of this isomer (depicted as green lines in Fig. 5.1 (b)) differ from XDTE-A. It has a negligible absorption in the visible part of the spectrum, as indicated by the vanishing and almost constant imaginary part of the complex refractive index. Corresponding to this, its real part in this spectral range is almost constant. In comparison to XDTE-A, the point of highest switching efficiency ($n_{XDTE-A} - n_{XDTE-T}$) is located at approximately 672 nm wavelength for the real part of the refractive index and at approximately 594 nm wavelength for its imaginary part.

By illumination with UV light, XDTE-T undergoes a ring closing reaction, transferring it back to XDTE-A. The overall efficiency of this procedure in terms of the fraction of switched molecules can be as large as approximately 95% [108]. However, in addition to the back conversion, the illumination with UV light can also lead to unwanted side reactions, resulting in an overall optical fatigue. The probability of this side reactions herein depends on the intensity and the wavelength of the used light source as well as on the layer thickness and the grade of conversion [111]. Previous experiments, carried out in the group of our collaborators, revealed a reduction of the overall photo-response of approximately 20% after 150 switching cycles [111].

XTPA

The second cross-linkable molecule utilized in this thesis is XTPA [112]. Similar to XDTE it is a dithienylethene derivative, which offers deviating optical properties. This manifests in a different complex refractive index distribution of both isomers, as measured by Thorsten Umbach[2] for XTPA films on a glass substrate. Both distributions ($n_{\text{XTPA}-\text{A}}$ and $n_{\text{XTPA}-\text{T}}$) are plotted in Fig. 5.1 (c).

The highly absorptive isomer, labeled as XTPA-A, offers a maximum of absorption in the visible spectral range at approximately 644 nm wavelength, combined with a highly dispersive real part of the complex refractive index in the same spectral range. Analogously to XDTE, an illumination with red light, converts this isomer (XTPA-A) to the second isomer (XTPA-T). XTPA-T now offers a negligible absorption in the visible spectral range, accompanied by an almost constant real part of the complex refractive index. A back conversion can be achieved by illumination of UV light, inducing a ring closing reaction in the molecule, converting XTPA-T to XTPA-A. The maximal conversion achieved within the switching procedure is approximately 91 % [112].

In comparison to XDTE, the highest switching efficiencies ($n_{\text{XTPA}-\text{A}} - n_{\text{XTPA}-\text{T}}$) of the real and imaginary parts of XTPA can be found at longer wavelengths. While the maximal difference in absorption takes place at approximately 644 nm, the highest switching efficiency of the real part of the complex refractive index is located at approximately 731 nm.

Switching times

While the switching of the used photochromic molecules from one state to another happens in the ps time range [113, 114], the time needed to switch a complete layer of material with red/UV light mainly depends on the intensity of the light source itself. In the case of flood illumination of an XDTE or XTPA layer, being accompanied by relatively low intensities, the switching times are in the range of minutes. Previous experiments approved that they can be even reduced to the range of seconds, if a tightly focused light source is utilized. However, too high intensities lead to a permanent change of the material, destroying its switching functionality.

5.2 Photochromic switching of Fano resonances

The discussion of the spectral properties of both used photochromic materials in the last section revealed that the points of highest switching efficiency of the real and imaginary parts of the complex refractive indices are at different spectral positions. This fact can be used to investigate the influence of both changes on SPPs in distinct experiments. As a starting point, this section will concentrate on the interaction of SPPs with a photochromic material in a spectral range, in which the change of absorption is predominant. By comparing the two presented materials, shown in Fig. 5.1, XDTE reveals the highest change of absorption and hence is utilized in the first part of this section.

---

[2] Group of Prof. Dr. Klaus Meerholz, Institut für Physikalische Chemie, Universität zu Köln

In this context metallic photonic crystal slabs are particular interesting systems to investigate. Due to an interaction of localized SPPs with delocalized dielectric waveguide modes, such systems provide Fano resonances [53, 72, 115]. Since these resonances exhibit highly dispersive properties they are good candidates for switching applications [52]. In fact, the transmittance of such a system has been previously investigated by Nau et al. [116] on its dependency on photo induced changes in one of the wave guiding layers. The resulting small shifts of the spectral features in their experiments were, however, caused mainly by a changing real part of the refractive index in the used photo addressable polymer. In contrast to this, making use of the more pronounced change of the absorption of XDTE, let us anticipate an even larger influence on such system. By discussing the realization of this concept, this section mainly follows Ref. [111].

5.2.1 Fano resonances in metallic photonic crystal slabs

We start the discussion with a bare metallic photonic crystal slab, not incorporating a photochromic layer. The assumed design of this non-switchable metallic photonic crystal is sketched in Fig. 5.2. It consists of an array of identical gold wires (with height h and width w), arranged with a period p, on top of a dielectric layer with thickness d and refractive index $n_d = 1.9$.
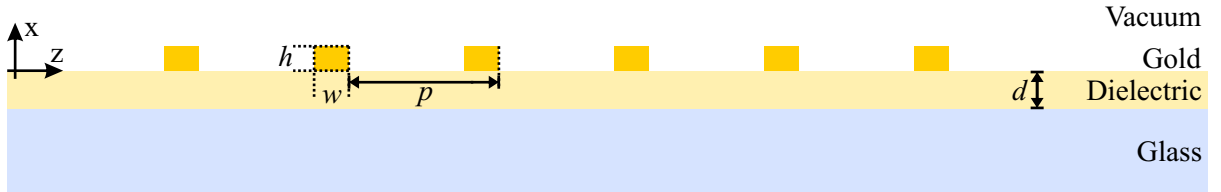

Figure 5.2: Metallic photonic crystal slab, consisting of gold wires with width w and height h, arranged with period p on top of a dielectric layer with thickness d, and fabricated on a glass substrate.

Dielectric slab waveguides

By neglecting firstly the gold wires included in the design, as it is sketched in Fig. 5.2, the system consist only of a dielectric layer sandwiched between a vacuum and a glass half-space. Such layer of a material with a high refractive index, surrounded by two lower index materials ($n_{vac} = 1$ and $n_{glass} = 1.5$), can act as a dielectric waveguide. The existence of waveguide modes for a given wavelength, however, depends strongly on the thickness d of the dielectric layer [69]. By taking the boundary conditions at both interfaces of the resulting waveguide into account, the following two characteristic equations for both, TM and TE modes of lowest order can be derived. With $k_d = k_0 n_d$, $k_{vac} = k_0 n_{vac}$, and $k_{glass} = k_0 n_{glass}$ it follows for the TE modes with a propagation constant β [115]:

$$d\sqrt{k_d^2 - \beta^2} = \arctan\left(\sqrt{\frac{k_d^2 - k_{vac}^2}{k_d^2 - \beta^2} - 1}\right) + \arctan\left(\sqrt{\frac{k_d^2 - k_{glass}^2}{k_d^2 - \beta^2} - 1}\right), \qquad (5.1)$$

and for TM-modes:

$$d\sqrt{k_{\mathrm{d}}^2 - \beta^2} = \arctan\left(\frac{n_{\mathrm{d}}^2}{n_{\mathrm{vac}}^2}\sqrt{\frac{k_{\mathrm{d}}^2 - k_{\mathrm{vac}}^2}{k_{\mathrm{d}}^2 - \beta^2} - 1}\right) + \arctan\left(\frac{n_{\mathrm{d}}^2}{n_{\mathrm{glass}}^2}\sqrt{\frac{k_{\mathrm{d}}^2 - k_{\mathrm{glass}}^2}{k_{\mathrm{d}}^2 - \beta^2} - 1}\right). \qquad (5.2)$$

Since these equations cannot be solved analytically, we use again the modal analyzer contained in the Comsol Multiphysics software package to get an insight into the complex dependencies. For this purpose, we search for the allowed modes of lowest order in a geometry, consisting of a dielectric with thickness d, sandwiched between a glass and a vacuum half space (similar to Fig. 5.2, by neglecting the gold wires). The simulations are performed for 400 nm – 900 nm wavelength in steps of 10 nm as well as thicknesses d of 100 nm, 120 nm, 140 nm, 160 nm, and 180 nm. The corresponding dispersion relations, deduced from the mode indices determined by the software, are plotted in Fig. 5.3 (a) and (b) together with the light lines for vacuum, glass, and the dielectric.
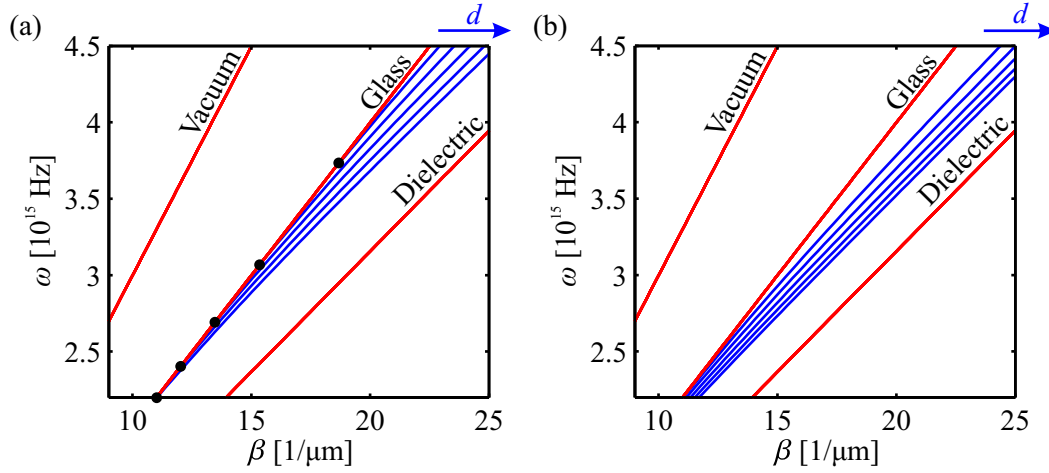

Figure 5.3: Calculated dispersion relations of (a) TM and (b) TE modes in a dielectric slab waveguide with core thicknesses (from the left to the right): $d = 100$ nm, 120 nm, 140 nm, 160 nm, 180 nm (colored in blue). The cutoff frequencies are indicated as black dots. Furthermore, the light lines of the dielectric layer as well as of glass and vacuum are depicted in red.

As expected, the dielectric's thickness has a direct influence on all modal dispersion relations (blue lines in Fig. 5.3). While the thickness d is increased, also the dispersion relations of the corresponding modes are shifted to larger values of β. This stems from the increasing influence of the material in larger waveguides. Nevertheless, as it can be recognized in Fig. 5.3 (b), for TE polarization all presented modes are existent over the whole spectral range and for all considered thicknesses. This is, however, different in case of TM polarization (see Fig. 5.3 (a)). Here, the cutoff frequencies of the different modes are marked with black dots. They indicate that the waveguide mode in a 140 nm thick dielectric layer is the first one that is supported over a broader part of the considered spectral range. This leads to the assumption that for the proceeding investigations it is the minimal reasonable thickness.

Metallic photonic crystal slabs

In the complete system, consisting of gold wires on top of the dielectric slab waveguide, the gold wire array can now serve as a grating coupler for the discussed dielectric slab waveguide [69]. Hence, if the incoming wave is polarized along the z-direction (TM polarization), as discussed in Sec. 2.4, the present design facilitates the simultaneous excitation of both, localized SPPs in the gold wires and delocalized waveguide modes in the dielectric slab waveguide [53, 54]. For this reason, we concentrate only on this polarization in the following discussions.

Based on the dispersion relations of the waveguide modes, depicted in Fig. 5.3 (a), the wavelength at which a waveguide mode is excited (waveguide resonance), can be controlled by linearly tuning the period of the grating. In contrast, the excitation wavelength of the localized SPPs (plasmonic resonance) depends to first approximation only on the profile of the gold wires [115]. Hence, the appearance of both effects can be controlled independently. In order to reduce the number of parameters, we restrict ourselves to a fixed plasmonic resonance at 610 nm wavelength, while the waveguide resonance is shifted by linearly changing the grating period.

The interaction of a plasmonic oscillation, exhibiting a resonance at Ω_{pl} and a damping of γ_{pl}, with a waveguide mode, having a resonance at Ω_{wg} and a damping of γ_{wg}, can be modeled by using a coupled oscillator model [72, 117]. Therefore, the equation of motion described by (2.23), is extended to [72]:

$$\ddot{\xi}_{\mathrm{pl}} + 2\gamma_{\mathrm{pl}}\dot{\xi}_{\mathrm{pl}} + \Omega_{\mathrm{pl}}^2\xi_{\mathrm{pl}} - \Omega_{\mathrm{c}}^2\xi_{\mathrm{wg}} = \frac{q_{\mathrm{pl}}}{m_{\mathrm{pl}}}E(t)\,, \tag{5.3}$$

$$\ddot{\xi}_{\mathrm{wg}} + 2\gamma_{\mathrm{wg}}\dot{\xi}_{\mathrm{wg}} + \Omega_{\mathrm{wg}}^2\xi_{\mathrm{wg}} - \Omega_{\mathrm{c}}^2\xi_{\mathrm{pl}} = 0\,, \tag{5.4}$$

with the charge q_{pl} and mass m_{pl} of the electron cloud, as well as the coupling constant Ω_{c} and the corresponding displacements ξ_i ($i \in \{\mathrm{pl}, \mathrm{wg}\}$). Here, analogously to the case described by (2.23), the plasmonic oscillation is externally driven by the electromagnetic wave $E(t)$. The waveguide mode, however, does only couple to the plasmonic mode, mediated by Ω_{c}. Hence, the plasmonic oscillation acts as an optical bright mode and the waveguide mode as optical dark mode.

Similar to the case discussed in Sec. 2.4, the plasmonic displacement induced by a monochromatic excitation can now be derived to [72]:

$$\tilde{\xi}_{\mathrm{pl}}(\omega) = \frac{q_{\mathrm{pl}}E_0(\Omega_{\mathrm{wg}}^2 - \omega^2 - 2\mathrm{i}\gamma_{\mathrm{wg}}\omega)}{m_{\mathrm{pl}}[(\Omega_{\mathrm{pl}}^2 - \omega^2 - 2\mathrm{i}\gamma_{\mathrm{pl}}\omega)(\Omega_{\mathrm{wg}}^2 - \omega^2 - 2\mathrm{i}\gamma_{\mathrm{wg}}\omega) - \Omega_{\mathrm{c}}^4]}\,. \tag{5.5}$$

By making use of (2.27) and the parameters of the plasmonic oscillation, listed in Sec. 2.4, an absorption spectrum for a waveguide resonance at Ω_{wg}, corresponding to the later presented experimental data, can be modeled by a coupling constant and a waveguide damping of $\Omega_{\mathrm{c}} = \Omega_{\mathrm{pl}}/4$ and $\gamma_{\mathrm{wg}} = \gamma_{\mathrm{pl}}/4000$, respectively. The resulting absorption spectra for five different waveguide resonance wavelengths are plotted in Fig. 5.4.

We start the discussion with the case of a large detuning ($\Delta\Omega = \Omega_{\mathrm{wg}} - \Omega_{\mathrm{pl}}$) of the waveguide and the plasmonic resonance, as it is the case in Fig. 5.4 (a). At this point, both resonances can be treated independently and are represented by two distinct peaks in the absorption spectrum.
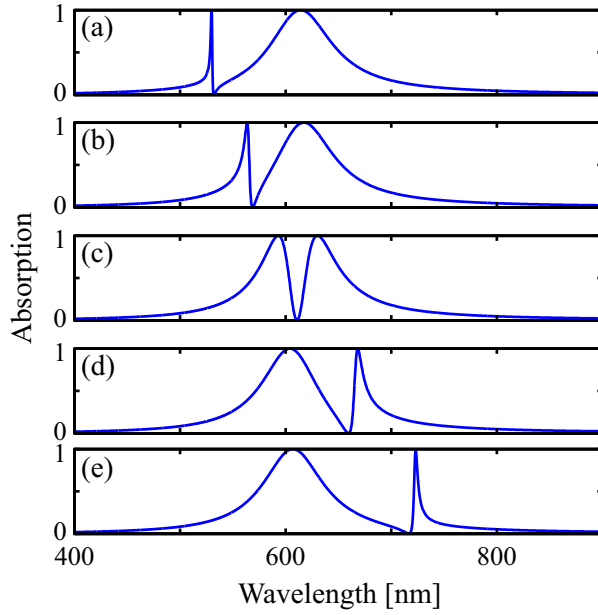
Figure 5.4: Normalized absorption of a coupled oscillator system for a plasmonic resonance at 610 nm wavelength and waveguide resonances at: 532 nm (a), 569 nm (b), 610 nm (c), 660 nm (d), and 717 nm wavelength (e).

The sharp peak corresponds to the waveguide resonance, while the broad peak, centered at 610 nm wavelength, is generated by the plasmonic resonance. If the detuning is decreased by shifting the waveguide resonance to higher wavelengths, both effects start to interact with each other [118]. Hence, the peaks cannot be assigned to a single resonance any more, but to a hybrid-type of effect. This manifests in the fact that the waveguide-like and the plasmon-like peaks perform an avoided crossing, as it can be recognized in Fig. 5.4 (b)–(e). The strongest interaction herein occurs for a zero detuning, when both resonances overlap. In this case, the destructive interference of both modes leads to a vanishing absorption of the system.

Such avoided crossing was previously assigned to the formation of a waveguide plasmon polariton [53, 54, 115]. Furthermore, this asymmetric type of line shape, originating from the interaction of a spectrally broad plasmonic resonance with a spectrally sharp waveguide resonance, is similar to a Fano resonance [48]. Hence, strongly dispersive features, as they are typical for such resonances [52], can be also expected for the present case.

Scattering matrix based calculations

The presented coupled oscillator model is useful to examine the interaction of two oscillators of known resonance wavelength and damping, as well as a known coupling constant. However, in real experimental situations these parameters are not known exactly. Therefore more rigorous calculations are necessary.

In this thesis an already existing script is used that bases on a scattering matrix method, extensively discussed in [119, 120]. In the course of that, in each layer of the system (vacuum, gold wires in vacuum, dielectric, glass) the electric field is decomposed into plane waves, corresponding to the Bragg harmonics of each layer. Together with the Maxwell equations, this results in a system of linear equations of a dimension that is determined by the number of the considered Bragg harmonics. After solving the resulting eigenvalue problem via transfer matrix formalism, the scattering matrix of the complete system is calculated. The accuracy of

the transmission, calculated by this formalism, depends on the number of considered Bragg harmonics. A good trade off between accuracy and calculation speed is found for a number of 50 Bragg harmonics.

Such calculations are performed for a TM polarized plane wave with wavelengths between 400 nm and 900 nm, impinging on an array of gold wires with a height of 40 nm and width of 90 nm, being arranged regularly with periods between 340 nm and 500 nm, on top of a dielectric waveguide with 140 nm thickness. The resulting extinction spectra (negative decadic logarithm of the transmission) are plotted in Fig. 5.5 (a) column-wise and with the extinction spectrum of a bare dielectric coated glass substrate as reference.
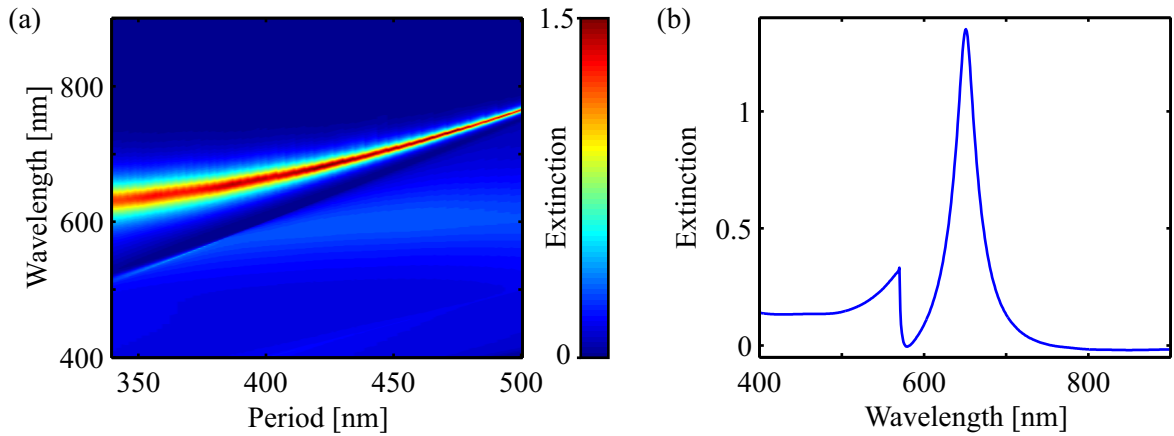
Figure 5.5: (a) Calculated extinction spectra of gold gratings with wires of 90 nm width, 40 nm height as well as periods between 340 nm and 500 nm, on a glass substrate with a dielectric coating of 140 nm thickness. (b) Extinction spectrum for a grating of 380 nm period, extracted from the data displayed in (a).

The extinction spectrum of the metallic photonic crystal slab with the smallest grating period, is located at the left border of Fig. 5.5 (a). I exhibits two spectral features at approximately 500 nm and 650 nm wavelength. Herein, the sharp peak can be assigned to the waveguide resonance, while the broader peak stems from the plasmonic resonance. In between both peaks, the minimum of the extinction, expected from the coupled oscillator model, can be recognized. As the period of the gold wire grating increases, accompanied by a shift of the waveguide resonance to higher wavelengths (compare Fig. 5.3 (a)), the interaction of both effects leads to an avoided crossing of the waveguide-like and plasmon-like peaks. Analogue to the coupled oscillator model, this behavior is the clear signature of the formation of a waveguide plasmon polariton [53, 54].

More insight into this hybridized effect is given by the extinction spectrum of a structure with 380 nm period, as it corresponds to a zero detuning of both resonances. It is plotted in Fig. 5.5 (b). In comparison to the extinction spectrum of a single wire, shown in Fig. 2.5, the asymmetric Fano-type shape of the spectrum becomes apparent, indicating on a Fano resonance. Similarly to the oscillator model, it exhibits a vanishing extinction around 580 nm wavelength, as it can be explained by the destructive interference of both modes in the inner of the waveguide and a therefore increased transmission.

5.2.2 Fano resonances in photochromic metallic photonic crystal slabs

Based on the theoretical considerations on Fano resonances in bare metallic photonic crystal slabs, presented in the last section, the system is now extended by an additional XDTE layer in order to implement the switching capability in the system. The resulting system is sketched in Fig. 5.6.
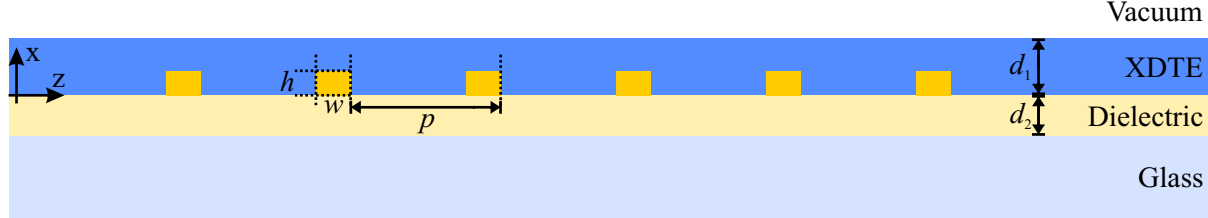

Figure 5.6: Photochromic metallic photonic crystal slab with gold wires of height h, width w and a period of p, on top of a dielectric and coated with an XDTE layer, with thicknesses of d_2 and d_1, respectively.

Photochromic dielectric slab waveguides

We start the discussion of this complex system again with the pure slab waveguide, not containing a gold wire array. Since in the last sections the large influence of the waveguide's core on its properties was demonstrated, we make once more use of the modal solver, contained in the Comsol Multiphysics software package, to investigate the complex dependencies in the present system. Herein, the simulated system is similar to the previously discussed one. On top of the glass substrate coated with a dielectric layer of thickness d_2 and a refractive index of $n_d = 1.9$, now the additional XDTE layer is placed. It has a thickness of d_1 and a complex refractive index, as depicted in Fig. 5.1 (b).

Since the TE modes do not contribute to the investigated Fano resonances, the modal solver is used to find only the allowed lowest-order TM modes of the photochromic dielectric slab waveguides. We therefore assume a system with a dielectric layer of 140 nm thickness as well as an XDTE layer of 120 nm thickness for wavelengths from 400 nm to 900 nm in steps of 10 nm. The resulting dispersion relations for both isomers of XDTE are plotted in Fig. 5.7, together with the light lines of the involved media.

In a system with an XDTE layer, being in its transparent state (XDTE-T), similarly to the previously discussed pure dielectric slab waveguide, the dispersion relation is almost straight (see Fig. 5.7 (a)). However, the added XDTE layer induces an overall shift to higher values of β. This is different for the dispersion relation, corresponding to the lowest order mode in a waveguide composed of the second isomer (XDTE-A), as it is plotted in Fig. 5.7 (b). It deviates from a straight line and thus demonstrates the strong influence of the changed material properties on the waveguide modes. Furthermore, the change of the imaginary part is even larger and has a maximum of $\Im(\Delta\beta) = 0.5$ around 610 nm wavelength.

Summarizing these results, the positions of the dispersion relations proof that in the chosen range of parameters wave-guiding is possible. In addition, the strong change of the modal dispersion relations upon a conversion of the XDTE layer from one state to the other, predicts a strong influence on the Fano resonances in the complete system.
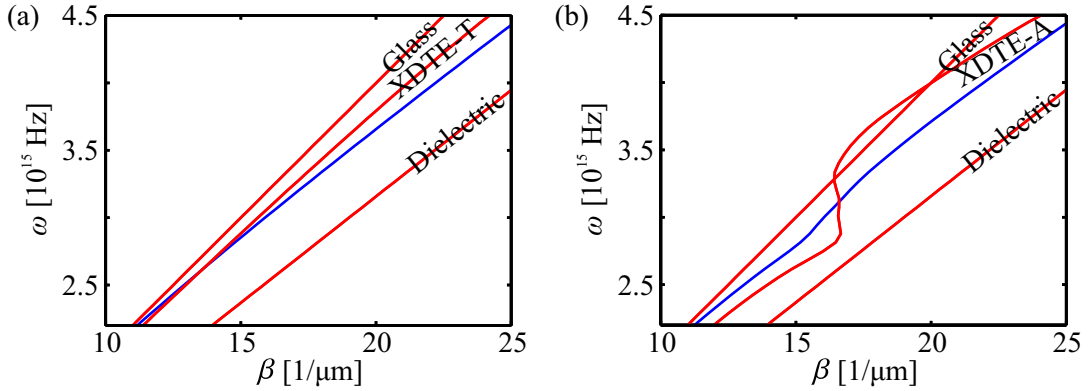
Figure 5.7: The blue lines depict the dispersion relations of TM modes in a waveguide, consisting of a dielectric layer of 120 nm and an XDTE layer with a thickness of 120 nm, being in the transparent state (a) and the absorptive state (b), respectively. In addition, the red lines correspond to the light lines in the involved media.

Photochromic metallic photonic crystal slabs

In the case of a plane wave, being polarized along the z-direction, impinging from the positive x-direction on the system shown in Fig. 5.6, again, the simultaneous excitation of waveguide modes and localized SPPs is possible. In order to model the influence of a changing absorption in the waveguide on the behavior of the system, we can use again the system of two coupled oscillators.

For this purpose, the system containing an XDTE layer, being completely in the transparent state (XDTE-T), can be modeled with the same parameters, as used for the non-switchable case. However, in account for the added XDTE layer, the waveguide's damping has to be slightly larger, and hence is described by $\gamma_{wg} = \gamma_{pl}/40$. The absorption of the resulting system can then be calculated analogously to the previous case. The results for the five different waveguide resonance wavelengths are plotted in Fig. 5.8, depicted in blue.

Again, the sharp peak, depicted in Fig. 5.8 (a), can be assigned to the waveguide resonance, while the broad peak centered at 610 nm wavelength stems from the plasmonic resonance. Now, due to the slightly higher damping in the waveguide, the corresponding peak is broader and lower in comparison to Fig. 5.4. However, by decreasing the detuning of both resonances, the hybridization leads still to an avoided crossing of the waveguide-like and plasmon-like peaks (see Fig. 5.8 (a)–(e)). It furthermore indicates on the formation of waveguide plasmon polaritons [53, 54] and, due to asymmetric line shape, also on a Fano resonance. The strongest interaction occurs again for a zero detuning of both resonances (see Fig. 5.8 (c)).

A system containing a layer of XDTE, converted to XDTE-A, is expected to obtain different absorption spectra. The increase of absorption in comparison to the previous case leads to a higher damping in the waveguide and can, according to the later presented experimental data, be modeled with a damping, given by $\gamma_{wg} = \gamma_{pl}/4$. The resulting absorption spectra are depicted in Fig. 5.8, colored in red.

While in this simple model the peak positions are not affected by the changed environment, the larger damping leads to an even increased broadening and lowering of the waveguide-like
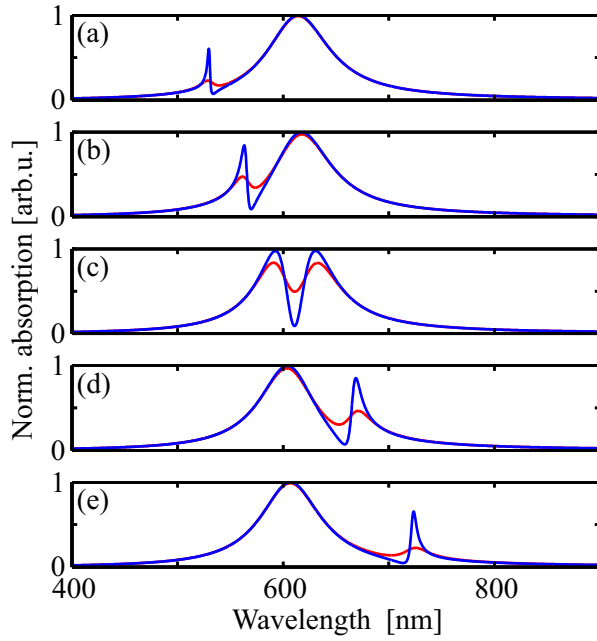
Figure 5.8: Modeled absorption of a system of two coupled oscillators with a plasmonic resonance fixed at 610 nm wavelength and waveguide resonances at 532 nm (a), 569 nm (b), 610 nm (c), 660 nm (d), and 717 nm (e) wavelength, respectively. The case of the XDTE layer being in the transparent state is depicted in blue, while the results for XDTE-A are colored in red.

peaks in the case of a large detuning (see Fig. 5.8 (a)). When the detuning of both resonances is lowered and changes its sign, similarly to the weakly damped system, an avoided crossing of both peaks can be recognized in Fig. 5.8 (b)–(e). Again, the strongest influence on the absorption is achieved for zero detuning, when both resonances overlap, as it is depicted in Fig. 5.8 (c). However, in contrast to the weakly damped system, the drop of absorption in considerably smaller and the Fano resonance is blurred out. This increase of absorption of about 50% shows that the quality of a Fano resonance can be strongly affected by changing the absorption in the wave-guiding layer.

Scattering matrix based calculations

In order to examine the influence of a changing absorption in the waveguide on the behavior of the system with more rigorous simulations, the already introduced scattering matrix based algorithm is used again. The considered geometry herein corresponds to the one depicted in Fig. 5.6. In correspondence to the calculations, discussed in the context of a bare metallic photonic crystal slab, the dielectric layer has a thickness of 140 nm and a refractive index of $n_d = 1.9$. Furthermore, the last section showed that a waveguide with an XDTE layer of 120 nm thickness allows for the excitation of TM modes in the investigated spectral region. Since, in this case the mode is strongly influenced by a conversation of XDTE from one isomer to the other, we concentrate here on this thickness only, by taking the optical properties of both isomers again from Fig. 5.1 (b).

The resulting extinction spectra (negative decadic logarithm of the transmission) for gold wires with a height of 40 nm and width of 90 nm, being regularly arranged with periods between 340 nm and 500 nm, are shown in Fig. 5.9 for both possible states of the XDTE layer.

Regarding firstly the case of a transparent XDTE layer, which is depicted in Fig. 5.9 (a). Similarly to the calculated extinction spectra of the bare metallic photonic crystal, shown in Fig. 5.5,
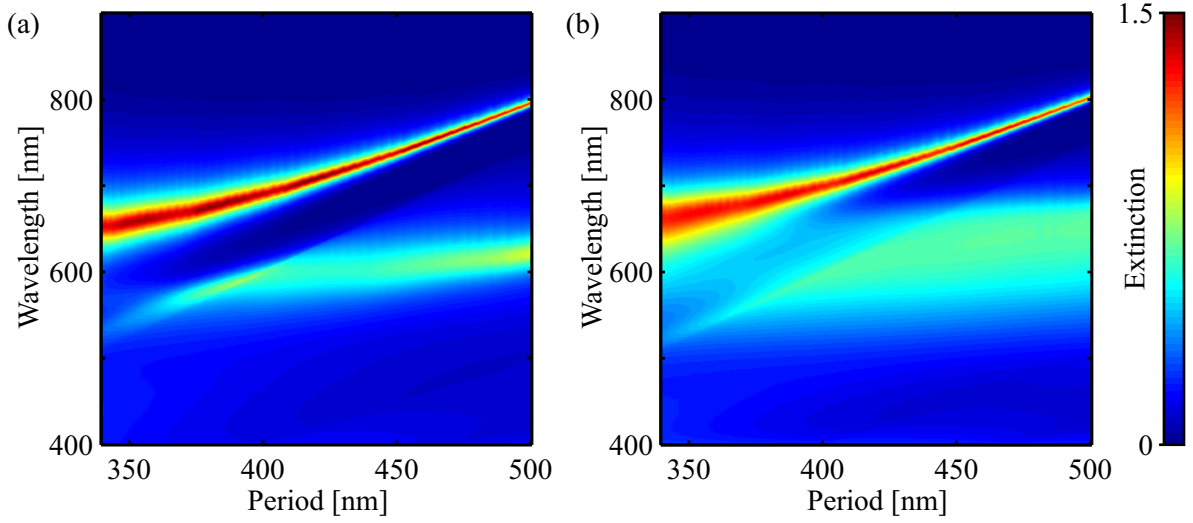
Figure 5.9: Calculated extinction spectra of the proposed geometry for grating periods between 340 nm and 500 nm, embedded in an XDTE layer converted to XDTE-T (a) and XDTE-A (b), respectively.

these spectra exhibit an avoided crossing of the plasmon-type and the waveguide-type peaks, by increasing the period of the gold wire grating. Due to the additional wave-guiding (XDTE) layer, however, all spectral features are shifted to larger wavelengths. This was expected already from the dispersion relations of the bare slab waveguide, shown in Fig. 5.7.

The extinction spectra of the photochromic metallic photonic crystal slab with an XDTE layer, in the absorptive state (XDTE-A), are plotted in Fig. 5.9 (b). In comparison to the extinction spectra, depicted in Fig. 5.9 (a), all spectral features are again slightly shifted to higher wavelengths, as it can be explained by the change of the real part of the complex refractive index. However, even more interesting and more pronounced is the change of extinction around 610 nm wavelength. Here, the strong absorption band of the XDTE-A layer can be recognized. It induces a blurring of all spectral features, being maximal in the extinction spectrum of a structure with a grating period of 380 nm, where the position of the Fano dip corresponds to the maximal absorption of XDTE. The according extinction spectra are plotted in Fig. 5.10 for both states of the XDTE layer.

Figure 5.10: Calculated extinction spectra of a photochromic metallic photonic crystal slab containing a grating of 380 nm period and an XDTE layer, being in the absorptive state (blue) and the transparent state (green). In addition, the extinction spectrum of a bare XDTE-A layer on top of the dielectric coated glass substrate is depicted in red.
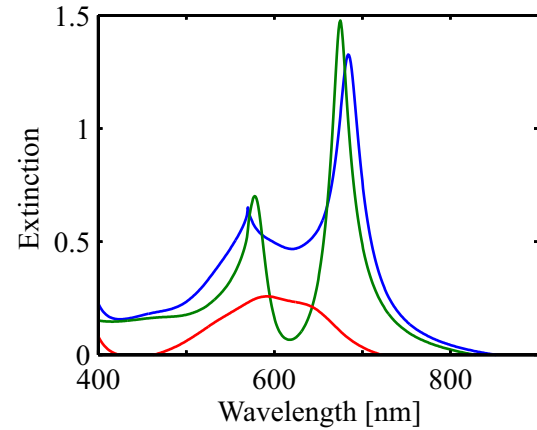
The extinction spectrum of the photochromic metallic photonic crystal slab with the XDTE layer in the absorptive state (XDTE-A), is depicted in blue, while the corresponding spectrum of the layer, being in the transparent state (XDTE-T), is colored in green. Both spectra exhibit a clear Fano-type line shape. Furthermore, directly in the Fano dip and consistent with the coupled oscillator model, an increase of the absorption in XDTE layer leads to a dramatical increase of the extinction. In comparison to the case of a transparent XDTE layer it results in a difference in extinction as large as $\Delta E = 0.4$. However, in comparison to the extinction of bare XDTE-dielectric-glass system (depicted as red line in Fig. 5.10), this change cannot be explained by the absorption of the XDTE layer alone, acting as additional filter.

As can be recognized from the peak positions in Fig. 5.10, the difference of the real parts of the refractive indices of both isomers of XDTE has a rather low influence of the system. It induces an only small spectral shift of the peaks upon a conversion of XDTE from one isomer to the other. Hence, this system promises an effective photochromic switching of Fano resonances, induced by a predominant change in the absorption.

5.2.3 Fabrication of photochromic metallic photonic crystal slabs

This section introduces the methods utilized for the fabrication of photochromic metallic photonic crystal slabs. By using positive tone electron beam lithography (pEBL) the gold wire arrays are fabricated on top of an ITO (indium tin oxide) layer, serving as dielectric waveguide. The XDTE is spin-coated in a subsequent step.

Positive tone EBL

As substrate, we use a 1 mm thick 4" glass-wafer, consisting of crown glass (BK-7). Onto that substrate, an ITO film of 140 nm thickness is evaporated by electron beam physical vapor deposition. Subsequently, the substrate is annealed for 4 h at a temperature of 400 °C, in order to ensure the oxidation of the ITO. The resulting ITO layer serves two different purposes. On the one hand it is the conducting layer, needed for the following electron beam exposure. On the other hand, it acts as the desired dielectric waveguide needed for the investigations of Fano resonances.

In order to reduce the size of the samples, the wafers are cut into 2 cm × 2 cm-pieces and cleaned with acetone in an ultrasonic bath for 1 h. Then, in order to prepare the sample for the electron beam exposure, approximately 90 μl of PMMA with a molecular weight of 950 k and dissolved at 4 % in annisole,[3] is spin-coated onto the sample in two steps: (i) For 3 s at 500 rpm, in order to distribute the solution over the sample (ii) For 90 s at 4000 rpm, to achieve a layer thickness of up to 200 nm. Subsequently, the samples are annealed at 175 °C for 45 min, resulting in PMMA-ITO covered glass substrates, as sketched in Fig. 5.11 (a).

In the next step, the sample is placed in an SEM.[4] Similarly to the application in gEBL, presented in Sec. 3.4, this machine facilitates the controlled electron beam exposure of the PMMA layer, by tracing simple geometrical structures (see Fig. 5.11 (b)).

---

[3] Supplied by the micro resist technology GmbH, Germany
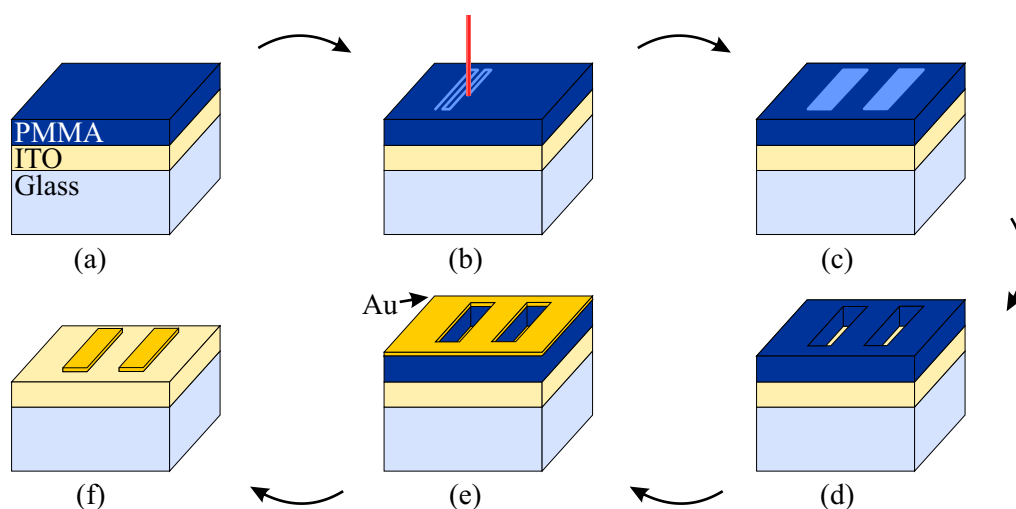[4] Zeiss Sigma with an attached ELPHY Plus system (see Sec. 3.4 for more details)

Figure 5.11: (a) PMMA-ITO coated glass substrate (b) Electron beam exposure (c) Exposed PMMA areas (d) Hole mask (e) Gold covered hole mask (f) Gold gratings on top of the ITO layer.

In contrast to gEBL, in this process PMMA is used as a positive tone resist. Therefore, the locally applied doses are chosen such that cross-linking of the layer is avoided, but the polymeric chains are disassembled and thus become less resistant against solvents [78]. For this purpose, the structures are exposed by applying an electron acceleration voltage of 20 kV, an aperture of 20 μm, a nominal dose of 400 μC/cm^2, and a step-size of 0.0032 μm.

The form of the resulting structures after e-beam exposure (Fig. 5.11 (c)) is influenced again by the proximity effect (for a detailed description see Sec. 3.4). However, in all designs discussed in the present section, the distances between all structures are rather large so that the effect does not play an important role here.

After the electron beam exposure, the samples are soaked in a developer[5] for 45 s. This results in a hole mask, being a negative image of the desired structures (Fig. 5.11 (d)). The fabrication of the gold structures of appropriate thickness is achieved by evaporating a 40 nm thick layer of gold, at a rate of 2 $\frac{\text{Å}}{\text{s}}$ and a typical pressure of approximately 1.5×10^{-6} mbar, onto that mask (compare Fig. 5.11 (e)).

In the last step the remaining unexposed gold coated PMMA is lifted off by placing the sample in NMP[6] for 2h at 60 °C, flushing with ethanol and methanol, and subsequently blowing off the remaining solvent residues with pressured nitrogen. After this step the samples consist of gold wires on top of an ITO layer (see Fig. 5.11 (f)).

XDTE Layer

The XDTE layers were provided by R. C. Shallcross.[7] In detail, a solution of 9 $\frac{\text{mg}}{\text{ml}}$ XDTE containing the photo acid 4-octyloxydiphenyliodonium hexafluoroantimonate (OPPI[8]) is spin-

---

[5] A 1:3 solution of MIBK (methyl isobutyl ketone) and isopropyl alcohol, including 1.5 vol-% butanone

[6] N-Methyl-2-pyrrolidon

[7] Group of Prof. Dr. Klaus Meerholz, Institut für Physikalische Chemie, Universität zu Köln

[8] Supplied by the ORGANICA Feinchemie GmbH Wolfen, Germany

coated onto the structured sample at 700 rpm. The resulting layer is illuminated with UV light of 312 nm wavelength for 60 s and subsequently cured for 2.5 min at 110 °C on a hot plate to finalize the cross-linking. Since one layer yields approximately 60 nm of thickness, the whole procedure was repeated twice in order to gain a total thickness of approximately 120 nm.

5.2.4 Fabricated samples

On top of the ITO layer of approximately 140 nm thickness, the gold wires are designed as rectangles of 90 nm width, 80 μm length, and a dose of 120% of the nominal dose. While their thickness is solely determined by the evaporation procedure (40 nm), in the grating design, the wires are arranged with periods from 350 nm up to 490 nm, in 10 nm-steps. One typical overview SEM image of a fabricated structure including an uncoated grating with a design period of 380 nm is shown in Fig. 5.12 (a).
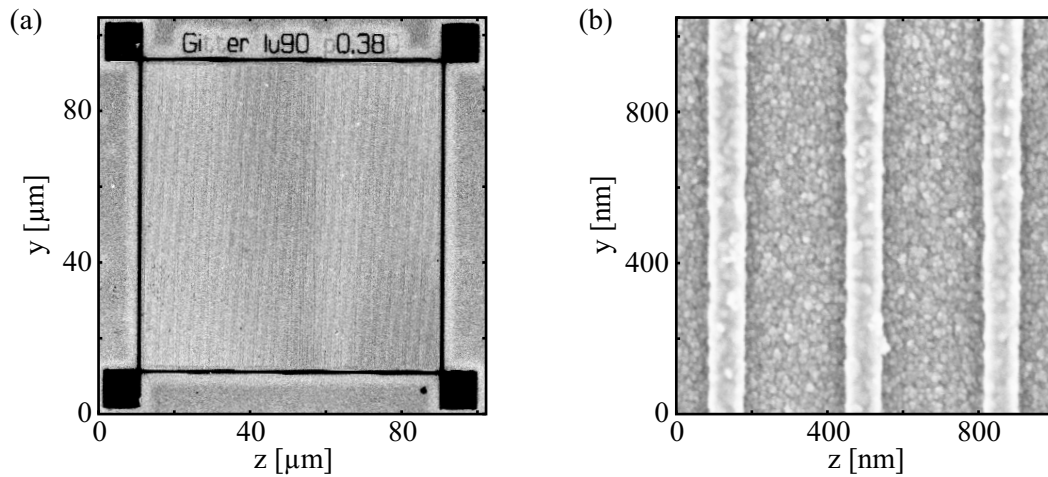
Figure 5.12: SEM overview image of an uncoated gold grating with 380 nm design period, on top of an ITO layer (a) and a magnified image of the central part ot the same grating (b).

All structures visible in this image correspond to gold structures on top of the ITO layer. Surrounded by four markers and the labeling of the structure, the actual grating is contained in the square-shaped region in the central part of the image. The markers herein span the write field with a size of 100 μm × 100 μm. The grating elements itself can be recognized in a magnified image of this grating, as it is shown in Fig. 5.12 (b). The gold wires obtain a width of approximately 95 nm and a period of approximately 369 nm. This deviation is taken into account in the following discussions, by utilizing only the measured periods of all fabricated gratings.

All of the already presented and some of the subsequently discussed measurements are performed before the XDTE layer of approximately 120 nm is added to the system. This facilitates the characterization of the uncoated sample and avoids the manipulation of the XDTE layer, as for example by an electron beam exposure.

These fabricated photochromic metallic photonic crystal slabs hence provide the desired dimensions of all components, such as gold wires and material layers. However, since the

refractive index of ITO, in contrast to the considered constant value in the theoretical discussions, is dispersive in the relevant spectral range [115], deviations of the experimental results can be expected.

5.2.5 Optical setup

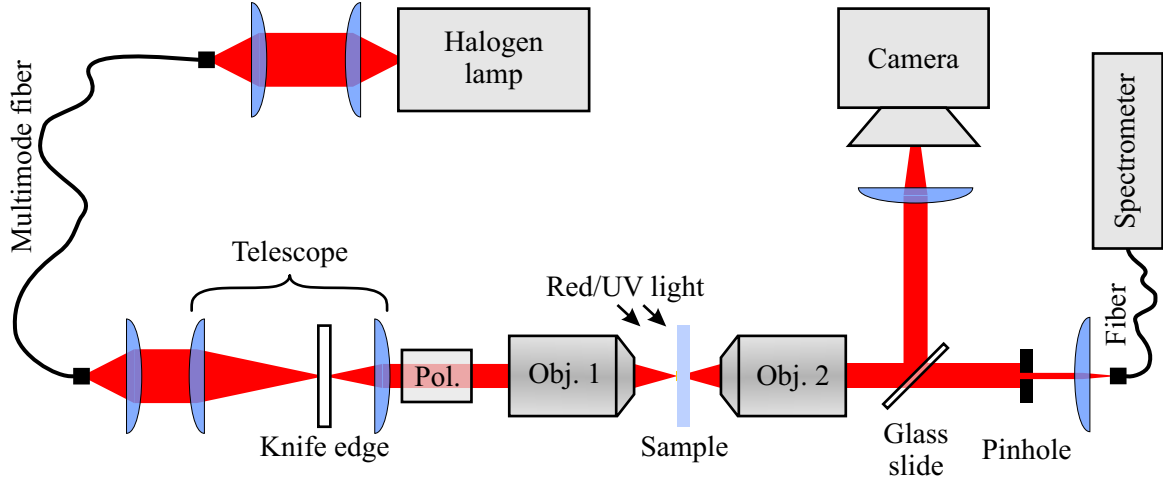The optical setup used to characterize the samples is sketched in Fig. 5.13.

Figure 5.13: Optical setup used for the spectral characterization of the fabricated photochromic metallic photonic crystal slabs.

For the present experiments we use a thermal light source of 22 W, providing high intensity and a broad spectrum in the investigated spectral region around 600 nm. The emitted light is collimated and subsequently coupled into an optical multi-mode fiber, in order to create a point-like white light source.

The light emitted by the fiber, is collimated with a lens and subsequently passes an optical telescope with a magnification of one third, serving two purposes. On the one hand, it reduces the diameter of the light beam and increases the intensity of the beam. On the other hand, in its focal point a knife edge is placed, which can be used to crop the beam.

With a reduced diameter, the beam passes a polarizer, attached to a rotational mount. Afterwards, the polarized light beam is focused onto the sample by making use of Objective 1.[9] This results in a real image of the knife-edge on the sample. The sample itself is mounted on an XYZ translation stage, a double goniometer and a rotation stage in order to control its spatial orientation on each rotation and translation axis.

Transmitted by the sample, the beam is collimated by Objective 2, being identical in construction to the first one. The beam passes a glass slide, is partially reflected and then imaged on a camera.[10] This facilitates the imaging of the illuminated areas on the sample and, in combination with the knife edge, the controlled measurement of the sample's transmission.

---

[9] Plan N 10x, Olympus Deutschland GmbH, Germany
[10] DCC1545M, Thorlabs GmbH, Germany

The transmitted proportion of the beam passes a 100 μm pinhole before it is focused onto a second optical multi-mode fiber. The pinhole herein causes a reduction of the detected angular range. As previous experiments revealed, this is necessary to avoid the imaging of higher order grating effects, which can occur due to the illumination with an angular broadly distributed light source [121].

Finally, the optical fiber is connected to a spectrometer,[11] which facilitates the measurement of transmission properties of the sample on short timescales. By this approach a manipulation of the used photochromic layer due to the used light source can be minimized.

Switching of the photochromic layer

In addition to the presented details, the setup allows for the switching of the used photochromic layers by flood illumination without having to remove the sample. To induce the conversion from the transparent to the absorptive state, a hand-held UV fluorescent tube with a wavelength of 302 nm can be mounted over the sample. Analogue, to perform the reverse conversion, a red LED with 623 nm wavelength can be fixed to the same position. Due to the low intensities on the sample's surface in both cases, the times needed to switch the layers are in the range of minutes.

5.2.6 Results: Bare metallic photonic crystal

Before the XDTE film is prepared, the bare metallic photonic crystal slabs are investigated. For this purpose, the sample is placed in the optical setup described above, and illuminated with TM polarized white light. The extinction spectrum (negative decadic logarithm of the transmission) of the bare ITO coated glass is measured and used as reference for the subsequent measurements. Based on this, the extinction spectrum of each fabricated gold wire grating on top of the ITO coated glass substrate is captured and column-wise plotted in Fig. 5.14 (a).

The depicted extinction spectra exhibit two peaks with different spectral positions, depending on the grating period. In accordance with the theoretical considerations, they can be assigned to the plasmon-like and waveguide-like peak. With an increasing period of the gold wire grating, both peaks perform the anticipated avoided crossing, due to the interaction of plasmonic and waveguide mode. Hence, these extinction spectra are the experimental demonstration of the formation of waveguide plasmon polaritons [53, 54]. The apparent deviation of the extinction spectrum corresponding to the 360 nm-grating stems from a slight corruption of the grating in the fabrication. It will therefore be recognizable also in all subsequent measurements on this sample.

The extinction spectrum of a bare metallic photonic crystal slab with a grating of a 380 nm period is plotted in Fig. 5.14 (b). As expected from the coupled oscillator model and the scattering matrix based calculations, this spectrum clearly provides an asymmetric Fano type line shape, indicating on a Fano resonance. The vanishing extinction in between both peaks, according to the theoretical considerations, stems from the destructive interference of the waveguide and the plasmonic mode in the structure.
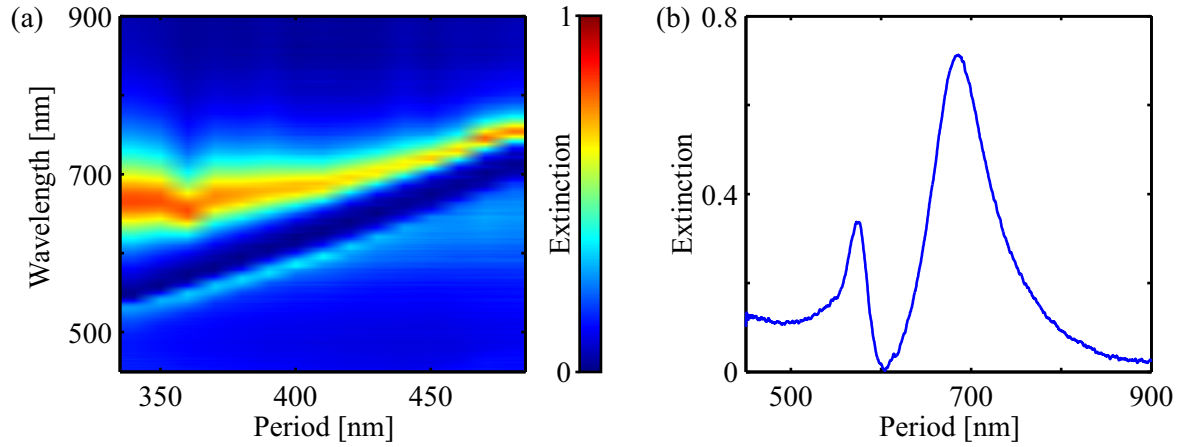
---

[11] USB4000, Ocean Optics, USA

Figure 5.14: (a) Measured extinction spectra of the bare metallic photonic crystals, consisting of gold wire gratings with measured periods between 340 nm and 480 nm, on top of an ITO layer with 140 nm thickness. (b) Extinction spectrum, corresponding to a grating with period of 380 nm, as extracted from (a).

However, several deviations of the experimental data to the theoretical calculations, depicted in Fig. 5.5, can be noticed. In the experimental images, the peaks are broader and spectrally shifted. This is mainly induced by the highly dispersive behavior of ITO, which was neglected in the simulations. Additionally, the imperfectness of structures and layers leads to a larger damping in the system. That induces an overall broadening of the peaks and an additional shift of the spectral positions.

5.2.7 Results: XDTE coated metallic photonic crystals

Next, the sample is coated with two layers of XDTE, resulting in a thickness of approximately 120 nm. Subsequently, one part of the sample is cleaned in order to facilitate a measurement of the extinction of the bare ITO coated glass substrate. It is used as the reference in all following measurements.

Bare XDTE-ITO coated glass substrate

Before the photochromic metallic crystal slabs are investigated, the extinction spectra of the XDTE layer in both possible states are measured in order to characterize the conversion efficiency. For this purpose, initially, the XDTE layer is switched to XDTE-A, by flood illumination with UV light for 40 min. The first extinction spectrum (E_A) is captured in this case. Subsequently, the sample is flood illuminated with red light for 60 min, converting the XDTE layer to the transparent state. Under these conditions, the second extinction spectrum (E_T) is measured. Both resulting spectra (E_A and E_T) are plotted in Fig. 5.15.

A strong difference between the extinction spectra of layers in both states is obvious as it is needed for the implementation of the photochromic switching in the current system. The areas of negative extinction, existent in both cases, can be explained by the formation of an anti-reflex coating, induced by the layered design of the sample.
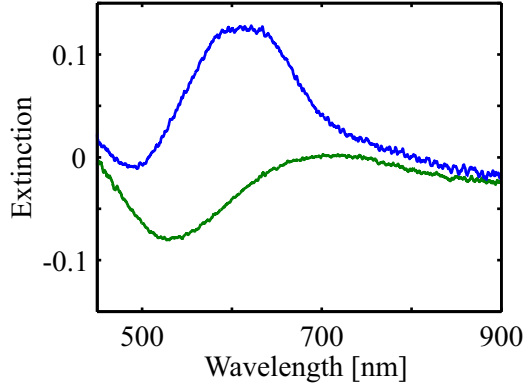
Figure 5.15: Extinction spectrum of the pure XDTE layer on top of the ITO coated substrate, being in the absorptive state (E_A, depicted in blue) and the transparent state(E_T, colored in green), respectively.

In comparison to Fig. 5.10 the experimentally measured peak extinction of XDTE-A is slightly smaller than expected. This can however be explained by the neglected dispersion of ITO in the calculations and a smaller conversion efficiency of the XDTE layer than predicted. Nevertheless, the switching of the layer's properties has succeeded and can hence be used for the manipulation of Fano resonances.

XDTE coated metallic photonic crystal slabs

With the results of the last section as a basis, the photochromic switching of Fano resonances in metallic photonic crystal slabs can now be investigated experimentally. For this purpose, initially, the sample is illuminated for 60 min with red light, in order to convert the complete photochromic layer to XDTE-T. Subsequently, with the extinction spectrum of the bare ITO coated glass substrate as reference, the extinction spectra of all fabricated gratings are captured. The results are plotted column-wise in Fig. 5.16 (a).
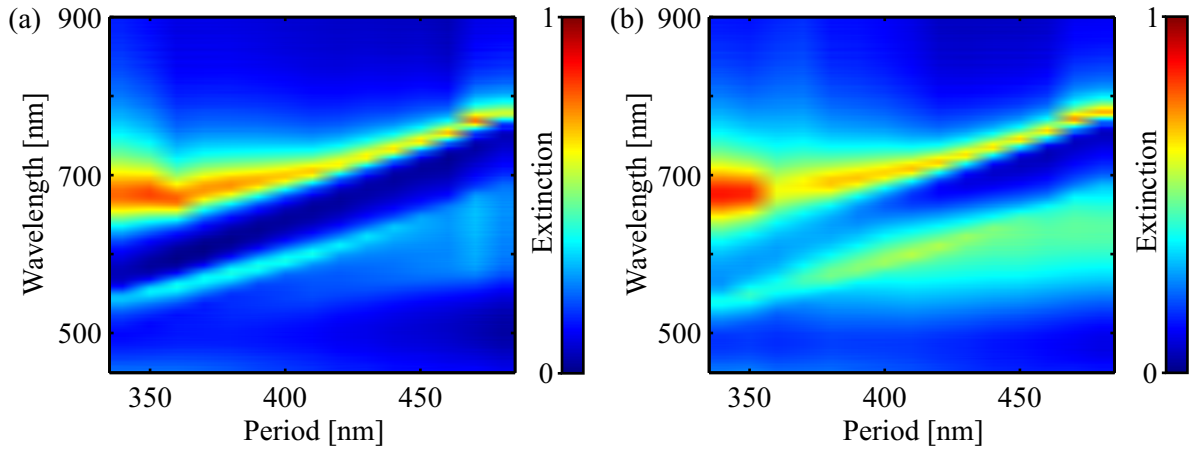

Figure 5.16: Extinction spectra of photochromic metallic photonic crystals containing gratings of varying periods and an XDTE layer, being converted to XDTE-T (a) and XDTE-A (b), respectively.

The spectra of all investigated photochromic metallic photonic crystals with XDTE being in the transparent state (XDTE-T) exhibit two peaks, which can be assigned to the plasmon-like and waveguide-like peaks, according to the theoretical considerations and to the results, shown

in Fig. 5.14 (a). Analogously, the avoided crossing of both peaks is again apparent and an experimental demonstration of the formation of waveguide plasmon polaritons [53, 54]. However, due to the addition of the XDTE layer and the increased size of the waveguide, the spectral features are slightly shifted to higher wavelengths.

Next, the sample is flood illuminated for 40 min with UV light, leading to a conversion of the XDTE layer to the absorptive state (XDTE-A). As before, the extinction spectra of all fabricated gratings are captured and plotted column-wise in Fig. 5.16 (b).

Again, the two peaks (waveguide-like and plasmon-like peaks) show an avoided crossing, similarly to the previous cases. In addition, around 600 nm wavelength, a clear absorption band, corresponding to the extinction of XDTE-A, occurred. Consistent with the theoretical calculations, this leads to a blurring of all spectral features, including both peaks.

The highest influence of the switching is expected for the case in which the Fano dip and the maximal absorption of the XDTE layer overlap. This is the case for a photochromic metallic photonic crystal slab with a grating with 380 nm period. The spectra of this structure are depicted in Fig. 5.17 with an the XDTE layer in both states together with the extinction of a bare XDTE-A film.

Figure 5.17: Extinction spectra of photochromic metallic photonic crystal slab obtaining a grating with 380 nm period and an XDTE layer, being converted to XDTE-A (blue) or XDTE-T (green). Additionally, the extinction of a bare XDTE-A layer is depicted in red.
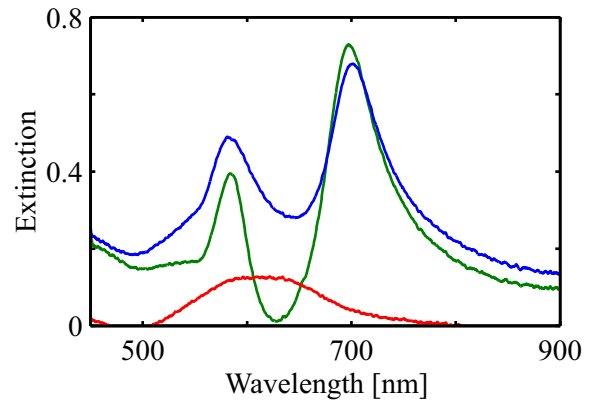
The extinction spectra of the photochromic metallic photonic crystal slab incorporating XDTE-A and XDTE-T are depicted in green and blue, respectively. Both spectra exhibit two peaks and a dip in between, representing once more a clear asymmetric Fano-type line shape and hence a Fano resonance. While the positions of both peaks differ only slightly, as induced by the change of the real part of the refractive index of the XDTE layer, the Fano dip in the middle of the spectrum is strongly blurred in the case of high damping. This leads to a maximal difference of extinction of $\Delta E = 0.3$, as it corresponds to a difference in transmission of $\Delta T = 0.49$. Furthermore, a comparison to the extinction of a bare XDTE-A layer (red line in Fig. 5.17) reveals, that this effect cannot be explained by a simple filter-like absorption of the photochromic layer alone. In fact, the massive manipulation of the interaction of waveguide and plasmonic mode is the reason for the switching of the Fano resonance. Neglecting the smaller switching efficiency due to the non optimal conversion of the layer, the results are in excellent agreement with the theoretical calculations, shown in Fig. 5.10.

5.3 Manipulation of propagating surface plasmon polaritons

The second topic investigated in this chapter is the influence of a photochromic state change on SPPs propagating at a photochromic-gold interface. In this context, previously, only the influence of a predominant change of the absorption of a photochromic layer was investigated by Pala et al. [43]. However, a manipulation of the SPP propagation, caused by a changing real part of the refractive index of a photochromic material has not been demonstrated so far. Such an approach, presuming the ability to locally change the state of the layer, would facilitate the generation of nearly arbitrary refracting boundaries and hence optical devices for propagating SPPs with switchable properties.

5.3.1 Manipulation concept

In order to investigate the influence of a changing real part of the photochromic materials' refractive index on propagating SPPs, in principle, both presented materials could be utilized. However, since the propagation length of propagating SPPs increases with the wavelength, a material with a high switching efficiency in the long wavelength regime is suitable. By comparing both materials in Fig. 5.1, it turns out that XTPA has to be favored. Moreover, a good trade off between low absorption and high switching efficiency of the real part of the refractive index can be found at 830 nm wavelength.

Global switching of the XTPA layer

The first case to discuss is the influence of a state change of a whole XTPA layer on the properties of propagating SPPs. For this purpose, we consider an XTPA layer of thickness d, sandwiched between a gold and a vacuum half-space, similar to the case sketched in Fig. 3.4.
By using the same approach as in Subsec. 3.3.1, the complex effective refractive index of propagating SPPs in the three layer system can be calculated for each thickness d and state of the layer. The resulting real and imaginary parts for a free space wavelength of 830 nm and the optical properties taken from Fig. 5.1, are plotted in Fig. 5.18.
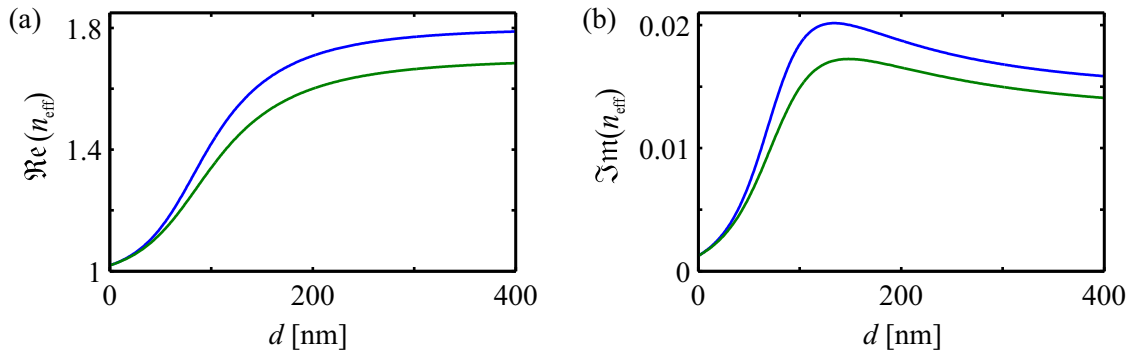

Figure 5.18: Real (a) and imaginary parts (b) of the effective refractive index of SPPs (free space wavelength 830 nm), propagating at an XTPA metal interface with an XTPA layer of thickness d being completely converted to XTPA-A (blue) and XTPA-T (green), respectively.

Analogously to the case of a simple dielectric, in both states an increasing thickness of the layer leads to an increasing influence of the material, accompanied by an increasing effective refractive index. For thicknesses larger than 400 nm, the real and imaginary parts of the effective refractive indices approximate the values of the two layer system, consisting of only XTPA and gold. In accordance to the values presented in Fig. 5.1, in the depicted range of parameters, XTPA-A induces slightly larger values than XTPA-T.

Note that, as discussed already in Subsec. 2.3.2, the leakage radiation of propagating SPPs cannot be detected anymore, if the effective refractive index exceeds the value of the numerical aperture (in the subsequently discussed experimental setup it is given by 1.49). Therefore, the maximal applicable thickness of an XTPA layer at 830 nm free space wavelength is 110 nm. In this case the effective refractive index of propagating SPPs in a layer being completely converted to XTPA-A, is given by $n_{\text{effA}} = 1.47 + 0.019i$, while in the case of the layer being in the transparent state, the effective refractive index is given by $n_{\text{effT}} = 1.38 + 0.016i$. Together this results in a $\Delta n_{\text{eff}} = 0.09 + 0.003i$.

Transmission properties of the XTPA layer

The grade of conversion of such an XTPA layer can be easily tested by measuring its transmission in both states. Since the properties highly depend on the layer thickness, a typical system containing XTPA is investigated by making use of Comsol Multiphysics. The simulated 2D geometry consists of an XTPA layer of various thicknesses (90 nm, 110 nm, 130 nm), as well as a gold layer of 60 nm thickness on top of a glass substrate. In order to investigate the transmission of this system, a modeled plane wave with 830 nm wavelength is excited on the vacuum side and collected in the glass substrate. The wave vector is chosen perpendicular to the surface.

From the resulting transmission spectra T_T and T_A of a system with an XTPA layer being converted to XTPA-T and XTPA-A, respectively, the ratio of the transmitted intensities can be determined as given by T_T/T_A. The results are plotted in Fig. 5.19 (a) for all investigated thicknesses.
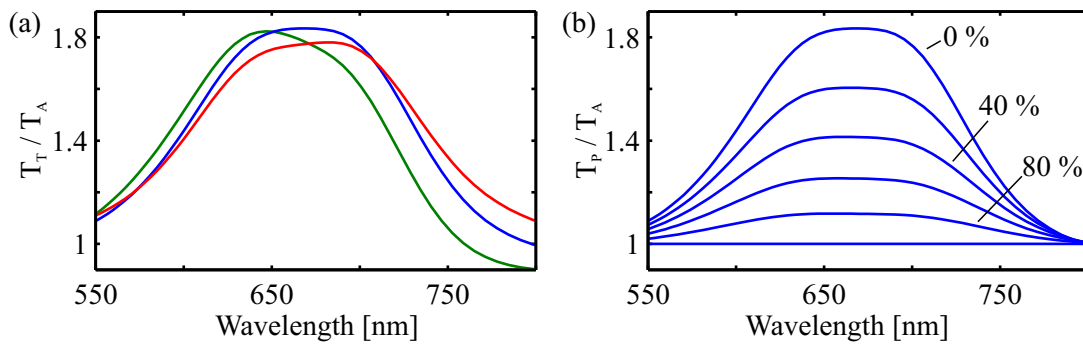

Figure 5.19: (a) Simulated transmission ratios of an XTPA layer in both states, for thicknesses of 90 nm (green), 110 nm (blue), 130 nm (red). (b) Transmission ratios of an XTPA layer of 110 nm thickness for an increasing amount of non-switched molecules, resting permanently in the absorptive state (XDTE-A).

In all considered cases, the maximal ratio T_T/T_A can be found around 670 nm wavelength. The position and form of this graph is herein not only influenced by the absorption of the material

itself. Due to the layered type of structure the exact profile depends additionally on the thickness of the XTPA layer.

While the previous simulations concentrated solely on completely converted layers, in a second step, the influence of a non optimal conversion is investigated theoretically. Analogously to the Arago-Biot equation for the mixing of binary liquids [122], we approximate the optical properties of the photochromic layer by averaging over the optical properties of the contained isomers of XTPA in dependence on their volume fractions. This is implemented in the simulation by describing the optical properties of the layer by the following equation:

$$n_p = (1 - p) \cdot n_{\text{XTPA-T}} + p \cdot n_{\text{XTPA-A}}, \tag{5.6}$$

with the parameter p ranging from 0 to 1. Based on this, analogously to the previously discussed case, Comsol Multiphysics simulations are performed for various values of p. The resulting simulated ratios of the transmission through XTPA in the mixed state (T_p) to the transmission through XTPA in the absorptive state (T_A) are plotted in Fig. 5.19 (b).

Obviously and as expected, the transmitted intensity is highly dependent on the effectiveness of the switching process. Hence, the transmittance spectra of a bare film can be utilized to examine the conversion efficiency of the material.

Local switching of the XTPA layer

A particular interesting case to investigate is the local switching of the photochromic material on top of the gold substrate, as it leads to a local increase or decrease of the effective refractive index of propagating SPPs. By controlling the form of the boundary of such a switched area, one could hope to manipulate the propagation of SPPs. For example, a circular structure could act as a collimating or diffusing lens, depending on the refractive index of the surrounding material. However, by switching the whole layer all devices could be erased again.

An exemplary 2D system is investigated by using Comsol Multiphysics. A circle of 5 μm diameter is placed in 5 μm distance from a source, emitting a TM polarized plane wave of 830 nm wavelength. Assuming an XTPA layer of 110 nm thickness, the disc and the surrounding area exhibit two different effective refractive indices, as given by n_{effT} and n_{effA}. The resulting normalized intensity distributions for both possible cases are depicted in Fig. 5.20 (a) and (b), respectively.

In Fig. 5.20 (a) the effective refractive index in the disc is smaller than the one of the surrounding. It therefore acts as a diffusing lens for the plane wave, which is excited at z = 0 and propagates in the positive z-direction. The reversed case is shown in Fig. 5.20 (b). Here, the higher effective refractive index in the disc leads to a focusing of the plane wave, resulting in a focal point behind the lens.

Both examples indicate that local switching of propagating SPPs can be achieved by using XTPA combined with an appropriate switching light source. By assuming a Gaussian shaped laser spot, the presented example is the simplest realization. However, by moving the laser spot over the sample or by moving the sample, optical lithography can be performed, leading to the realization of nearly any structure. Even more complicated structures, such as gradient index elements would be possible by only partially switching the layer.
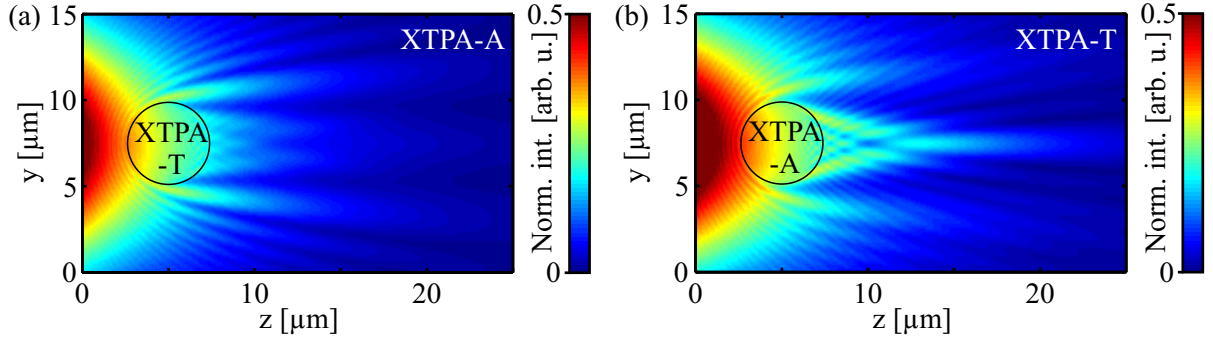
Figure 5.20: (a) TM polarized electromagnetic wave propagating in XTPA-A, impinges on an XTPA-T disc. (b) TM polarized electromagnetic wave propagating in XTPA-T, impinges on an XTPA-A disc.

5.3.2 Fabricated samples

The samples needed for the experimental realization of the described effects should provide a gold surface, coated with XTPA, and an embedded grating coupler, facilitating the excitation of propagating SPPs. For this purpose, similar substrates as in the experiments on DLSPPWs are used: glass cover-slides covered with 10 nm of chromium and 60 nm gold.

On top of these substrates, the necessary gold gratings are fabricated making use of pEBL again (see Subsec. 5.2.3 for more details). They are designed as gold wires of 200 nm width, 80 μm length, 40 nm height and a dosis of 140% of the nominal dose. The grating periods, required to excite propagating SPPs in the three layer system, depend on the thickness and state of the layer. In order to cover a wide range of possible scenarios, gratings with various periods are fabricated, starting from 460 nm up to 700 nm. An SEM image of a resulting structure with a typical grating of 700 nm period is depicted in Fig. 5.21.

Figure 5.21: Exemplary SEM image of one write field, containing a grating of 700 nm period, surrounded by the labeling of the structure and cross-shaped markers.
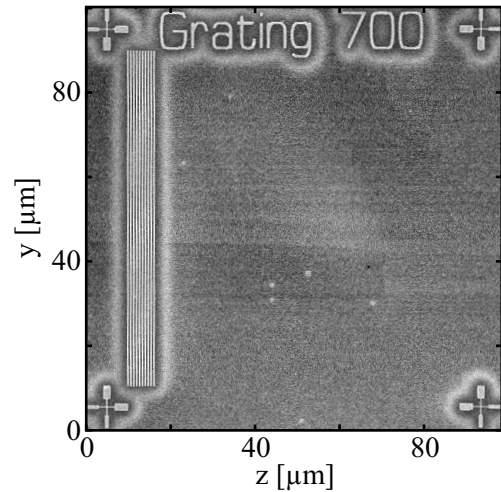
The grating is surrounded by the labeling as well as four markers of a different type, compared to the previous experiments. This new design allows for a precise coordinate-system correction in further lithographic procedures, such as optical lithography. The grating itself facilitates the excitation of propagating SPPs in both directions.

XTPA coating

In the last step, the sample is spin-coated with a solution, containing $18\,\frac{mg}{ml}$ of XTPA and OPPI, at a rotation velocity of 700 rpm. Subsequently, the layer is annealed with UV light at 312 nm for 120 s and cured for 5.5 min at 110 °C. Finally, the sample is flushed with toluene in order to remove the not cross-linked residues.

The thickness of the resulting film was measured on unstructured gold coated samples to be approximately 40 nm per layer. In order to fabricate a thicker layer of XTPA, the procedure is repeated twice, resulting in a thickness of approximately 80 nm. It can, however, be anticipated that the XDTE is thicker in the vicinity of the gold structures (gratings, markers, labels).

5.3.3 Optical setup

Since this section concentrates again on the investigation of propagating SPPs, the optical setup used here bases on the one presented in the previous chapter (sketched in Fig. 4.31). The imaging part remains unchanged and still facilitates both, real space and Fourier space imaging. The central part of the used setup is sketched in Fig. 5.22. It includes the extensions added in account for the different types of experiments carried out in this section:
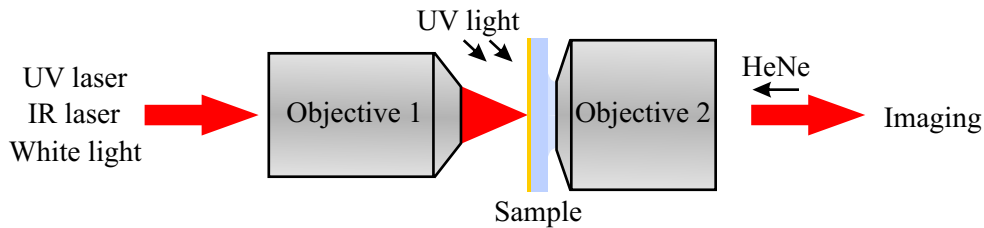

Figure 5.22: Experimental setup, used for the investigation of the local and global photochromic switching of propagating SPPs.

In the present setup, a laser diode of 830 nm wavelength is used for the excitation of propagating SPPs. Furthermore, this setup now supports both types of switching. The global switching of the layers can be achieved by flood illumination of the sample with a thermal light source (600 nm peak-wavelength), coupled into the beam path via a polarizing beam splitter, as well as a UV fluorescent tube (302 nm peak-wavelength), mounted over the sample. Additionally, an UV laser (405 nm) and a HeNe laser (633 nm), being focused onto the sample, facilitate the local switching of the photochromic layer.

The sample itself is placed on a multi-axis piezo system for the highly resolved positioning.[12] Together with a homemade Labview script, simple geometrical objects such as lines and circles can be traced by moving the sample accordingly, facilitating optical lithography.

5.3.4 Results: Transmission measurements

As a first step, the transmission through the fabricated XTPA layer on top of the gold surface is measured for both possible states. The measurements are carried out right next to a fabricated

---

[12] NanoCube P-611.3S, Physik Instrumente (PI) GmbH, Germany

grating, by utilizing an optical setup, similarly to the one presented in Fig. 5.13. Due to the simple type of structure (plain layers), the small pinhole could be waived. In addition, the light intensity is decreased as far as possible, in order to avoid an unwanted conversion of the photochromic layer.

Two transmission spectra are captured, the first one (T_A) after 60 min of flood illumination with UV light, resulting in a layer converted to XTPA-A. The second one (T_T) after 60 min of illumination with white light, when the layer is in the transparent state. The ratio (T_T/T_A) of both spectra is plotted in Fig. 5.23.

Figure 5.23: Ratio of the transmission through an XTPA film illuminated with white light (T_T) and an XTPA film illuminated with UV light (T_A), as determined by (T_T/T_A).
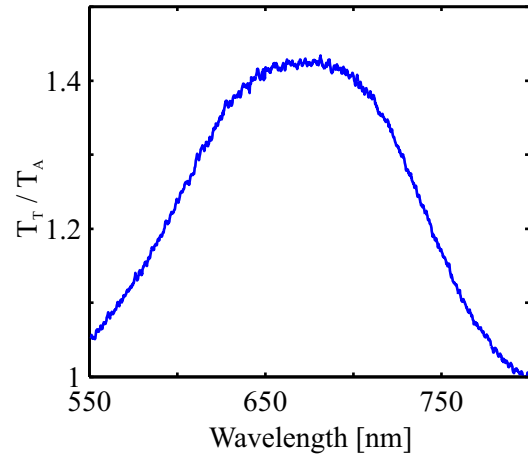
This experimentally determined transmission ratio deviates from the theoretical calculations for a film with the expected parameters, as it is presented in Fig. 5.19. In contrast it is, however, similar to the ratio of the calculated transmission spectra of an XTPA layer of 110 nm thickness, consisting of an isomer mixture of 60% XTPA-A and 40% XTPA-T, in comparison to a layer being completely in the absorptive state. Therefore, a similar thickness and conversion efficiency can be presumed also for the fabricated layer.

The increased layer thickness can be explained by the presence of the fabricated gold structures. However, the reduced grade of conversion leads to the assumption that the XTPA layer is corrupted. This could be explained either by optical fatigue similar to XDTE or by a degradation of the layer due to oxidization [123]. Based on this, for all subsequent experiments, a smaller change of the real part of the refractive index can be anticipated.

5.3.5 Results: Global switching

In order to investigate the influence of a globally switched layer on propagating SPPs, the XTPA layer is illuminated with white light for 90 min and hence is converted to XTPA-T. Subsequently, the 830 nm laser is focused on a grating in order to excite propagating SPPs. The resulting normalized intensity distribution is depicted in Fig. 5.24 (a), on a logarithmic color scale.

Due to the position of the laser spot on the grating, the excitation of propagating SPPs takes place mostly in the positive z-direction. Besides the clear Gaussian shape of the SPP beam, small scattering at surface and grating inhomogeneities can be recognized.

In order to gain more information on the complex refractive index distribution, also the Fourier
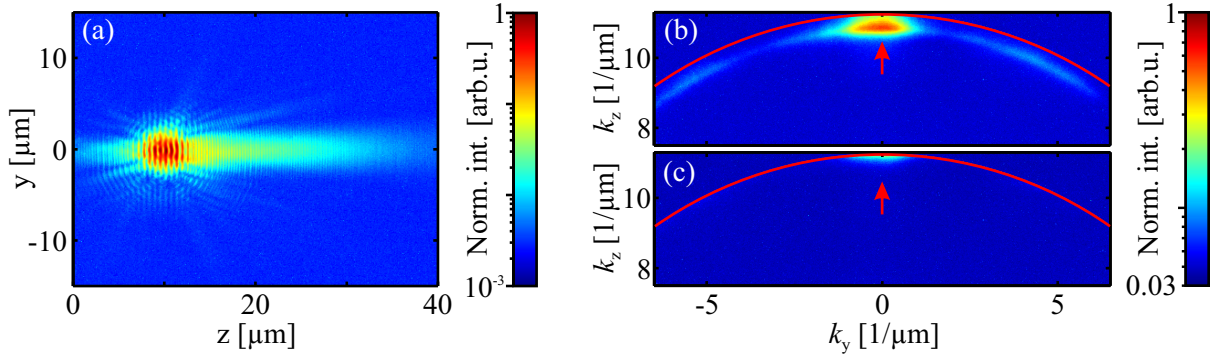
Figure 5.24: (a) Real space image of propagating SPPs in an XTPA layer in the transparent state. (b) The Fourier space image corresponding to (a). (c) Fourier space image of propagating SPPs excited with the same grating, but with an XTPA layer being in the absorptive state. The red arrows mark the position of the subsequently fitted data. The red lines correspond to the border of the objective's BFP.

space image is captured. On this data the same post-processing is applied as in the context of DLSPPW arrays. The resulting normalized intensity distribution in the Fourier space is shown in Fig. 5.24 (b), on a logarithmic color scale.

While, induced by the propagation of the SPPs in z-direction, the largest fraction of the intensity is assembled around $k_y = 0$, the mentioned scattering of the propagating SPPs leads to the occurrence of a circular intensity distribution in the Fourier space image. The constant radius indicates on an equally distributed effective refractive index of the SPPs. In order to measure this radius, a Lorentz curve is fitted to a data line, indicated by the red arrow. The resulting peak position corresponds to an effective refractive index of $n_{effT} = 1.439 \pm 0.005$. In comparison to the theoretically expected value, described in Sec. 5.3.1, this effective refractive index is larger.

In oder to investigate the index on its influence of a switched layer, without moving the sample, by illumination with UV light for 40 min, the layer is converted back to the absorptive state (XTPA-A). Subsequently, propagating SPPs are excited at the same position on the grating again. Since the resulting real space image is similar to the presented one, we concentrate here on the resulting Fourier space image, only, which is shown in Fig. 5.24 (c).

By comparing both Fourier space images, two features attract attention. On the one hand, the higher damping of the system leads to a reduction of the overall intensity. On the other hand, the radius of the circular intensity distribution increased drastically. This indicates on an even larger effective refractive index as in the previous case. In order to measure it, again, a Lorentz curve is fitted to a data line, indicated by the red arrow. In this case, the effective refractive index is calculated to be $n_{effA} = 1.51 \pm 0.06$. The larger error herein can be explained by the position of the expected peak, laying outside of the angular range collected by the objective. By taking the measurement error into account, this value corresponds to the one expected for XTPA-A thickness of 110 nm.

A comparison of the difference of both values to the theoretically expected value, also described in Sec. 5.3.1, reveals a strong deviation. The experimentally determined difference is smaller. This is, however, in good accordance to the reduced conversion efficiency and the higher thickness of the XTPA layer, as assumed in the last section.

5.3.6 Results: Local switching

Next, the influence of a locally switched layer on propagating SPPs is investigated. Preliminary, the whole XTPA layer is switched to the XTPA-A state, by flood illumination with UV light for approximately 50 min. Subsequently, the HeNe laser is focused on a position with a distance of approximately 10 μm to the grating for approximately 5 min. Due to its spot-size (a few μm), this results in a small area, being converted to the transparent state.

In these conditions, propagating SPPs are excited by focusing the 830 nm-laser onto the gold grating. The resulting intensity distribution is depicted in Fig. 5.25, with the position of the switched area being indicated by the arrow.

Figure 5.25: Propagating SPPs, excited at a grating and propagating in positive z-direction. The position of a manipulated area is indicated by the black arrow.
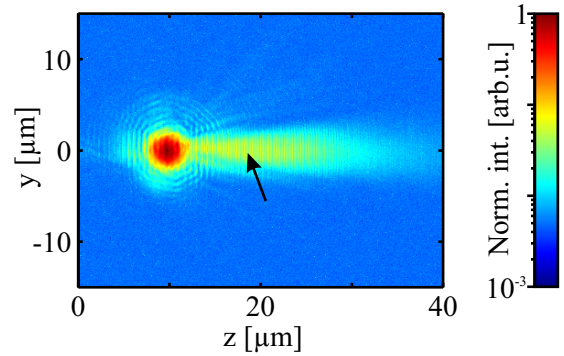
The SPPs propagate in positive z-direction, similarly to the previously discussed case, shown in Fig. 5.24 (a). However, they are passing the switched region without a detectable influence.

This measurement exemplifies the results obtained from all experiments, performed on the local switching of propagating SPPs on the presented sample. This includes also the contrary type of switching (XTPA-T is converted locally to XTPA-A, by making use of the UV laser). The reason for this behavior in the present case is the non-optimal conversion efficiency of the layer, mentioned in the last sections. Since it is accompanied by a reduced change of the real part of the effective refractive index, the remaining influence is covered by the inhomogeneities of the layer itself.

Summary

In this thesis we explored how surface plasmon polaritions (SPPs) can be manipulated with dielectric nanostructures. For this purpose, we considered both, stationary and switchable environments. Herein, the main results of this thesis are: (i) The manipulation of Airy SPP beams (non-diffracting plasmonic wave packages) by making use of gradient refractive index (GRIN) elements. (ii) The observation of excited topologically protected edge states and bulk states in dielectric loaded SPP waveguide (DLSPPW) arrays, simulating a Su-Schrieffer-Heeger (SSH) topological insulator. (iii) The switching of Fano resonances in photochromic metallic photonic crystal slabs. (iv) The manipulation of propagating SPPs by switching a photochromic material.

In detail, the first part of this thesis concentrated on the excitation and manipulation of propagating Airy SPP beams at a gold vacuum interface. While the excitation was realized by specially designed grating couplers, the manipulation was achieved by adding dielectric ramps on top of the gold surface, inducing a gradient in the effective refractive index. Both, ramps and gratings were fabricated out of PMMA by making use of gray-scale electron beam lithography (gEBL). As a result, various PMMA grating couplers as well as ramps of different height gradients were deposited on top of the gold surface. These fabricated samples were experimentally investigated with an optical setup, based on leakage radiation microscopy (LRM).

By this approach it was possible to observe freely propagating Airy SPP beams and, for the first time, Airy SPP beams propagating in PMMA ramps. We showed that such ramps can be utilized to alter the propagation properties of Airy SPP beams. In fact, an inversion of their bending direction in comparison to an undisturbed Airy SPP beam was realized. All results were in excellent agreement with numerical simulations.

The results demonstrated that gEBL is a versatile tool that can be utilized to fabricate dielectric structures for the excitation and manipulation of propagating SPPs. Additionally, LRM offers the possibility to image the intensity distribution of propagating SPPs also in complex PMMA structures.

In the second part of this thesis we implemented the Su-Schrieffer-Heeger (SSH) model, i.e., the prototypical system of a 1D topological insulator, in arrays of evanescently coupled DLSPPWs. The basis for this is the mathematical equivalence between the evolution of electrons in a crystal, as described by the condensed matter tight binding model, and the spatial evolution of SPPs

in the waveguide arrays, as described by the coupled mode theory (CMT). By making use of gEBL, various DLSPPW arrays were fabricated on top of the gold layer, corresponding to different realizations of the SSH model. Propagating SPPs in these arrays were experimentally investigated in an optical setup, facilitating the imaging of the real and Fourier space intensity distributions.

We observed excited topologically protected edge states and bulk states in the fabricated arrays both, in real and Fourier space. In the real space, an excitation of bulk modes led to a strongly broadening SPP intensity distribution in propagation direction, while the excited topologically protected edge states exhibited a clear localized evolution. Simultaneously, in the Fourier space intensity distributions the topologically protected edge states could be identified as states within a band gap of two cosine-shaped bands, formed by the bulk modes. These images marked the first experimental observation of a band structure including excited topologically protected edge states in a plasmonic system. In this context, the influence of different fabrication parameters was investigated extensively. The remaining deviations to the numerical calculations obtained from CMT could be explained by the neglected non next neighbor coupling effects. This was confirmed by a numerical analysis of the eigenmodes of the system. These results exhibited an excellent accordance to the experimental results.

As indicated by these experiments and the theoretical considerations, DLSPPW arrays are a versatile tool in terms of mimicking condensed matter effects. They allow for the tuning of all essential parameters as the coupling between the DLSPPWs as well as the properties of the single DLSPPWs.

The last part of this thesis was dedicated to two different approaches to implement the photochromic switching in plasmonic systems. Both systems incorporated gold gratings, fabricated with positive tone electron beam lithography and coated with photochromic molecules, provided by the group of Prof. Dr. Meerholz from the Universität zu Köln.

It was shown that photochromic metallic photonic crystal slabs consisting of an XDTE-ITO waveguide incorporating gold gratings of various periods can exhibit Fano resonances at various wavelengths. In this system the Fano resonance describes the interaction of localized plasmonic modes and delocalized waveguide modes. Hence, the position of the corresponding Fano dip depends directly on the spectral detuning of both effects. By carefully adjusting all fabrication parameters it was shown that a state change of the photochromic layer induces a strong alteration of the extinction in the Fano dip. By this approach we achieved a maximum difference in extinction of 0.3, corresponding to a change in transmission of $\Delta T \approx 0.5$.

Secondly, the propagation of SPPs in globally and locally changing refractive index profiles was investigated. By switching a complete layer of the photochromic material XTPA, deposited top of the gold film, a change of the effective refractive index of propagating SPPs in this environment could be measured to be approximately 5%. In comparison to the theoretical expectations, this rather small value can be probably be traced back to a suboptimal film quality. This also prevented the manipulation of propagating SPPs by a locally switched layer.

Although both types of experiments suffered from the non-optimal conversion of the photochromic layers, a strong influence on the behavior of the plasmonic systems could be demonstrated. Hence, this approach builds a basis for promising further applications.

Outlook

The results presented in this thesis represent the current state of the research in this area. Based on the discussed results several pursuing investigations are of high interest. I would like to mention some of them.

As introduced within this thesis, DLSPPW arrays can be utilized as simulators for condensed matter systems, which allow for the control over all essential parameters, as coupling constants and effective refractive indices. As mentioned previously, the remaining deviations to the theoretical predictions were accounted to the proximity effect only, whose influence could be minimized in future experiments [80]. Hence, this system forms a good basis for more in-depth investigations of more elaborate systems.

Since the topologically protected edge states are especially robust against perturbations [99, 100], it would be interesting to investigate the influence of various types of perturbations. Since temporally changing properties of a condensed matter system correspond to spatially changing properties in the plasmonic system, the influence of temporal effects on such states can be easily investigated in a plasmonic system. This includes a (in the real systems not trivially realizable) phase change between two different topological phases, as it can be achieved by changing the coupling and effective refractive index profiles simultaneously [124]. But also the influence of a temporally changing or spatially randomized distributed damping can be investigated, based on an incorporation of chromium into the waveguides [33]. Finally, even more topological phases can be realized and investigated by using discrete-time quantum walks [125].

The presented concept of photochromic switching can be applied on many different plasmonic systems:

In terms of Fano resonances, the already explained system of photochromic metallic photonic crystals can be improved by introducing a photochromic material obtaining a higher conversion efficiency. This would then lead to a filter of narrow band width and an improved switching efficiency.

Furthermore, one could make use of the localized switching of photochromic films. This concept could be applied for example on plasmonic Yagi Uda antennas [126]. If, initially, the directors and reflectors of such antenna are covered by a photochromic material being in an absorptive state, while the material around the emitter is in a transparent state, the antenna would act as simple dipole antenna. In contrast, if the complete layer is in the transparent state, it will act

as a complete Yagi Uda antenna. Hence, this approach allows to switch the directivity of such antenna. This can, however, not only achieved by local switching but also by locally destroying the photochromic layer with an electron beam, since this permanently converts the layer to a transparent state, as first experiments have approved.

On the basis of the results, presented in this thesis, these pursuing investigations, hence promise an deeper insight into even more elaborate physical systems.

Bibliography

[1] R. H. Ritchie, *Plasma Losses by Fast Electrons in Thin Films*, Phys. Rev. **106**, 874–81 (1957).

[2] A. Otto, *Excitation of nonradiative surface plasma waves in silver by the method of frustrated total reflection*, Zeitschrift für Phys. **216**, 398–410 (1968).

[3] E. Kretschmann and H. Raether, *Radiative decay of non-radiative surface plasmons by light*, Zeitschrift für Naturforsch. A **23**, 2135 (1968).

[4] J. N. Anker, W. P. Hall, O. Lyandres, N. C. Shah, J. Zhao, and R. P. Van Duyne, *Biosensing with plasmonic nanosensors*, Nat. Mater. **7**, 442–53 (2008).

[5] H. A. Atwater and A. Polman, *Plasmonics for improved photovoltaic devices*, Nat. Mater. **9**, 205–13 (2010).

[6] H. Raether, *Surface Plasmons on Smooth and Rough Surfaces and on Gratings*, Springer Tracts Mod. Phys. **111**, 136 (1988).

[7] W. L. Barnes, A. Dereux, and T. W. Ebbesen, *Surface plamons subwavelength optics*, Nature **424**, 824–30 (2003).

[8] E. Ozbay, *Plasmonics: merging photonics and electronics at nanoscale dimensions*, Science **311**, 189–93 (2006).

[9] A. Hohenau, J. R. Krenn, A. L. Stepanov, A. Drezet, H. Ditlbacher, B. Steinberger, A. Leitner, and F. R. Aussenegg, *Dielectric optical elements for surface plasmons*, Opt. Lett. **30**, 893–5 (2005).

[10] F. Bleckmann, *Transformationsoptik mit Oberflächenplasmonen*, Diploma Thesis: Universität Bonn, 2012.

[11] B. Steinberger, A. Hohenau, H. Ditlbacher, F. R. Aussenegg, A. Leitner, J. R. Krenn, A. L. Stepanov, and A. Drezet, *Dielectric stripes on gold as surface plasmon waveguides*, Appl. Phys. Lett. **88**, 081111 (2006).

[12] B. Steinberger, A. Hohenau, H. Ditlbacher, F. R. Aussenegg, A. Leitner, and J. R. Krenn, *Dielectric stripes on gold as surface plasmon waveguides: Bends and directional couplers*, Appl. Phys. Lett. **91**, 2005–8 (2007).

[13] T. Holmgaard and S. Bozhevolnyi, *Theoretical analysis of dielectric-loaded surface plasmon-polariton waveguides*, Phys. Rev. B **75**, 245405 (2007).

[14] E. Devaux, J.-Y. Laluet, B. Stein, C. Genet, T. Ebbesen, J.-C. Weeber, and A. Dereux, *Refractive micro-optical elements for surface plasmons: from classical to gradient index optics*, Opt. Express **18**, 20610–9 (2010).

[15] T. Zentgraf, Y. Liu, M. H. Mikkelsen, J. Valentine, and X. Zhang, *Plasmonic Luneburg and Eaton lenses*, Nat. Nanotechnol. **6**, 151–5 (2011).

[16] M. Berry and N. Balazs, *Nonspreading wave packets*, Am. J. Phys. **47**, 264–7 (1979).

[17] J. Broky, G. A. Siviloglou, A. Dogariu, and D. N. Christodoulides, *Self-healing properties of optical Airy beams*, Opt. Express **16**, 12880–91 (2008).

[18] A. Salandrino and D. N. Christodoulides, *Airy plasmon: a nondiffracting surface wave*, Opt. Lett. **35**, 2082–4 (2010).

[19] A. Minovich, A. E. Klein, N. Janunts, T. Pertsch, D. N. Neshev, and Y. S. Kivshar, *Generation and Near-Field Imaging of Airy Surface Plasmons*, Phys. Rev. Lett. **107**, 116802 (2011).

[20] L. Li, T. Li, S. M. Wang, C. Zhang, and S. N. Zhu, *Plasmonic airy beam generated by in-plane diffraction*, Phys. Rev. Lett. **107**, 1–4 (2011).

[21] P. Zhang, S. Wang, Y. Liu, X. Yin, C. Lu, Z. Chen, and X. Zhang, *Plasmonic Airy beams with dynamically controlled trajectories*, Opt. Lett. **36**, 3191–3 (2011).

[22] A. E. Klein, A. Minovich, M. Steinert, N. Janunts, A. Tünnermann, D. N. Neshev, Y. S. Kivshar, and T. Pertsch, *Controlling plasmonic hot spots by interfering Airy beams*, Opt. Lett. **37**, 3402 (2012).

[23] W. Liu, D. N. Neshev, I. V. Shadrivov, A. E. Miroshnichenko, and Y. S. Kivshar, *Plasmonic Airy beam manipulation by linear optical potentials*, Opt. Lett. **36**, 1164–6 (2011).

[24] A. W. Snyder, *Coupled-Mode Theory for Optical Fibers*, J. Opt. Soc. Am. **62**, 1267 (1972).

[25] A. Yariv, *Coupled-mode theory for guided-wave optics*, IEEE J. Quantum Electron. **9**, 919–33 (1973).

[26] D. H. Dunlap and V. M. Kenkre, *Dynamic localization of a charged particle moving under the influence of an electric field*, Phys. Rev. B **34**, 3625–33 (1986).

[27] H. S. Eisenberg, Y. Silberberg, R. Morandotti, A. R. Boyd, and J. S. Aitchison, *Discrete Spatial Optical Solitons in Waveguide Arrays*, Phys. Rev. Lett. **81**, 3383–6 (1998).

[28] T. Pertsch, T. Zentgraf, U. Peschel, A. Bräuer, and F. Lederer, *Anomalous refraction and diffraction in discrete optical systems*, Phys. Rev. Lett. **88**, 093901 (2002).

[29] U. Peschel, T. Pertsch, and F. Lederer, *Optical Bloch oscillations in waveguide arrays*, Opt. Lett. **23**, 1701–3 (1998).

[30] R. Morandotti, U. Peschel, J. S. Aitchison, H. S. Eisenberg, and Y. Silberberg, *Experimental Observation of Linear and Nonlinear Optical Bloch Oscillations*, Phys. Rev. Lett. **83**, 4756–9 (1999).

[31] A. Block, C. Etrich, T. Limboeck, F. Bleckmann, E. Soergel, C. Rockstuhl, and S. Linden, *Bloch oscillations in plasmonic waveguide arrays*, Nat. Commun. **5**, 3843 (2014).

[32] T. Vogler, *Anderson localization in disordered plasmonic waveguide arrays*, Master Thesis: Universität Bonn, 2014.

[33] P. Pai, *Sub-ballistic Transport in Coupled Dissipative Plasmonic Waveguide Arrays*, Master Thesis: Universität Bonn, 2015.

[34] A. Hohenau, J. R. Krenn, A. Drezet, O. Mollet, S. Huant, C. Genet, B. Stein, and T. W. Ebbesen, *Surface plasmon leakage radiation microscopy at the diffraction limit*, Opt. Express **19**, 25749 (2011).

[35] W. P. Su, J. R. Schrieffer, and A. J. Heeger, *Solitons in polyacetylene*, Phys. Rev. Lett. **42**, 1698 (1979).

[36] A. J. Heeger, S. Kivelson, J. R. Schrieffer, and W. P. Su, *Solitons in conducting polymers*, Rev. Mod. Phys. **60**, 781–850 (1988).

[37] M. Z. Hasan and C. L. Kane, *Colloquium: Topological insulators*, Rev. Mod. Phys. **82**, 3045–67 (2010).

[38] X. L. Qi and S. C. Zhang, *Topological insulators and superconductors*, Rev. Mod. Phys. **83**, 1057 (2011).

[39] Q. Cheng, Y. Pan, Q. Wang, T. Li, and S. Zhu, *Topologically protected interface mode in plasmonic waveguide arrays*, Laser Photon. Rev. **9**, 392–8 (2015).

[40] S. Khatua, W.-S. Chang, P. Swanglap, J. Olson, and S. Link, *Active modulation of nanorod plasmons*, Nano Lett. **11**, 3797–802 (2011).

[41] N. Strohfeldt, A. Tittl, M. Schäferling, F. Neubrech, U. Kreibig, R. Griessen, and H. Giessen, *Yttrium hydride nanoantennas for active plasmonics*, Nano Lett. **14**, 1140–7 (2014).

[42] N. K. Emani, T.-F. Chung, X. Ni, A. Kildishev, Y. P. Chen, and A. Boltasseva, *Electrically Tunable Plasmonic Resonances with Graphene*, Nano Lett. **12**, 5202–6 (2012).

[43] R. A. Pala, K. T. Shimizu, N. A. Melosh, and M. L. Brongersma, *A nonvolatile plasmonic switch employing photochromic molecules*, Nano Lett. **8**, 1506–10 (2008).

[44] A.-L. Baudrion, A. Perron, A. Veltri, A. Bouhelier, P.-M. Adam, and R. Bachelot, *Reversible strong coupling in silver nanoparticle arrays using photochromic molecules*, Nano Lett. **13**, 282–6 (2013).

[45] Y. Zheng, B. Kiraly, and S. Cheunkar, *Incident-angle-modulated molecular plasmonic switches: a case of weak exciton–plasmon coupling*, Nano Lett., 2061–5 (2011).

[46] H. Nishi, T. Asahi, and S. Kobatake, *Light-Controllable Surface Plasmon Resonance Absorption of Gold Nanoparticles Covered with Photochromic Diarylethene Polymers*, J. Phys. Chem. C **113**, 17359–66 (2009).

[47] H. Nishi and S. Kobatake, *Photochromism and Optical Property of Gold Nanoparticles Covered with Low-Polydispersity Diarylethene Polymers*, Macromolecules **41**, 3995–4002 (2008).

[48] U. Fano, *Effects of configuration interaction on intensities and phase shifts*, Phys. Rev. **124**, 1866–78 (1961).

[49] M. Hentschel, M. Saliba, R. Vogelgesang, H. Giessen, A. P. Alivisatos, and N. Liu, *Transition from Isolated to Collective Modes in Plasmonic Oligomers*, Nano Lett. **10**, 2721–6 (2010).

[50] J. B. Lassiter, H. Sobhani, J. A. Fan, J. Kundu, F. Capasso, P. Nordlander, and N. J. Halas, *Fano resonances in plasmonic nanoclusters: Geometrical and chemical tunability*, Nano Lett. **10**, 3184–9 (2010).

[51] N. A. Mirin, K. Bao, and P. Nordlander, *Fano Resonances in plasmonic nanoparticle aggregates*, J. Phys. Chem. A **113**, 4028–34 (2009).

[52] B. Luk'yanchuk, N. I. Zheludev, S. A. Maier, N. J. Halas, P. Nordlander, H. Giessen, and C. T. Chong, *The Fano resonance in plasmonic nanostructures and metamaterials*, Nat. Mater. **9**, 707–15 (2010).

[53] A. Christ, S. G. Tikhodeev, N. A. Gippius, J. Kuhl, and H. Giessen, *Waveguide-plasmon polaritons: strong coupling of photonic and electronic resonances in a metallic photonic crystal slab*, Phys. Rev. Lett. **91**, 183901 (2003).

[54] A. Christ, T. Zentgraf, J. Kuhl, S. G. Tikhodeev, N. A. Gippius, and H. Giessen, *Optical properties of planar metallic photonic crystal structures: Experiment and theory*, Phys. Rev. B **70**, 1–15 (2004).

[55] J. D. Jackson, *Classical Electrodynamics*, vol. 67, 1998.

[56] S. A. Maier, *Plasmonics: Fundamentals and Applications*, Springer US, 2007.

[57] P. B. Johnson and R. W. Christy, *Optical Constants of the Noble Metals*, Phys. Rev. B **6**, 4370–9 (1972).

[58] P. Drude, *Zur Elektronentheorie der Metalle*, Ann. Phys. **306**, 566–613 (1900).

[59] H. A. Lorentz, *The theory of electrons and its applications to the phenomena of light and radiant heat*, BG Teubner, 1916.

[60] F. von Cube, S. Irsen, J. Niegemann, C. Matyssek, W. Hergert, K. Busch, and S. Linden, *Spatio-spectral characterization of photonic meta-atoms with electron energy-loss spectroscopy [Invited]*, Opt. Mater. Express **1**, 1009 (2011).

[61] G. I. Stegeman, R. F. Wallis, and A. A. Maradudin, *Excitation of surface polaritons by end-fire coupling*, Opt. Lett. **8**, 386–8 (1983).

[62] S. I. Bozhevolnyi, J. Erland, K. Leosson, P. M. W. Skovgaard, and J. M. Hvan, *Waveguiding in surface plasmon polariton band gap structures*, Phys. Rev. Lett. **86**, 3008–11 (2001).

[63] J. Seidel, F. I. Baida, L. Bischoff, B. Guizal, S. Grafström, D. Van Labeke, and L. M. Eng, *Coupling between surface plasmon modes on metal films*, Phys. Rev. B **69**, 121405 (2004).

[64] H. Ditlbacher, J. R. Krenn, N. Felidj, B. Lamprecht, G. Schider, M. Salerno, A. Leitner, and F. R. Aussenegg, *Fluorescence imaging of surface plasmon fields*, Appl. Phys. Lett. **80**, 404–6 (2002).

[65] J. Wang, C. Zhao, and J. Zhang, *Does the leakage radiation profile mirror the intensity profile of surface plasmon polaritons?* Opt. Lett. **35**, 1944–6 (2010).

[66] A. Giannattasio and W. L. Barnes, *Direct observation of surface plasmon-polariton dispersion*, Opt. Express **13**, 428–34 (2005).

[67] A. Drezet, A. Hohenau, D. Koller, A. Stepanov, H. Ditlbacher, B. Steinberger, F. R. Aussenegg, A. Leitner, and J. R. Krenn, *Leakage radiation microscopy of surface plasmon polaritons*, Mater. Sci. Eng. B **149**, 220–9 (2008).

[68] B. Hecht, H. Bielefeldt, L. Novotny, Y. Inouye, and D. Pohl, *Local Excitation, Scattering, and Interference of Surface Plasmons*, Phys. Rev. Lett. **77**, 1889–92 (1996).

[69] B. E. A. Saleh and M. C. Teich, *Fundamentals of photonics*, New York: Wiley, 1991.

[70] R. Quidant, N. F. V. Hulst, A. G. Curto, G. Volpe, T. H. Taminiau, and M. P. Kreuzer, *Dot Coupled to a Nanoantenna*, Science (80-.). **329**, 930–3 (2010).

[71] F. Von Cube, J. Niegemann, S. Irsen, D. C. Bell, and S. Linden, *Angular-resolved electron energy loss spectroscopy on a split-ring resonator*, Phys. Rev. B - Condens. Matter Mater. Phys. **89**, 1–5 (2014).

[72] M. W. Klein, T. Tritschler, M. Wegener, and S. Linden, *Lineshape of harmonic generation by metallic nanoparticles and metallic photonic crystal slabs*, Phys. Rev. B **72**, 115113 (2005).

[73] P. Biagioni, J.-S. Huang, and B. Hecht, *Nanoantennas for visible and infrared radiation*, Reports Prog. Phys. **75**, 024402 (2012).

[74] F. Bleckmann, A. Minovich, J. Frohnhaus, D. N. Neshev, and S. Linden, *Manipulation of Airy surface plasmon beams*, Opt. Lett. **38**, 1443–5 (2013).

[75] M. Abramowitz and I. A. Stegun, *Handbook of mathematical functions*, Appl. Math. Ser. **55**, 62 (1966).

[76] A. E. Minovich, A. E. Klein, D. N. Neshev, T. Pertsch, Y. S. Kivshar, and D. N. Christodoulides, *Airy plasmons: Non-diffracting optical surface waves*, Laser Photonics Rev. **8**, 221–32 (2014).

[77] Y. Liu, T. Zentgraf, G. Bartal, and X. Zhang, *Transformational plasmon optics*, Nano Lett. **10**, 1991–7 (2010).

[78] I. Zailer, J. E. F. Frost, V. Chabasseur-Molyneux, C. J. B. Ford, and M. Pepper, *Crosslinked PMMA as a high-resolution negative resist for electron beam lithography and applications for physics of low-dimensional structures*, Semicond. Sci. Technol. **11**, 1235–8 (1996).

[79] A. C. F. Hoole, M. E. Welland, and A. N. Broers, *Negative PMMA as a high-resolution resist - the limits and possibilities*, Semicond. Sci. Technol. **12**, 1166–70 (1997).

[80] M. Parikh, *Corrections to proximity effects in electron beam lithography. I. Theory*, J. Appl. Phys. **50**, 4371–7 (1979).

[81] W. L. Barnes and R. J. Sambles, *Re-radiation from surface-plasmon-polaritons by surface roughness*, Solid State Commun. **55**, 921–3 (1985).

[82] L. Liu, Z. Han, and S. He, *Novel surface plasmon waveguide for high integration*, Opt. Express **13**, 6645–50 (2005).

[83] S. I. Bozhevolnyi, V. S. Volkov, E. Devaux, J.-Y. Laluet, and T. W. Ebbesen, *Channel plasmon subwavelength waveguide components including interferometers and ring resonators*, Nature **440**, 508–11 (2006).

[84] W. Ebbsen, V. S. Volkov, S. I. Bozhevolnyi, E. Devaux, and J. Y. Laluet, *Wavelength Selective Nanophotonics Components Utilizing Channel Plasmon Polaritons*, Nano Lett. **7**, 880–4 (2007).

[85] B. Lamprecht, J. R. Krenn, G. Schider, H. Ditlbacher, M. Salerno, N. Felidj, A. Leitner, F. R. Aussenegg, and J. C. Weeber, *Surface plasmon propagation in microscale metal stripes*, Appl. Phys. Lett. **79**, 51–3 (2001).

[86] H. Ditlbacher, A. Hohenau, D. Wagner, U. Kreibig, M. Rogers, F. Hofer, F. R. Aussenegg, and J. R. Krenn, *Silver Nanowires as Surface Plasmon Resonators*, Phys. Rev. Lett. **95**, 257403 (2005).

[87] Y. Liu and X. Zhang, *Metasurfaces for manipulating surface plasmons*, Appl. Phys. Lett. **103**, 141101 (2013).

[88] T. Holmgaard, *Dielectric-loaded guiding of surface plasmon polaritons*, PhD Thesis: Aalborg Universitet, 2009.

[89] P. Yeh and A. Yariv, *Photonics: Optical Electronics in Modern Communication*, New Delhi: Oxford University Press, 2007.

[90] W. Lin, X. Zhou, G. P. Wang, and C. T. Chan, *Spatial Bloch oscillations of plasmons in nanoscale metal waveguide arrays*, Appl. Phys. Lett. **91**, 243113 (2007).

[91] P. Delplace, D. Ullmo, and G. Montambaux, *Zak phase and the existence of edge states in graphene*, Phys. Rev. B **84**, 1–13 (2011).

[92] S. Ryu and Y. Hatsugai, *Topological Origin of Zero-Energy Edge States in Particle-Hole Symmetric Systems*, Phys. Rev. Lett. **89**, 077002 (2002).

[93] J. Zak, *Berrys phase for energy bands in solids*, Phys. Rev. Lett. **62**, 2747–50 (1989).

[94] M. V. Berry, *Classical adiabatic angles and quantal adiabatic phase*, J. Phys. A. Math. Gen. **18**, 15–27 (1985).

[95] M. Atala, M. Aidelsburger, J. T. Barreiro, D. Abanin, T. Kitagawa, E. Demler, and I. Bloch, *Direct measurement of the Zak phase in topological Bloch bands*, Nat. Phys. **9**, 795–800 (2013).

[96] R. D. King-Smith and D. Vanderbilt, *Theory of polarization of crystalline solids*, Phys. Rev. B **47**, 1651–4 (1993).

[97] C. L. Kane, *Topological Band Theory and the Z2 Invariant*, ed. by M. Franz and L. Molenkamp, Contemporary Concepts of Condensed Matter Science, Elsevier, 2013.

[98] M. Hafezi, S. Mittal, J. Fan, A. Migdall, and J. M. Taylor, *Imaging topological edge states in silicon photonics*, Nat. Photonics **7**, 1001–5 (2013).

[99] Z. Wang, Y. Chong, J. D. Joannopoulos, and M. Soljacić, *Observation of unidirectional backscattering-immune topological electromagnetic states*, Nature **461**, 772–5 (2009).

[100]   T. Kitagawa, M. A. Broome, A. Fedrizzi, M. S. Rudner, E. Berg, I. Kassal, A. Aspuru-Guzik, E. Demler, and A. G. White, *Observation of topologically protected bound states in photonic quantum walks*, Nat. Commun. **3**, 882 (2012).

[101]   D. N. Christodoulides, F. Lederer, and Y. Silberberg, *Discretizing light behaviour in linear and nonlinear waveguide lattices*, Nature **424**, 817–23 (2003).

[102]   J. Grandidier, S. Massenot, G. des Francs, A. Bouhelier, J.-C. Weeber, L. Markey, A. Dereux, J. Renger, M. González, and R. Quidant, *Dielectric-loaded surface plasmon polariton waveguides: Figures of merit and mode characterization by image and Fourier plane leakage microscopy*, Phys. Rev. B **78**, 245419 (2008).

[103]   L. Li, Z. Xu, and S. Chen, *Topological phases of generalized Su-Schrieffer-Heeger models*, Phys. Rev. B **89**, 1–7 (2014).

[104]   V. L. Mironov, *Fundamentals of scanning probe microscopy*, Moscow: Technosfera, (2004).

[105]   F. Koenderink, H. Schokker, and M. Kamp, *Spectrally resolved high-NA back focal plane imaging of fluorescence and nanolaser emission*, LOT-QuantumDesign GmBH, (2013).

[106]   P. Bharadwaj, A. Bouhelier, and L. Novotny, *Electrical excitation of surface plasmons*, Phys. Rev. Lett. **106**, 1–4 (2011).

[107]   A. Drezet, A. Hohenau, A. L. Stepanov, H. Ditlbacher, B. Steinberger, N. Galler, F. R. Aussenegg, A. Leitner, and J. R. Krenn, *How to erase surface plasmon fringes*, Appl. Phys. Lett. **89**, 091117 (2006).

[108]   P. Zacharias, M. C. Gather, A. Köhnen, N. Rehmann, and K. Meerholz, *Photoprogrammable organic light-emitting diodes*, Angew. Chemie Int. Ed. **48**, 4038–41 (2009).

[109]   R. C. Shallcross, P. O. Körner, E. Maibach, A. Köhnen, and K. Meerholz, *A photochromic diode with a continuum of intermediate states: towards high density multilevel storage*, Adv. Mater. **25**, 4807–13 (2013).

[110]   R. C. Shallcross, P. Zacharias, A. Köhnen, P. O. Körner, E. Maibach, and K. Meerholz, *Photochromic Transduction Layers in Organic Memory Elements*, Adv. Mater. **25**, 469–76 (2013).

[111]   F. Bleckmann, E. Maibach, S. Cordes, T. E. Umbach, K. Meerholz, and S. Linden, *Photochromic Switching of Fano Resonances in Metallic Photonic Crystal Slabs*, Adv. Opt. Mater. **2**, 861–5 (2014).

[112]   E. Maibach, *Divergent Synthesis of Crosslinkable Dithienylethenes for Optoelectronic Devices*, PhD thesis: Universität zu Köln, 2015.

[113]   H. Jean-Ruel, R. R. Cooney, M. Gao, C. Lu, M. A. Kochman, C. A. Morrison, and R. J. D. Miller, *Femtosecond dynamics of the ring closing process of diarylethene: A case study of electrocyclic reactions in photochromic single crystals*, J. Phys. Chem. A **115**, 13158–68 (2011).

[114] K. Uchida, A. Takata, S.-i. Ryo, M. Saito, M. Murakami, Y. Ishibashi, H. Miyasaka, and M. Irie, *Picosecond laser photolysis studies on a photochromic oxidation polymer film consisting of diarylethene molecules*, J. Mater. Chem. **15**, 2128 (2005).

[115] A. Christ, *Optical properties of metallic photonic crystal structures*, PhD thesis: Philipps-Universität Marburg, 2005.

[116] D. Nau, R. P. Bertram, K. Buse, T. Zentgraf, J. Kuhl, S. G. Tikhodeev, N. A. Gippius, and H. Giessen, *Optical switching in metallic photonic crystal slabs with photoaddressable polymers*, Appl. Phys. B **82**, 543–7 (2006).

[117] C. L. G. Alzar, M. A. G. Martinez, and P. Nussenzveig, *Classical Analog of Electromagnetically Induced Transparency*, Am. J. Phys. **37**, 6 (2001).

[118] C. W. Hsu, B. G. Delacy, S. G. Johnson, J. D. Joannopoulos, and M. Soljacic, *Theoretical criteria for scattering dark states in nanostructured particles*, Nano Lett. **14**, 2783–8 (2014).

[119] D. Whittaker and I. Culshaw, *Scattering-matrix treatment of patterned multilayer photonic structures*, Phys. Rev. B **60**, 2610–8 (1999).

[120] S. G. Tikhodeev, A. L. Yablonskii, E. A. Muljarov, N. A. Gippius, and T. Ishihara, *Quasiguided modes and optical properties of photonic crystal slabs*, Phys. Rev. B **66**, 045102 (2002).

[121] S. Linden, *Kontrolle der Wechselwirkung zwischen Licht und Partikelplasmonen durch selektive Unterdrückung der Extinktion*, PhD thesis: Universität Marburg, 2002.

[122] N. An, B. Zhuang, M. Li, Y. Lu, and Z.-G. Wang, *Combined Theoretical and Experimental Study of Refractive Indices of Water–Acetonitrile–Salt Systems*, J. Phys. Chem. B **119**, 10701–9 (2015).

[123] M. Kempf, Personal communication: Universität zu Köln.

[124] M. Ezawa, Y. Tanaka, and N. Nagaosa, *Topological phase transition without gap closing*, Sci. Rep. **3**, 2790 (2013).

[125] T. Kitagawa, M. S. Rudner, E. Berg, and E. Demler, *Exploring topological phases with quantum walks*, Phys. Rev. A **82**, (2010).

[126] A. G. Curto, G. Volpe, T. H. Taminiau, M. P. Kreuzer, R. Quidant, and N. F. van Hulst, *Unidirectional emission of a quantum dot coupled to a nanoantenna.*, Science **329**, 930–3 (2010).

Publications

Parts of this thesis have already been published in refereed scientific journals:

- F. Bleckmann, A. Minovich, J. Frohnhaus, D. N. Neshev, and S. Linden, *Manipulation of Airy surface plasmon beams*, Opt. Lett. **38**, 1443–5 (2013).

- F. Bleckmann, E. Maibach, S. Cordes, T. E. Umbach, K. Meerholz, and S. Linden, *Photochromic Switching of Fano Resonances in Metallic Photonic Crystal Slabs*, Adv. Opt. Mater. **2**, 861–5 (2014).

Additional work on other topics have been published in refereed scientific journals:

- A. Block, C. Etrich, T. Limboeck, F. Bleckmann, E. Soergel, C. Rockstuhl, and S. Linden, *Bloch oscillations in plasmonic waveguide arrays*, Nat. Commun. **5**, 3843 (2014).

Acknowledgements